1931 Waikari River Tsunami: New Zealand's largest historical tsunami

Geordie M Donaldson

Supervisors:
Prof. James Goff
Dr. Catherine Chagué-Goff

Submitted in partial fulfilment of the requirements for the degree of Bachelor of Science (Honours),
School of Biological, Earth and Environmental Sciences,
Faculty of Science at the University of New South Wales
June 2016

The University of New South Wales
Faculty of Science
School of Biological, Earth and Environmental Sciences

Honours thesis project declaration page

I, Geordie Donaldson, hereby declare that this submission is my own work and to the best of my knowledge it contains no materials previously published or written by another person, nor material which to a substantial extent has been accepted for the award of any other degree or diploma at UNSW or any other educational institution, except where the acknowledgement is made in the thesis. Any contribution made to the research by others, with whom I have worked at UNSW or elsewhere, is explicitly acknowledged in the thesis.

I also declare that the intellectual content of this thesis is the product of my own work, except to the extent that assistance from others in the project's design and conceptions or in style, presentation and linguistic expression is acknowledged. I have also submitted a digital copy of this thesis

Word count excluding references, tables and captions: 9183
In the style of *Sedimentary Geology*

Geordie Donaldson Date: 31/5/2016

Thesis committee (type out their names, not signatures):

Supervisors	Prof. James Goff
	Dr. Catherine Chagué-Goff
Examiners:	Associate Professor Rob Brander
	Dr John Triantafilis

I am fully aware that the School retains a copy of the thesis and is free to allow them to be consulted or borrowed. The thesis may be restricted for up to 2 years or longer by a written request to the Head of School.

Abstract

The largest historical tsunami to occur in New Zealand was a 15 m high wave caused by a landslide into the Waikari River, Hawke's Bay. The landslide was triggered by groundshaking due to the 1931 Hawke's Bay Earthquake, New Zealand's deadliest natural disaster to date. Although a memoir and a newspaper report from the time describe the tsunami that destroyed the homestead and sheep shed on Waikari Station, this research is the first to examine the 1931 tsunami using a multiproxy approach aimed at investigating the physical evidence of this event. The stratigraphy was recorded throughout the site, and cores and grab samples collected for further analysis. This was used in conjunction with LiDAR data and historical documents to establish a detailed record of both the landslide and the resulting tsunami.

This study revealed the presence of an anomalous gravel layer within the sedimentary sequence of Waikari Station, which was subjected to sedimentological, geochemical, chronological and microfossil analyses. Extrapolation from ^{137}Cs data coupled with historical artefacts suggests that this layer, which is characterised by a large increase in grainsize and a decrease in sorting, was deposited by the 1931 event. Diatom taxa from within the deposit displayed a preference for environments with higher salinity, and contained a high proportion of broken frustules compared to those found in the surrounding soils, suggesting deposition from a high energy, turbulent flow. Principle component analysis (PCA) was performed on geochemical data in order to detect trends in elemental counts. This showed the anomalous gravel layer at all sites is associated with a cluster of elements not related to detrital inputs nor organic matter, and is believed to have originated from the tsunami.

A second, older, gravel layer was identified. This is considered to have been deposited by an earlier tsunami, quite likely caused by a landslide generated by the AD1863 Hawke's Bay earthquake - the deposit has similar sedimentological, geochemical and microfossil characteristics to the gravel layer deposited by the 1931 event. Given that there appear to be repeated tsunamis associated with earthquake-generated landslides in the area, the implications and risks for the wider region are discussed, in addition to identifying two locations where similar events may have occurred or will occur in the future.

Acknowledgements

Firstly I would like extend a massive thank you to my supervisors, Prof. James Goff and Dr. Catherine Chagué-Goff. Their support across all facets of this project was always forthcoming, and their dedication to this project and the countless hours of work they both put into it are immensely appreciated. I am very grateful to have had the opportunity to work with them, not just on this project but also on the Chile project in my third undergraduate year, as well as the New Zealand field trip. Their unfaltering commitment to tsunami science is inspiring.

Thank you to the Hawke's Bay Regional Council for providing a grant to fund fieldwork and for their assistance in sourcing resources. In particular, I would like to thank Lisa Pearse and Craig Goodier for all their assistance before and during the fieldwork. Thank you, also, to Guy Denver for granting us access to his land for fieldwork, as well as for sourcing historical documents and allowing them to be read and copied.

Thank you to the ANSTO Rad team for their assistance in the irradiation of samples that were imported from New Zealand. Big thanks to Patricia Gadd for carrying out the ITRAX analysis and Daniela Fierro and Atun Zawadzki for carrying out ^{210}Pb and ^{137}Cs dating.

Thanks are also due to the Australian Institute of Nuclear Science and Engineering (AINSE), which generously supported this research through the AINSE Honours Scholarship Program.

Thank you to Claire Kain for writing the original R Studio scripts used in the geochemical analysis.

Thank you to Selena Shannon for editing help and advice.

Table of Contents

1.0 Introduction

With the expansion of coastal populations the risk to both human life and property posed by tsunamis is ever increasing. To reduce potential damage a better understanding of the mechanisms, magnitude and frequency of these events is needed and it is therefore important to create comprehensive databases that incorporate as much data as possible (Dunbar and McCullough, 2012; Goff and Chagué-Goff, 2012). The construction of such a database is possible partly due to the preservation of tsunami signatures within the sedimentary record of low energy depositional environments. The analysis of such sedimentary sequences can yield valuable evidence concerning the nature (e.g. source, timing, characteristics) of unrecorded or poorly understood tsunamis (e.g. Atwater, 1987). However, any single line of evidence can prove ambiguous therefore a multi-proxy approach is generally adopted in order to differentiate a tsunami deposit from other types such as storm deposits (e.g Goff et al., 2004; Chagué-Goff et al., 2011). Broadly speaking this generally means analysis of the sedimentary, geochemical, archaeological and biotic signatures (Goff et al., 2010). As more events are studied knowledge of these proxies also increases, thereby allowing a better understanding of past events. This in turn results in the ability to detect a greater variety of tsunami signatures such as those related to small events or those close to the maximum point of inundation that leave negligible sedimentary records (Chagué-Goff et al., 2011; 2015).

While the ability to identify a wider variety of tsunami deposits is increasing, there are some notable deficiencies in our current understanding of these events. For example, little is still known about locally-generated tsunamis, such as those caused by landslides, largely because they are less well documented and the affected areas tend to be much smaller than those of region- or ocean-wide events (Liu et al., 2004; Viroulet et al., 2013). Furthermore, studies of non-marine sourced tsunami deposits are rare (e.g. Dirksen et al., 2011). Locally-generated tsunamis have the potential to produce a much higher local run-up than their more geographically extensive counterparts, due to being in close proximity to the generating mechanism (e.g. Fritz et al., 2003a; 2003b). As a result they can be significantly more devastating over relatively small areas (e.g. Miller, 1960). The study of these events is therefore important to help us better understand tsunami signatures, identify potential threats and mitigate the risk to populations where these events could occur (Bolin et al., 2014). This is particularly true for an environment such as New Zealand where landslide-prone hills and mountains are subjected to regular large earthquake events, often in close proximity to large water bodies (Goff et al., 2001; Clark et al., 2015).

The 1931 Waikari River Tsunami was New Zealand's largest historical tsunami with a reported wave height of 15 m (Tait, 1977). The landslide which generated this tsunami resulted from severe ground shaking caused by the 1931 Hawke's Bay Earthquake (M_S 7.8) (Smith, 1978). While historical documents in the form of a memoir from the station owners (Tait, 1977) and a newspaper report (Auckland Star, 1931) describe general details about the cause and damage, no research has been carried out to better understand the nature and extent of this locally-generated event.

The aims of this project are to, a) identify and determine the extent of sediments related to the 1931 Waikari River Tsunami, b) provide a better understanding of the nature of the generating mechanism and, c) provide information to help better understand whether such locally-sourced events are more widespread within the region.

These aims will be addressed by using a multiproxy approach to study the geomorphology of the area and a number of properties of the sediments deposited by the tsunami:

- Analysis of the stratigraphy and sedimentary characteristics both within and bounding the tsunami deposit will help characterise the nature of the deposit (Morton et al., 2007; Chagué-Goff et al., 2012).
- Geochemical analyses will help identify the potential source sediments (Chagué-Goff, 2010).
- Diatom characteristics, including the species present, their environmental preferences and condition, will be studied to assist in finding evidence for inundation (Hemphill-Haley, 1996; Dura et al., 2016).
- LiDAR data, field observations and historical documents will be used to estimate the size and classify the movement type of the tsunami-generating landslide.
- Other potential local sources of a similar nature will be identified.

2.0 Geological Setting and Site Description

2.1 Geology

New Zealand sits astride the boundary between the Australian and Pacific Plates. The Taupo-Hikurangi Subduction System itself is located within the southern extension of the Tonga-Kermadec Arc System (Figure 1a), a system formed by the subduction of the Pacific Plate under the Australian Plate (Reyners, 1980). In the Hawke's Bay area, the Pacific Plate is subducting at an angle of around 10-12 degrees with the collision point of the two plates located ~130 km east of the study site (Cole and Lewis, 1981). The subduction zone makes the area prone to tectonic activity, as evidenced by events such as the M_S 7.8 1931 Hawke's Bay Earthquake (Smith, 1978).

The source of the 49 km long Waikari River is in the Maungaharuru Ranges (Figure 1b) which is located in the Frontal Ridge of the Taupo-Hikurangi Subduction System and consists of faulted greywacke-argillites (Pillans, 1986). To the east is the Forearc Basin (Figure 1a) in which the study area is located. This basin consists of a layer of mostly marine Plio-Pleistocene sediments (Bannister, 1988).

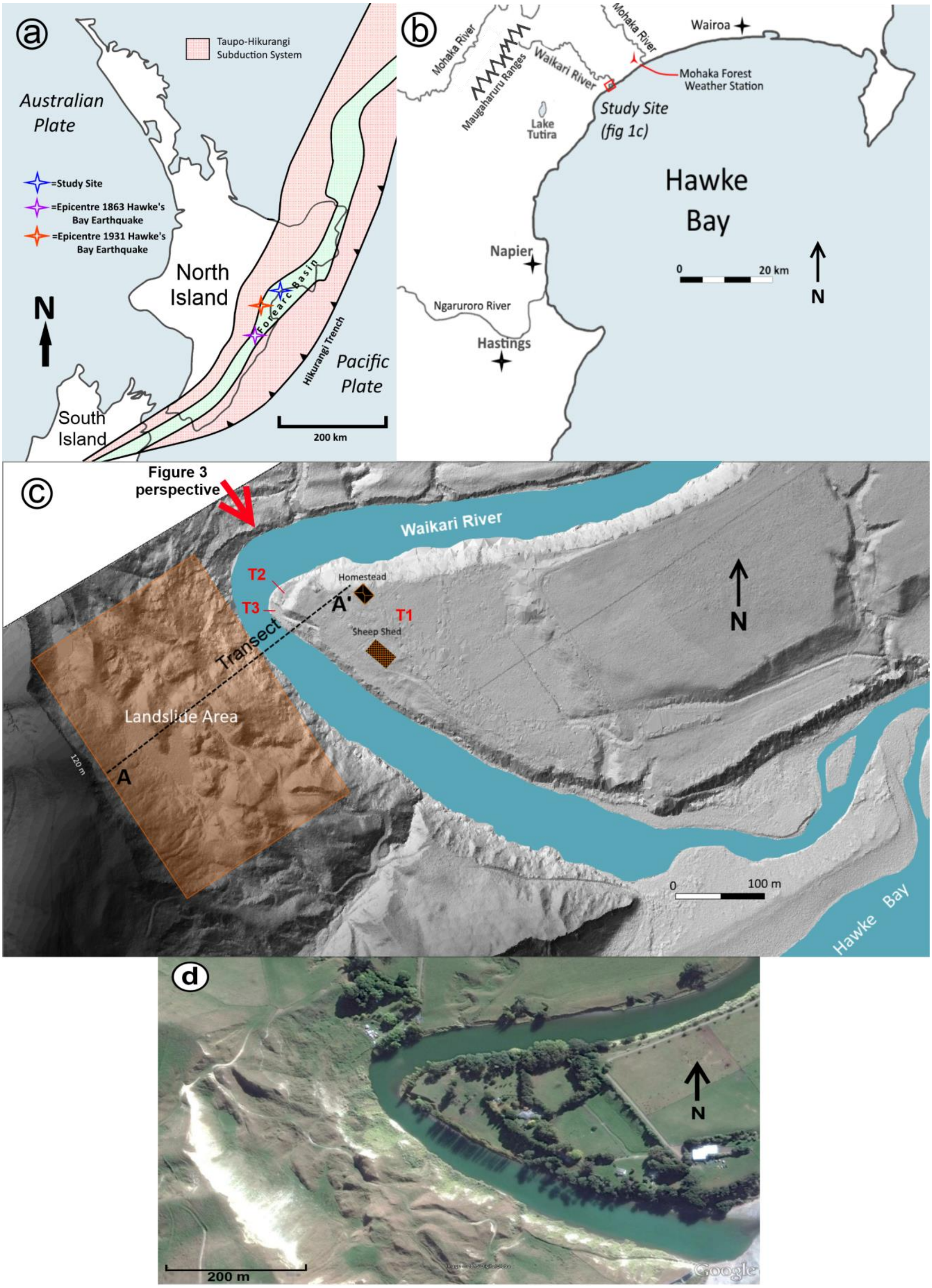

Figure 1 a) Location of the study site and the epicentre of the 1863 and 1931 Hawke's Bay Earthquake (Stirling et al., 1998; Bullen, 1938) within the Forearc Basin of the east coast of the North Island of New Zealand (After Hull, 1990). b) Hawke's Bay region, showing the location of major rivers and towns. c) Study site at the mouth of the Waikari River with locations of the 1931 homestead and sheep shed, landslide area and topographic transect shown in Figure 4 (dashed line between A and A'). T1, T2 and T3 (red) represent the three terraces on the site. The perspective of Figure 3 is also labelled. Image made from LiDAR data. d) Satellite image of the study site (Google Earth).

2.2 1931 Hawke’s Bay Earthquake

The M_s 7.8, Hawke’s Bay Earthquake occurred on the 3rd February 1931 at 10.17 am local time. The epicentre was located at 39^{o}19’48”S 176^{o}35’60”E, 32 km NW of Napier (Figure 2) (Bullen, 1938). Groundshaking led to widespread destruction of the buildings and infrastructure of Hastings and Napier, resulting in the deaths of 256 people, making the 1931 Hawke’s Bay Earthquake New Zealand’s deadliest natural disaster (e.g. Hill and Gaillard, 2013; Hawke’s Bay Emergency Management Group, 2015). Modelling of the focal point suggests it was a slip of a steeply dipping reverse dextral fault at a depth of 16-24 km (Hayes, 1936). The earthquake was comprised of three main shocks, spanning 14 seconds (Davison, 1934).

The three main shocks caused large amounts of surface deformation, creating a north-east trending elongated dome, 90 km long and 70 km wide (Figure 2) (Gibowicz, 1973). The maximum uplift of 2.7 m was recorded near Old Man’s Bluff. Post seismic collapse also occurred in areas of coseismic subsidence with these drops equating to 10-20% extra downwards movement (Hull, 1990).

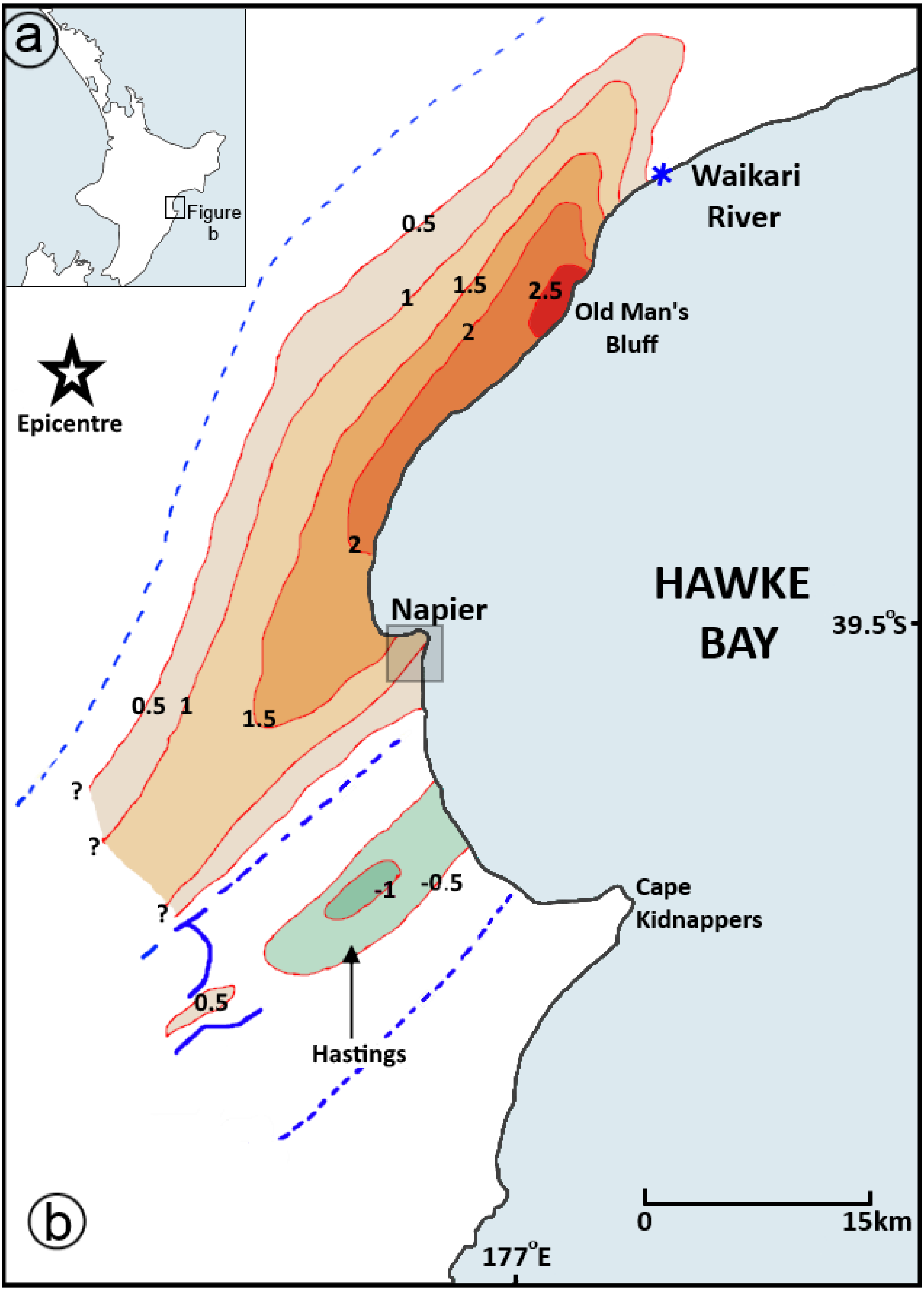

Figure 2: a) North Island of New Zealand. b) Uplift and subsidence as a result of the 1931 Hawke's Bay Earthquake, the epicentre is shown with a star. Continuous blue lines show known surface faulting, dashed blue lines show implied faulting, orange lines represent contours height change with brown-red and green indicates uplift and subsidence, respectively. Adapted from Hull (1990).

2.3 Climate

The climate of Hawke’s Bay is oceanic (Cfb) as defined by the Köppen Climate type (Kottek et al., 2006). This means that Hawke’s Bay has slight variations in seasonal rains and a relatively narrow temperature range. Annual rainfall at the Mohaka Forest weather station, located approximately 10 km north east of the field site (Figure 1b), is 1365 mm per annum - much of which can fall as heavy rain over short periods of time with the area being prone to both thunderstorms and ex-tropical cyclones (Chappell, 2010).

2.4 Study Site

The study site is on the east bank of the Waikari River, approximately 700 m upstream from the mouth of the river where it bends (meanders), changing to a south easterly heading. Just before the river drains into the bay it once again turns and narrows as it encounters a spit (Figure 1c). This spit, created by longshore drift, varies in height and width with time. The width of the river fluctuates from 35 m at the main bend to 70 m downstream immediately prior to narrowing where it encounters the spit. There are three distinct fluvial terraces on the land to the east of the meander bend, the highest (T1) of which is approximately 10 m above the river level while the others are 1.5 m (T2) and 0.5 m (T3) above the river, respectively (Figure 1c). The top terrace is relatively flat and has been cleared for use as a horse paddock. The main bend, where the river changes from a westerly to south easterly direction, has resulted in undercutting and oversteepening of the adjacent loess hills (Figure 1c). The adjacent hill immediately to the west of the river bend, directly opposite the terraces, rises to an elevation of 120 m above sea level at a distance of some 250 m from the western bank.

Waikari Station is situated on the eastern side of the river within the study area (Figure 1c). In 1931 there were two buildings on the station, a homestead, located approximately 80 m from the river and a sheep shed, about 30 m from the bank (Figure 1c and Figure 3). Both buildings were destroyed by the 1931 Waikari River Tsunami (Tait, 1977).

3.0 Methods

3.1 Sampling

A survey was carried out in early July 2015 around the final permanent bend of the Waikari River. Trenches were manually excavated at various locations on the Waikari Station side of the river to display the stratigraphy in full at selected trenches. Stratigraphy, physical properties and features of the sediment were recorded. GPS locations of all sites were taken with a Garmin eTrex® H handheld GPS and cores were taken from six of the seven trenches dug (WR006 excluded). These cores were: WR005 (50 cm), WR007 (33 cm), WR008 (50 cm), WR009 (45 cm), WR010 (48 cm) and WR011 (50 cm) (Figure 3). This was done by pushing longitudinally cut PVC pipes, ranging in diameter from 7 to 10 cm, into the trench walls.

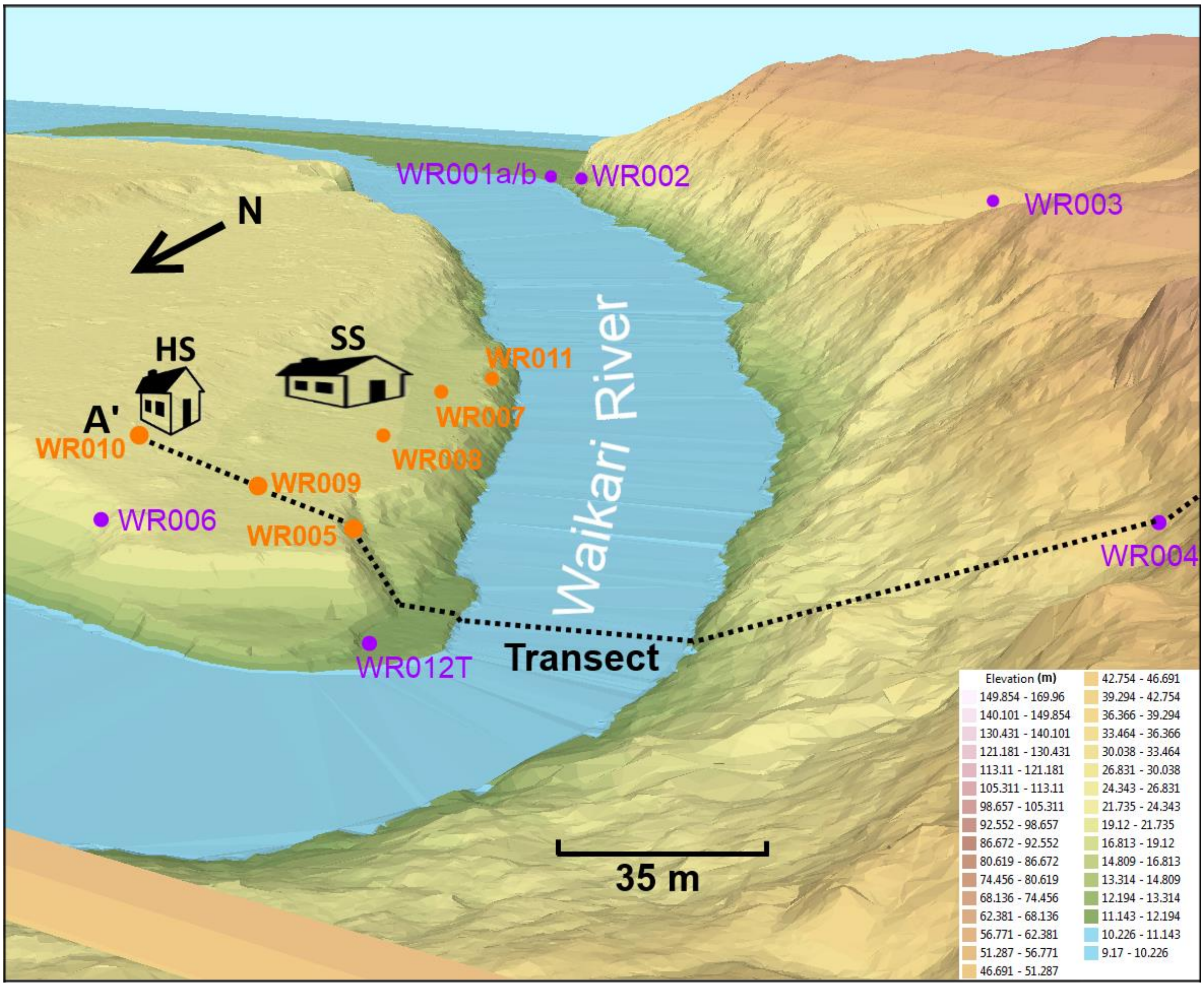

Figure 3: Location of the trenches (orange) and grab samples (purple). 'HS' represents the location of the homestead, 'SS' represents the location of the sheep shed, both destroyed in 1931 Dashed line displays transect, 'A' is further west along transect (see Figure 1c for location)

Six grab samples of approximately 100 g, representative of local sediments, were taken throughout the site including: four on the south western side of the river and two from the east (Figure 3). Samples were bagged, locations noted on GPS and context photographs taken of the surrounding stratigraphy and landscape.

A shallow gravel layer was identified in trenches closest to the river and its areal extent was recorded by probing with a metal rod throughout the study area along a series of transects. The edge of the layer was recorded by GPS.

A transect was taken south west to north east (A-A') throughout the study site using a TruPulse 360 Laser Rangefinder, with an accuracy of ±0.1 m. The transect encompassed the top of the failed slope on the far side of the river, though sites WR004, WR005, WR009 and ending at WR010 (Figures 1c and 4).

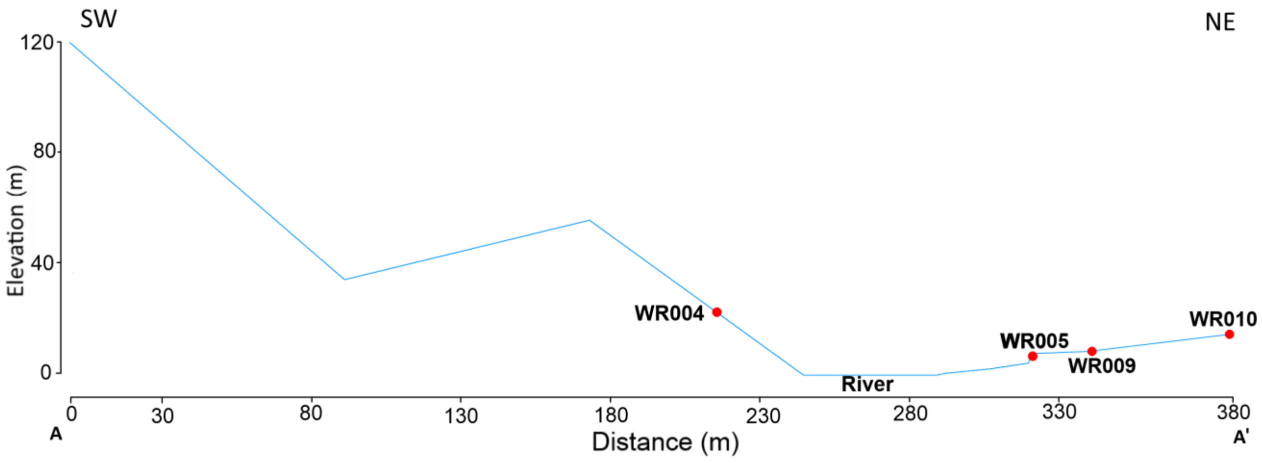

Figure 4: Transect across the study site, south-west to north east. Showing sample locations included in transect (see Figure 1c and Figure 3).

All sediment samples were shipped to the Australian Nuclear Science and Technology Organisation (ANSTO) and irradiated. Cores were cleaned before being described using a modified version of the Troels-Smith classification system (Kershaw, 1997), then scanned with the ITRAX Core Scanner before being transported to UNSW for further analysis. Figure 5 provides a summary of the analyses conducted and depths on each core.

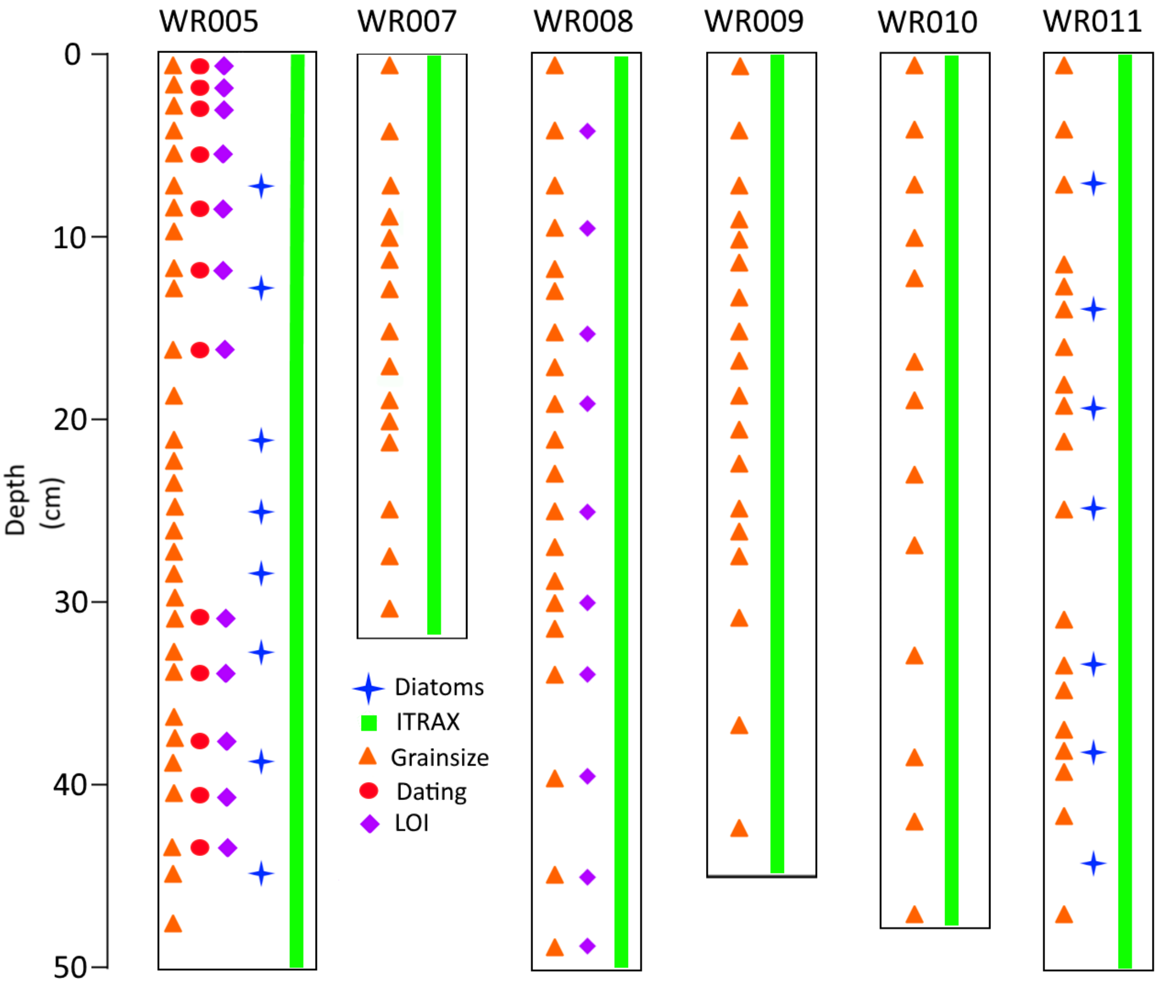

Figure 5 Summary of the analyses conducted on each core

3.2 ITRAX

Geochemical and magnetic susceptibility analyses were carried out using the ITRAX Core Scanner at ANSTO. Optical and radiographic images of the cores were also acquired. This non-destructive technique gives data in the form of counts, a ‘semi-quantitative’ value for the elemental composition (Croudace et al., 2006). Optical and radiographic images were acquired and the cores scanned with a step size of 1 mm. Magnetic susceptibility was then measured in 5 mm intervals. The resulting data were processed in Microsoft Excel and readings with kilo counts per second (KCPS) <40000 (usually the first and last few mm of the core) were removed. Elemental counts were then normalised over KCPS to correct for variation in porosity and matrix (e.g. Bouchard et al., 2011). Finally, data were imported into

RStudio where normalised count vs depth graphs were produced and data processed by principle component analysis (PCA).

ITRAX analysis was also carried out on grab samples taken from around the site. These data were also imported into RStudio where Spearman's rank correlation coefficients were calculated between the count values of the grab samples. This allowed the chemical similarity of the grab samples to be assessed.

3.3 Grainsize

Grainsize analysis was carried out using a combination of sieving and laser diffraction. Sub-samples (between 0.5 and 1.5 g) were taken throughout all the cores (Figure 5) and digested with 30% hydrogen peroxide (H_2O_2) to remove the organic matter (Di Stefano et al., 2010). Sodium hexametaphosphate was added to prevent flocculation and samples were sonicated (Sperazza et al., 2004). Samples in which <5% of the clasts were over 2 mm were analysed using a Malvern Mastersizer 2000.

Samples in which more than 5% of the clasts had an *a* axis >2 mm were resampled to obtain a larger sample for sieving. The new subsamples (between 3 – 15 g) were digested with H_20_2, dried and weighed. Samples were sieved at 2, 1.7, 1.4 and 1 mm with a Haver EML Digital Plus Sieve for 10 minutes before each portion was re-weighed with an A&D ED-182A balance. The portion of the sample with an *a* axis <1.4 mm was analysed with the Malvern Mastersizer. Measurements of the *a*, *b* and *c* axes of clasts >2 mm were performed with Vernier calipers.

Data from manually measuring, sieving and laser diffraction were consolidated in Microsoft Excel using a modified version of Dinis and Castilho's (2012) method for integrating sieving and laser data. Results were then imported into GRADISTAT (Blott and Pye, 2001) where the Folk and Ward (1957) method was used to obtain values for mean, sorting and skewness in µm and gravel, sand and mud portions which were graphed in RStudio.

3.4 Loss-on-Ignition (LOI)

Loss-on-ignition (LOI) was carried out on two cores to quantify the relationship between organic content and the ratio of incoherent and coherent scattering of molybdenum (referred to as either: Mo(Inc/coh) or Mo-ratio) as measured by the ITRAX core scanner (e.g. Chagué-Goff et al., 2016). Mo-ratio acts as a proxy for the organic content of the material as samples high in organic matter tend to be composed of lighter elements, resulting in more incoherent scattering of the Mo. Heavier elements cause more coherent scattering, leading to a lower Mo(Inc/coh) ratio (e.g. Guyard et al., 2007).

LOI is a well-established technique for determining organic content following the methods of Dean (1974) and Heiri et al. (2001), but is undertaken at a much lower sampling resolution than can be achieved using the ITRAX core scanner. Sub-samples of around 0.5 cm^3 of material (from a 1 cm core depth range – Figure 5) were taken and their initial mass recorded. These were dried overnight at 105^{o}C and then ashed at 550^{o}C in a muffle furnace for 4 hours and results provided on a dry weight basis (DW$_{550}$). The following formula was then applied to determine the LOI$_{550}$ (Heiri et al., 2001):

$$LOI_{550} = \frac{100(DW_{105} - DW_{550})}{DW_{105}}$$

LOI and Mo(Inc/coh) data were compared by plotting the LOI value against the average Mo(Inc/coh) value over the relevant centimetre core depth in RStudio before running a linear regression model and assessing the goodness of fit of the line to the data.

3.5 ^{210}Pb/^{137}Cs Dating

^{210}Pb/^{137}Cs dating was carried out on subsamples of ~3 g each taken from core WR005, which were oven dried at 60^{o}C and crushed into a fine powder. They were then sent to ANSTO where they were analysed after 3 weeks in an HPGe gamma spectrometry well detector. The ^{210}Pb method uses the difference in equilibrium of activities of the radioisotopes ^{210}Pb and ^{222}Rn to date sediments up to ~130 years (Appleby and Oldfield, 1978). ^{137}Cs which was measured simultaneously, can be used for chronological comparison with ^{210}Pb results by cross-referencing with the peak ^{137}Cs concentration. ^{137}Cs occurs in measurable quantities in the soil from the mid-1950s due to the increase of atmospheric nuclear weapons testing (Schuller et al., 1993; Leslie and Hancock, 2008). ^{137}Cs activity peaks in sediments in 1963 or 1964 before the Nuclear Test Ban Treaty in 1963 (Pennington et al., 1973; Carter and Moghissi, 1977).

3.6 Diatoms

Diatom samples from cores WR005 and WR011 (Figure 5) were prepared following Renberg's (1990) method in conjunction with a control sample to check for contamination. Sediment samples were digested in 30% H_2O_2 to remove any organic matter. A few drops of 10% HCl were then added to remove carbonates and iron precipitates and the samples left to settle overnight. The supernatant was pipetted off and distilled water was added before the samples were then centrifuged at 1000 RPM to remove fine sediment. Centrifuging was repeated until all fine sediment was removed. A few drops from each sample were mounted onto microscope slides with Naphrax. If possible, counts of at least 250 diatom frustules were made per slide under 400x magnification with a Kyowa Optical microscope. Species identification and environmental preferences were determined with reference to the standard floras described in Van der Werff and Huls (1957–1974). Counting and identification of diatoms were performed by Professor James Goff.

3.7 Landslide Size

An estimation of the landslide size was undertaken using LiDAR data from Hawke's Bay Regional Council, analysed in ARC GIS. Digital elevation models made from LiDAR data can be used to predict (Jones, 2006) or establish landslide slide volumes (e.g. Jaboyedoff et al., 2012). The approach used in this study was to calculate the volume difference between the side of the hill which failed and the intact adjacent hillside. This was achieved by defining the extent of the surface of the intact hill slope then calculating the volume between this surface and a plane fixed at the elevation of the base of the hill. A polygon with the same shape and area was laid on the failed side of the hill. The volume between the failed surface and the original plane was then calculated. This gave approximate volumes for the hill before and after the landslide event.

To quantify the error in this assumption the same analysis was carried out on surrounding hills, assessing the volumes of both flanks of each hill. These data were used to assess the volume variation between flanks to determine an appropriate value for error.

4.0 Results

4.1 Stratigraphy and Grainsize

In general, throughout the study site, the broad brush stratigraphy consists of a lower unit of yellow-grey cemented loess. This is mostly overlain by a brown (black) silty soil (around 35 to 60 cm depth) which generally increases in organic matter towards the surface. Details of sample locations can be found in Appendix A.1 and grainsize data obtained using Gradistat can be found in Appendix A.2. Detailed site specific stratigraphic information is given below.

4.1.1 WR005

The base of core WR005 consists of a silty black soil (60 cm depth; underlain by the cemented loess although this was not collected in the core). There is a sharp upper contact at 30 cm depth with a 2 cm thick gravel layer (Figure 6). The well rounded gravel clasts have an average *a* axis length of 10 mm and sit within a grey silty sand matrix. This unit is overlain by a 13 cm thick layer of light brown sandy-silt which grades upwards into a uniform darker brown silty soil at 14 cm depth, extending to the surface.

The mean grainsize is relatively consistent throughout the core with the exception of a marked increase within the gravel layer. Clasts become less well sorted within the gravels and X-Ray imaging shows an increase in density of the core within this layer (Figure 6).

LOI and Mo-ratio, both indicators of organic content (plotting LOI vs Mo-ratio gives an r^2 value of 0.90, demonstrating that the Mo-ratio is a good proxy for organic content as also proposed by Chagué-Goff et al. 2016), show similar trends throughout WR005 (Figure 6). Both show high levels of organic matter at the base of the core, reaching a minimum within the gravel layer before increasing towards the surface. Full LOI data can be found in Appendix B.

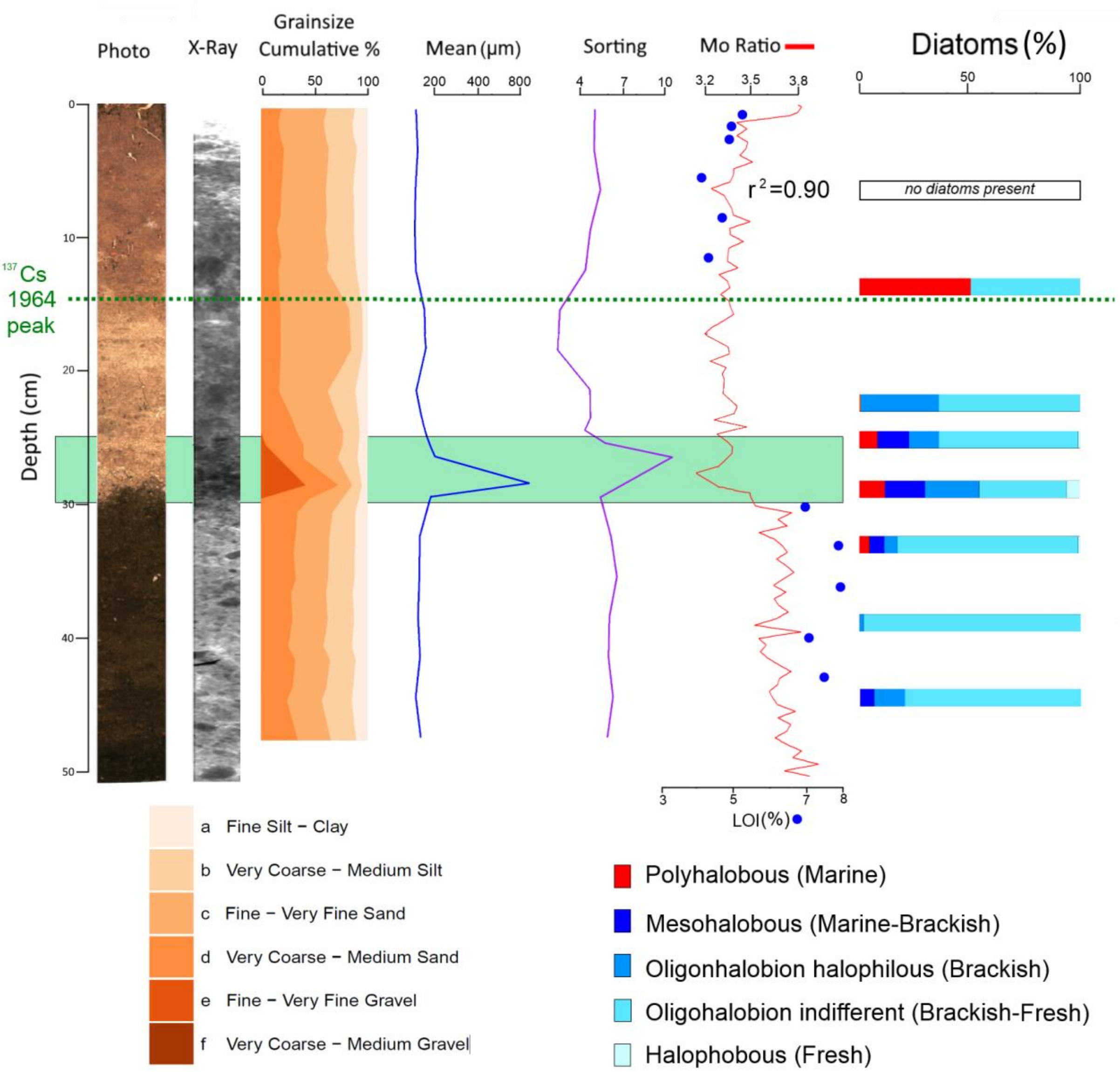

Figure 6: Stratigraphy for core WR005. From left to right: Photo, X-Ray, cumulative grainsize plot, mean grainsize (µm), sorting (Folk and Ward method), Mo-ratio (red line), LOI (%, blue dots) and diatom species salinity preferences (%). Green shaded area shows the location of the anomalous gravel layer while the dashed line shows the 1964 peak of ^{137}Cs activity. The r^2 value shows the strength of the relationship between Mo-ratio and LOI.

4.1.2 WR006

No core was taken from site WR006 however the stratigraphy was recorded and photographed *in situ* (Figure 7). The base of the site consists of a yellow loess material which grades into a dark black, organic-rich soil at ~38 cm depth. This is overlain by an 11 cm thick gravel layer between ~7 and 28 cm. Within the gravel layer clasts were evenly distributed and ranged in size from an *a* axis length of 10 to 250 mm. The matrix is comprised of a coarse grey sand. Around 7 cm depth is a diffuse upper contact with a grey-brown silty soil which continues to the surface.

Figure 7: Trench of WR006 including close up of gravel deposit. Markers in the right hand image as well as the green dashed lines in both images display the top and bottom of the gravel layer.

4.1.3 WR007

Site WR007 consists of a brown silty soil which becomes darker towards the surface (Figure 8). Three pebbles with *a* axes of 20, 15 and 10 mm were found at depths of 15, 17.5 and 12.5 cm, respectively. Mean grainsize was at a maximum in the anomalous layer with sediments becoming less sorted up the core. The organic matter gradually increases towards the surface, reaching a maximum in the top few centimetres.

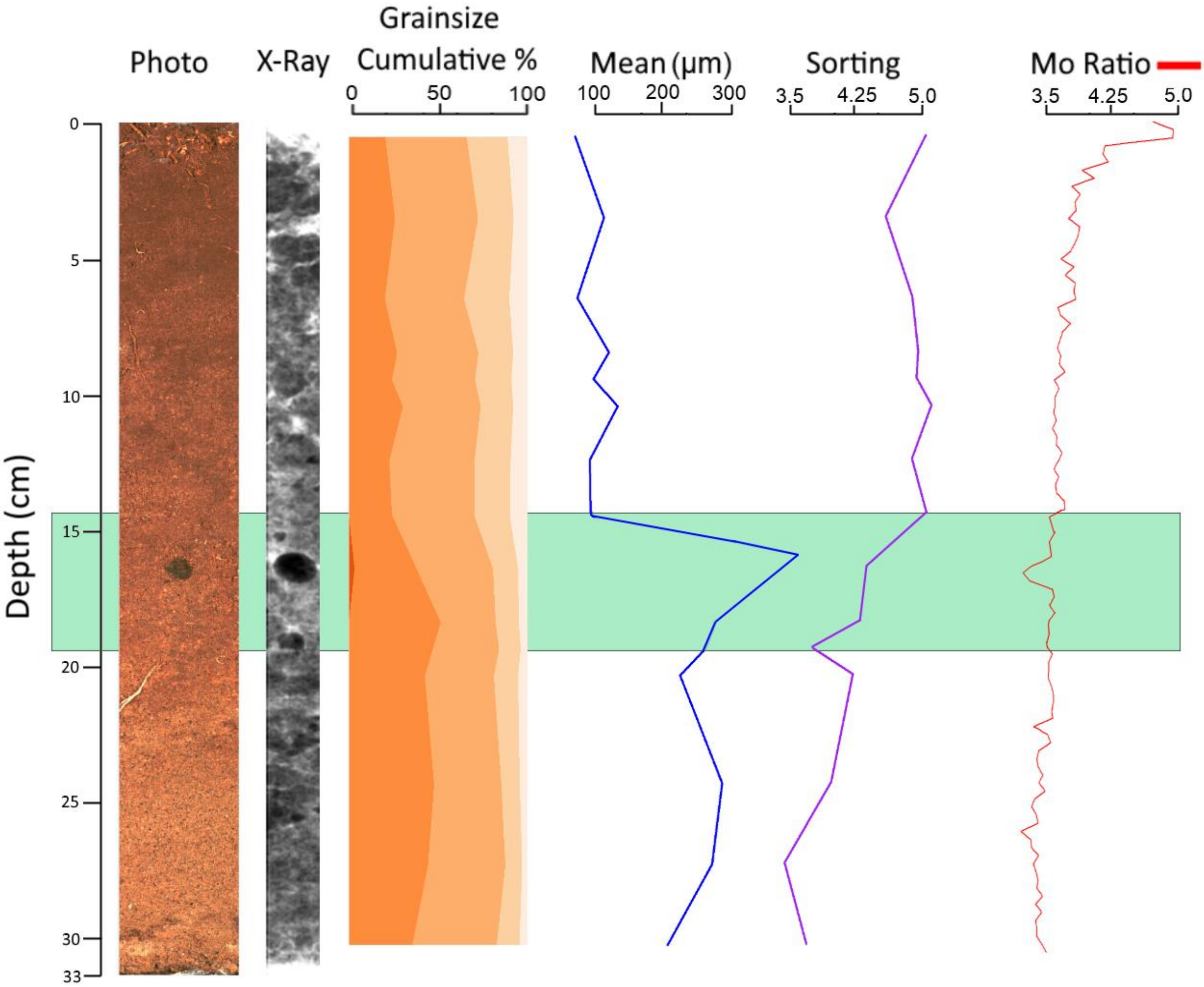

Figure 8: Stratigraphy of core WR007. From left to right: Photo, X-Ray, cumulative grainsize plot, mean grainsize (μm), sorting (Folk and Ward method), Mo-ratio (red line). Green shaded area shows location of possible anomalous layer. Refer to Figure 6 for key to cumulative grainsize plot.

4.1.4 WR008

The lowest unit in WR008 is an orange loess which at ~30 cm depth grades into a black silty soil. Mean grainsize decreases upcore throughout this unit from 50 cm, reaching a minimum at 24 cm (Figure 9). Between 15 and 9 cm depth, mean grainsize increases in what appears to be a gradational contact between the black silty soil below and the overlying brown silty soil.

LOI and Mo-ratio are in good agreement, showing organic matter being lowest at the base of the core and gradually increasing upcore. The r^2 value of a plot of LOI vs Mo-ratio is 0.96, reinforcing that Mo-ratio is a good proxy for organic content.

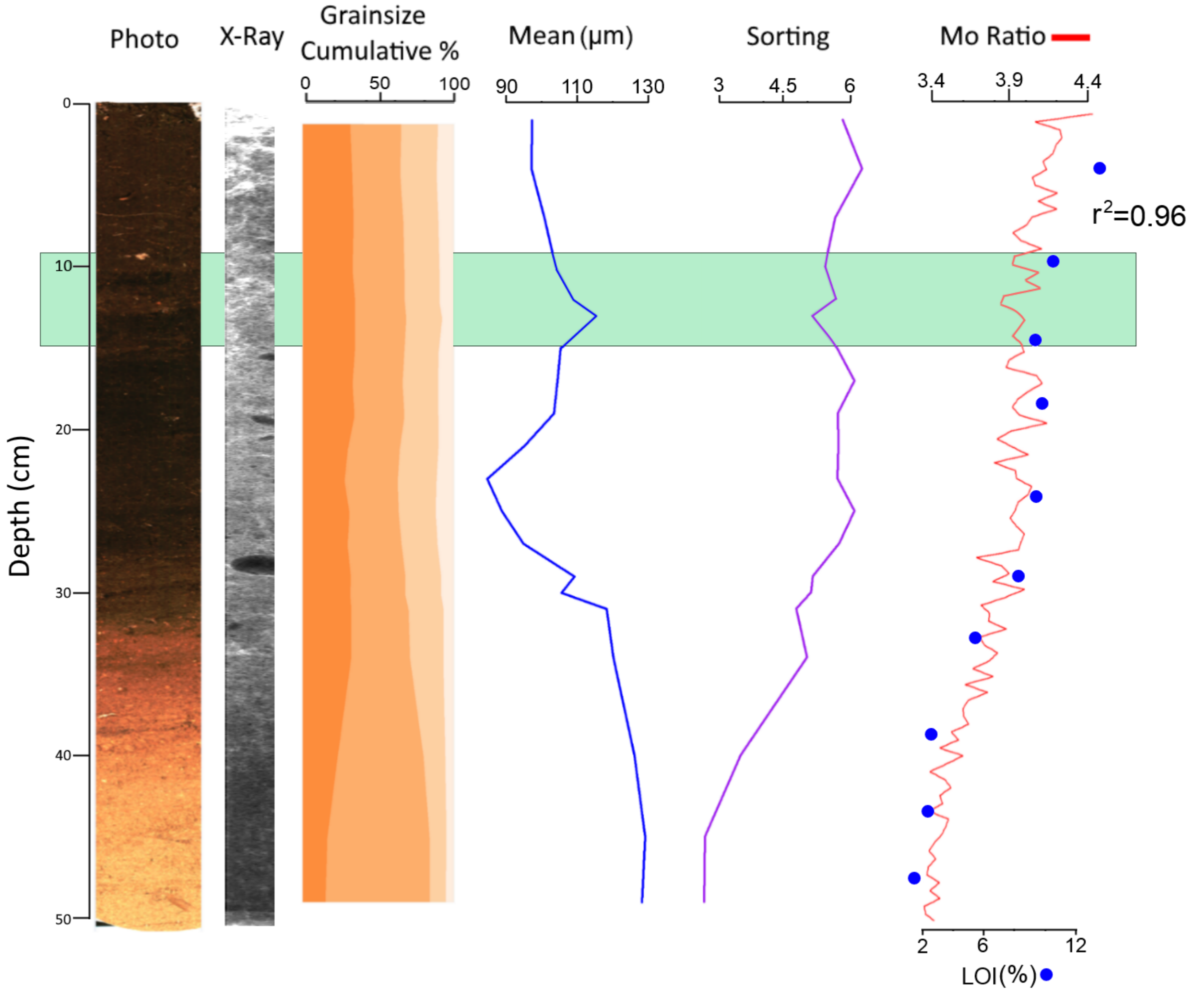

Figure 9: Stratigraphy of core WR008. From left to right: Photo, X-Ray, cumulative grainsize plot, mean grainsize (µm), sorting (Folk and Ward method), Mo-ratio (red line) and LOI (%, blue dots). Green shaded area shows location of possible anomalous layer. The r^2 value shows the strength of the relationship between Mo-ratio and LOI. See Figure 6 for the key for the cumulative grainsize plot.

4.1.5 WR009

The lower unit at WR009 consists of a black silty soil with orange mottling near the base (Figure 10). The upper contact of this unit to an overlying pebbly unit at 23 cm depth is gradational. Pebbles within this 8 cm thick layer are grey, rounded, and have *a* axes ranging between 10 and 30 mm. There were ~25 pebbles in a 10x10 cm area, set in a matrix of grey-brown sand. A single clast with an *a* axis >250 mm was also found in this layer along with two iron roofing nails and some broken crockery, which are most likely to be debris from the 1931 homestead (Figure 11). The layer between the top of this unit, at 15 cm, and the surface consists of a light brown silty soil.

Mean grainsize is consistent throughout with the exception of a marked peak that occurs within the gravel layer between 15 and 23 cm. The sediments within this range also display a lower sorting and decrease in organic matter content.

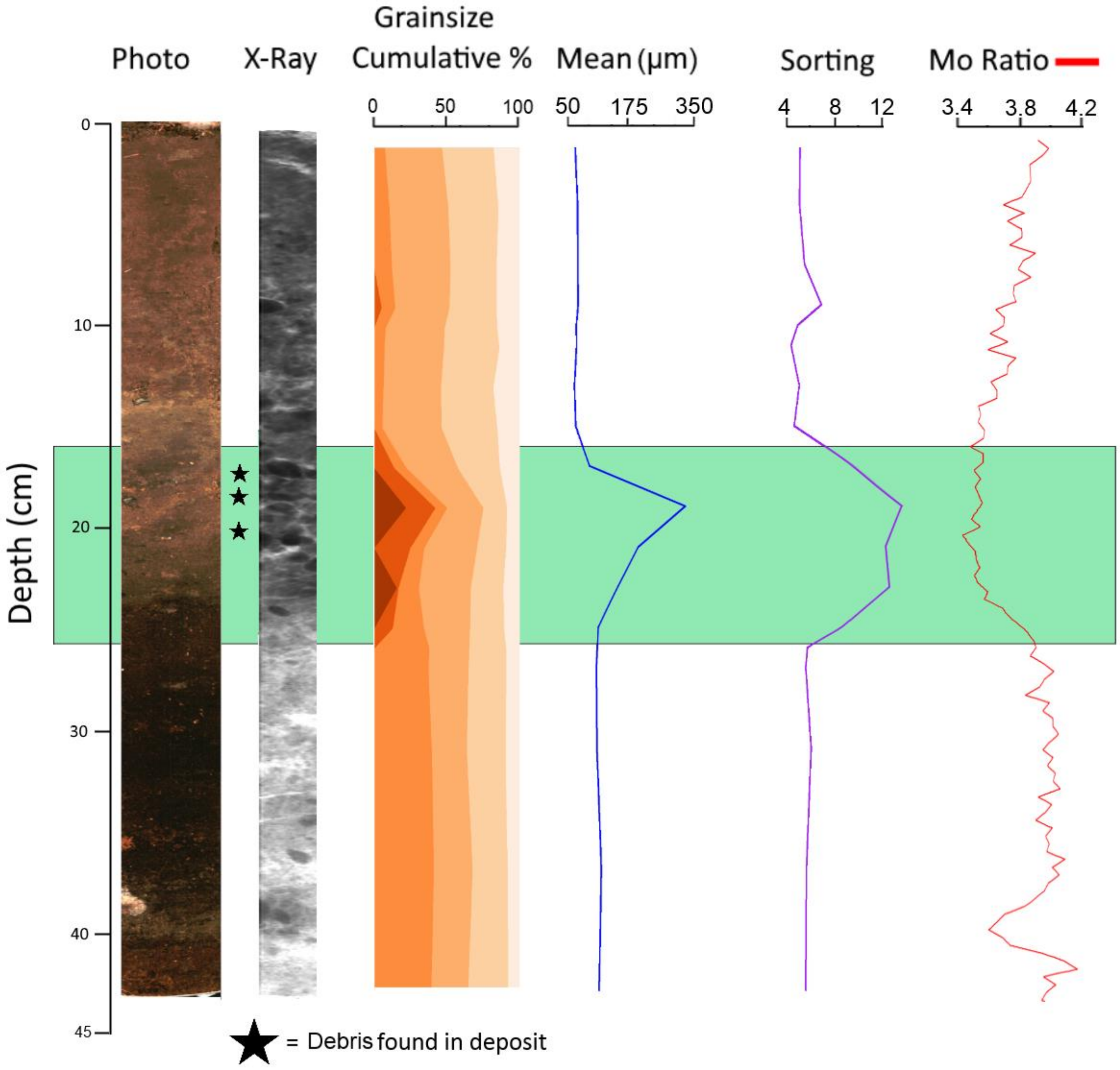

Figure 10: Stratigraphy of core WR009. From left to right: Photo, X-Ray, cumulative grainsize plot, mean grainsize (µm), sorting (Folk and Ward method) and Mo-ratio (red line). Green shaded area shows location of anomalous layer. Stars represent the depths at which two roofing nails and a piece of broken crockery (Figure 11). Refer to Figure 6 for the key to the cumulative grainsize plot.

Figure 11: Two nails and piece of broken crockery found within the anomalous pebble layer in core WR009.

4.1.6 WR010

The base of core WR010 consists of an orange loess which grades at around 42 cm depth into a dark black silty soil, exhibiting orange banding around the contact (Figure 12). The black silty soil contains small (~1 mm *a* axis) clasts of orange-brown pumice lapilli. There is a 2 cm thick gradational contact from 13 to 11 cm depth between the black silty soil below and the overlying dark-brown silty soil. Within the contact there is an increase in grainsize and decrease in sorting, before a general decrease in grainsize throughout the overlying dark-brown soil up to the surface. Organic matter content is relatively constant throughout the core with a marked increase in the top few centimetres.

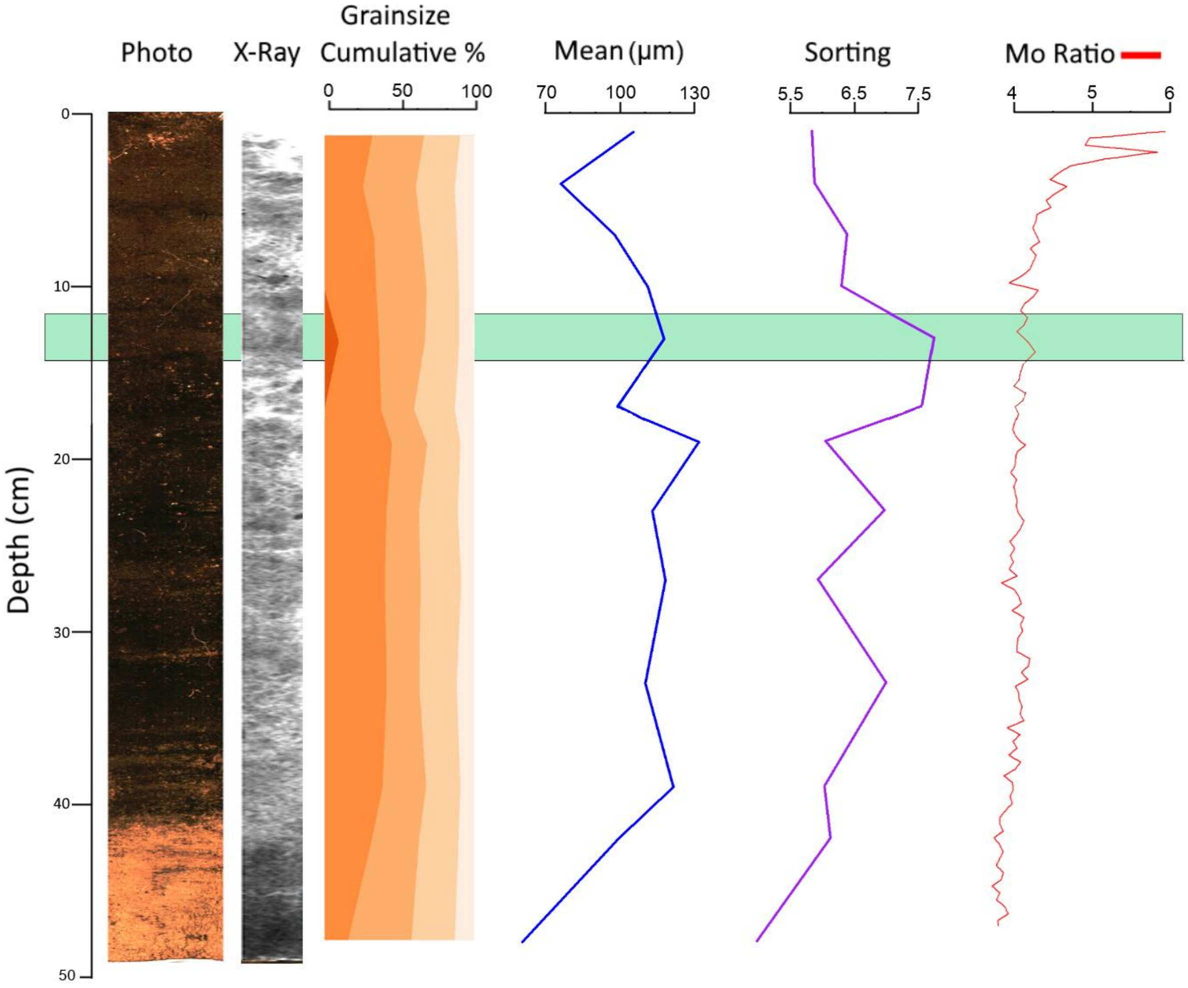

Figure 12: Stratigraphy of WR010. From left to right: Photo, X-Ray, cumulative grainsize plot, mean grainsize (µm), sorting (Folk and Ward method) and Mo-ratio (red line). Green shaded area shows location of possible anomalous layer. Refer to Figure 6 for the key to the cumulative grainsize plot.

4.1.7 WR011

The lowest unit in core WR011 consists of a grey-black silty soil with some orange mottling around the base (Figure 13). It has an upper contact at 38.5 cm depth with a 4.5 cm thick gravel deposit that contains grey and rounded pebbles with *a* axes ranging (in size) from 4 to 30 mm. This layer is overlain by a 12.5 cm thick layer of black silty homogenous soil which in turn has a sharp upper contact at 21.5 cm depth with another gravel layer approximately 7.5 cm thick. This gravel layer contains rounded grey clasts, similar to the one below, with *a* axes ranging from 2 to 40 mm. The size of the pebbles in this unit shows a fining upwards trend. The uppermost unit in WR011 is a dark brown silty soil, starting at 14 cm depth and remaining relatively homogenous to the surface.

Mean grainsize data show marked increases associated with the two pebble layers (Figure 13). Sorting decreases at the top and base on each of the pebble layers with the middle of the units being better sorted. The organic content is inversely related to the grainsize data, being lowest within the pebble layers.

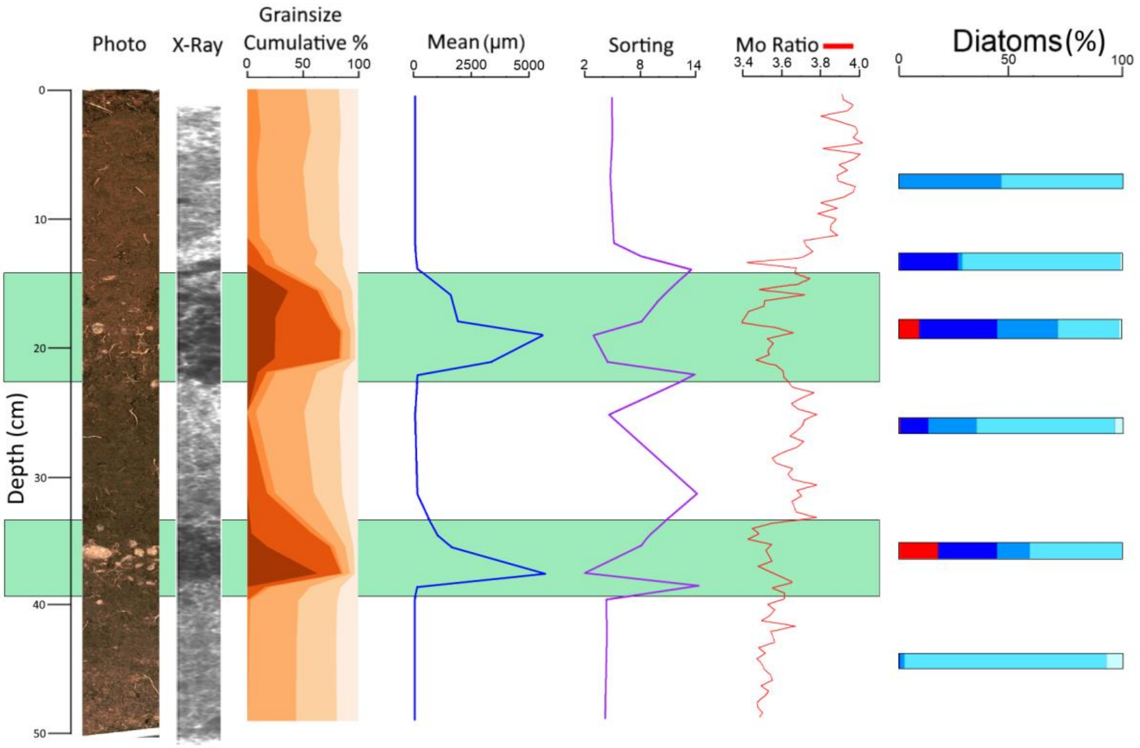

Figure 13: Stratigraphy of core WR011. From left to right: Photo, X-Ray, cumulative grainsize plot, mean grainsize (µm), sorting (Folk and Ward method), Mo-ratio (red line) and diatom species salinity preferences (%). Green shaded area shows location of anomalous layers. Refer to Figure 6 for the key to the cumulative grainsize plot.

4.2 Geochemistry

Elemental profiles exhibit spatial variations in all cores analysed, however, relationships between elements (normalised over KCPS) were not always consistent between cores. Nevertheless PCA allowed the groupings of elements and Mo-ratio, thereby assisting in the distinction of the anomalous (gravel) layers. While PCA often showed similar shapes and groupings, the plots also displayed variations in relationships amongst the cores.

4.2.1 WR005

Although the anomalous (gravel) layer cannot clearly be identified based on geochemical characteristics, its lower contact is marked by distinct changes in Mo-ratio, a decrease in Ca and Br counts and increases in Si, Fe, K and Ti (Figure 14). A large peak in Fe counts at 36-36.5 cm depth, caused by a piece of unidentifiable anthropogenic iron, is matched by marked negative counts in most elements and the Mo-ratio. This negative relationship is most probably an artefact of the analytical technique, the so called closed-sum effect (e.g. Van der Weijden, 2002). Therefore all elemental counts between 36 and 36.5 cm depth were removed before PCA was carried out.

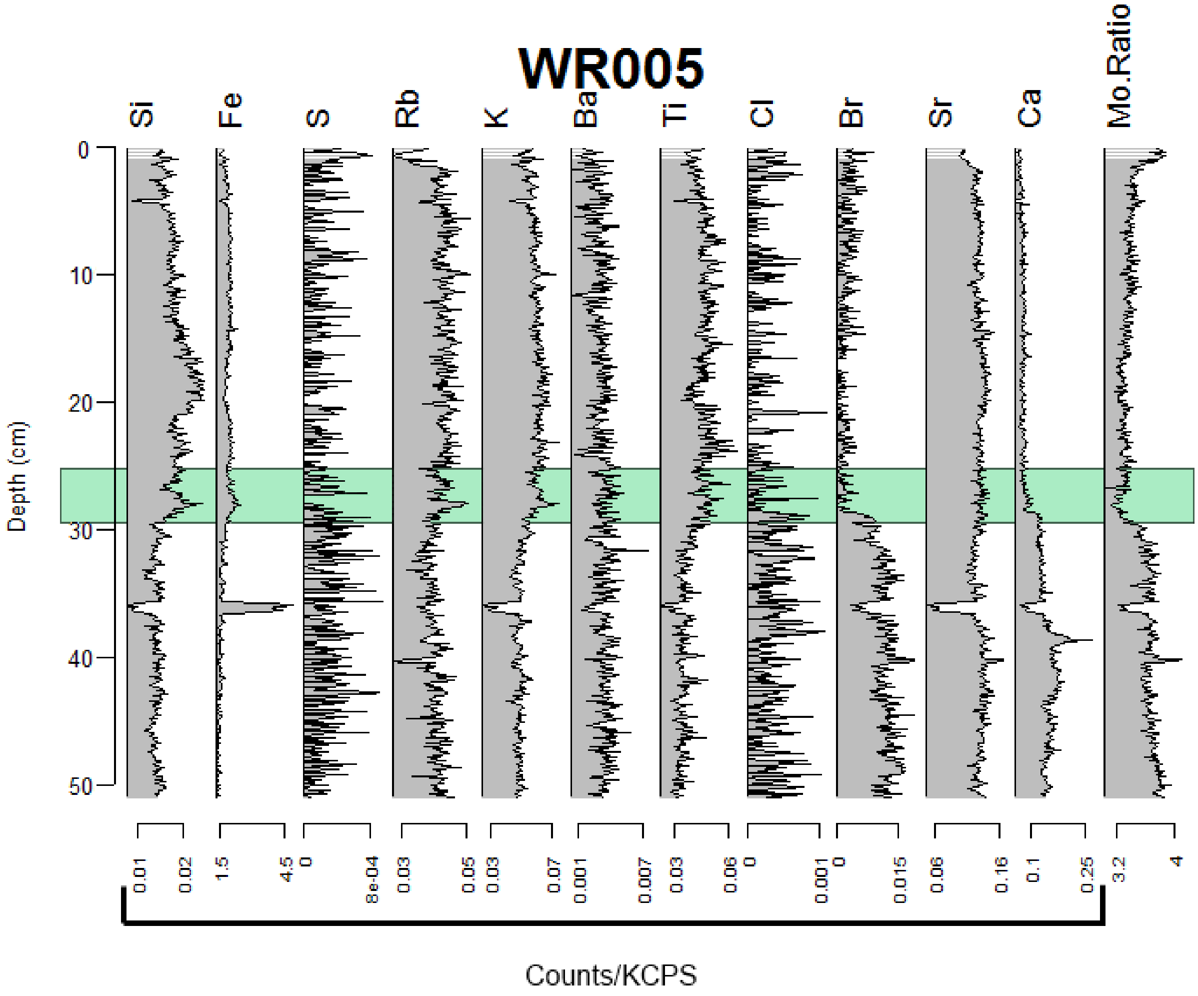

Figure 14: Normalised (expect for Mo-ratio) count data of selected elements from core WR005. The green shaded area shows the location of the gravel layer.

The amended PCA (PC1: 51.0% variance, PC2: 11.2% variance) shows a clumping of detrital elements (Ti, Rb, Si, Fe and K) to the right (Figure 15), Ca and Br are on the left side with organic content (Mo-ratio) on the far left, along the *x* axis. Ba and Sr are grouped together between the detrital and organic grouping, along the *y* axis. Cl and S group together and show a weak relationship with Mo-ratio. On the PCA plot the anomalous (gravel) layer is located between the detrital and the 'Ba-Sr' groups.

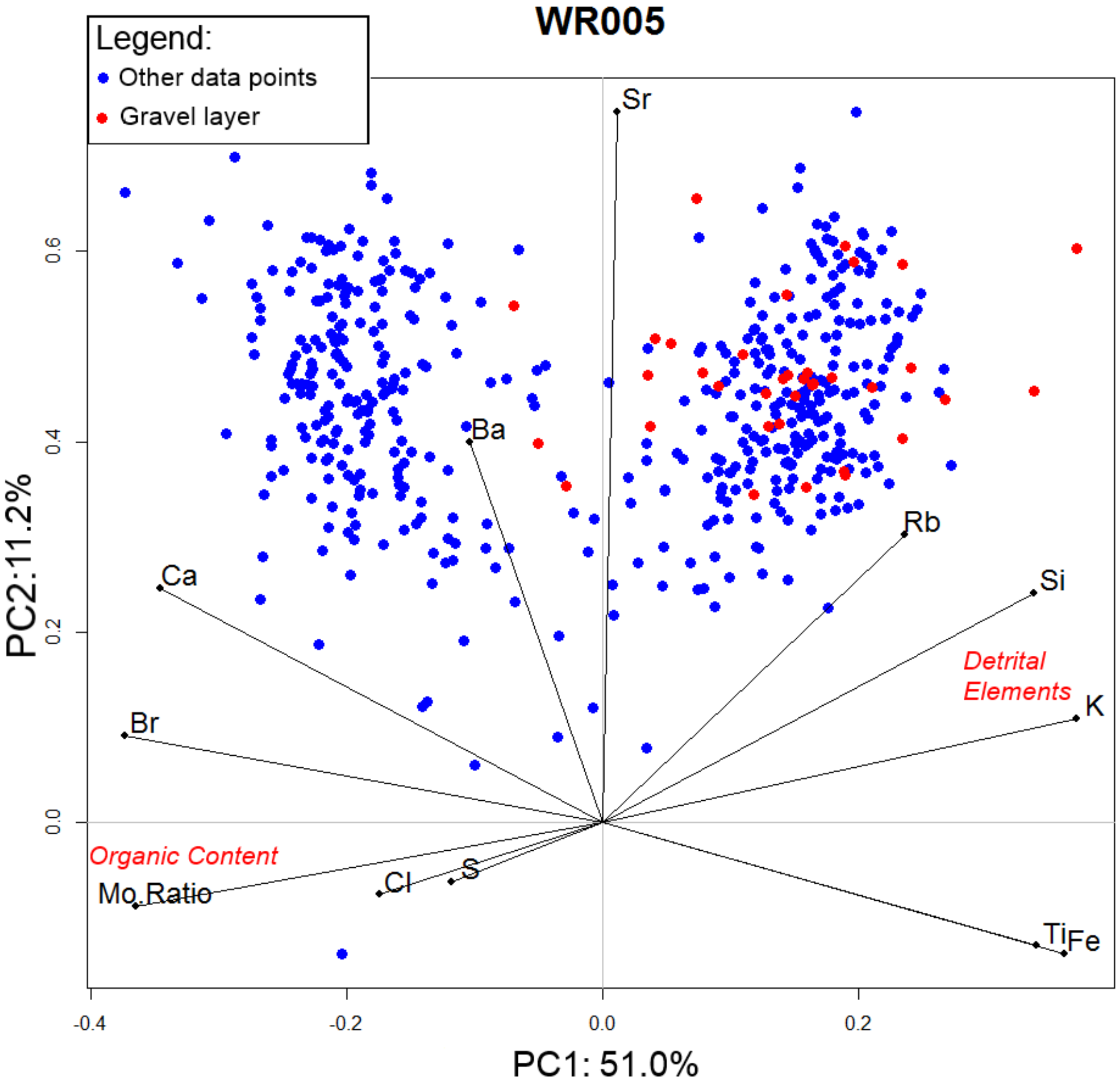

Figure 15: PCA plot of WR005 with the anomalous (gravel) layer (red) and the rest of the core (blue).

4.2.2 WR009

ITRAX data for core WR009 show an increase in Ba and S within the anomalous (gravel) deposit that coincides with a decrease in Br, Ca and Mo-ratio (Figure 16).

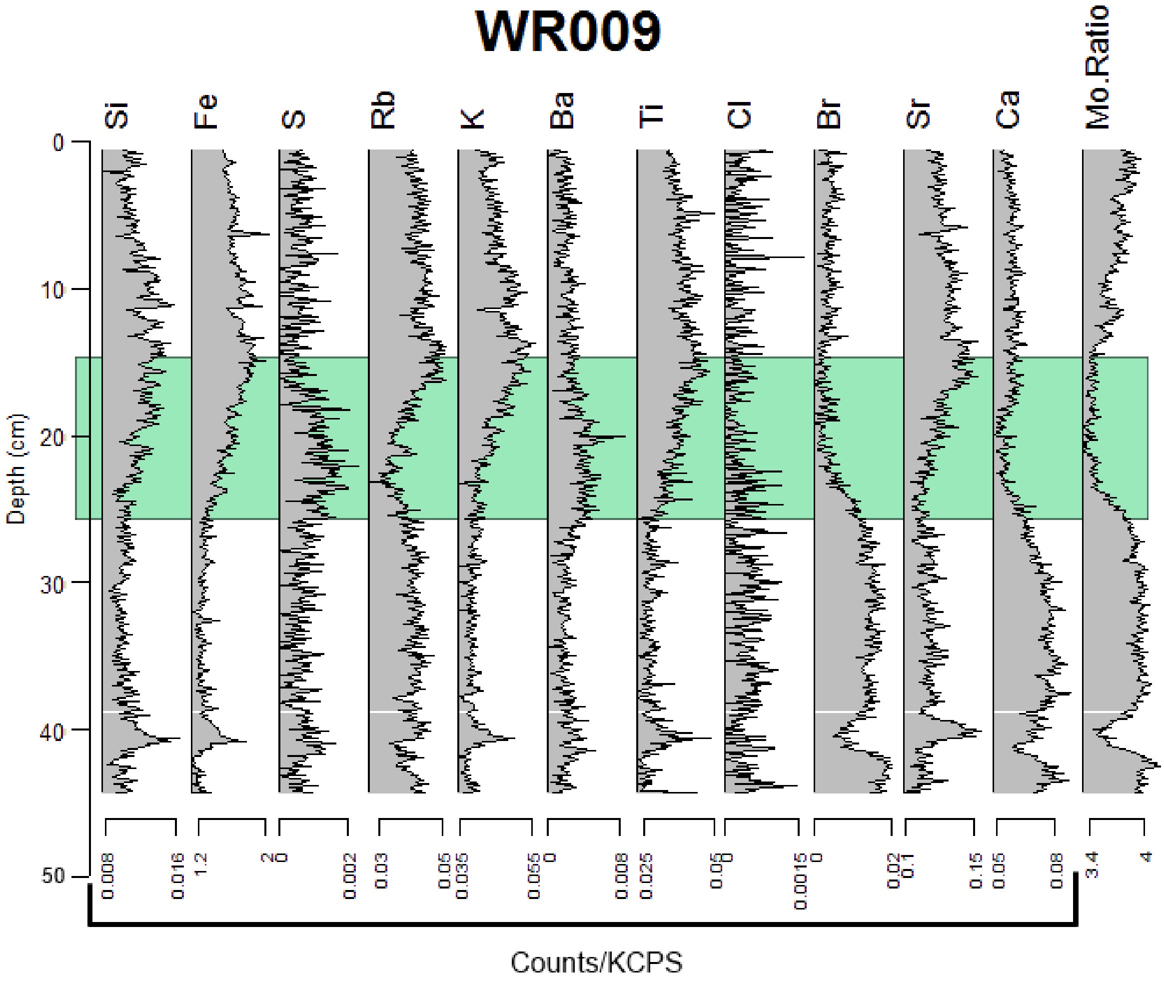

Figure16: Normalised (excluding Mo-ratio) count data for core WR009. Green shaded area represents the anomalous (gravel) layer with rare pebbles.

Four distinct groups can be distinguished from PCA in WR009. Along the *x* axis (51.6% variance) detrital elements (Si, Ti, Fe, K and Sr) displays a positive loading. On the opposite side of the plot, organic content (Mo-ratio) is clustered with Br and Ca with a weak relation with Cl. Along the *y* axis (19.4% variance) S and Ba are located at the top of the plot and Rb is by itself at the bottom (Figure 17). The sediments fall into three main ‘zones’ on the plot. Sediment above the deposit plot around the bottom right, showing an association with the detrital elements, reflecting the minerology of the brown silty soil. The chemistry of the sediments in the anomalous (gravel) layer shows an association between both detrital and the 'Ba-S' grouping. Below the deposit, in the organic rich soil, the chemistry correlates with organic matter (Mo-ratio), Ca and Br and to a lesser extent Cl.

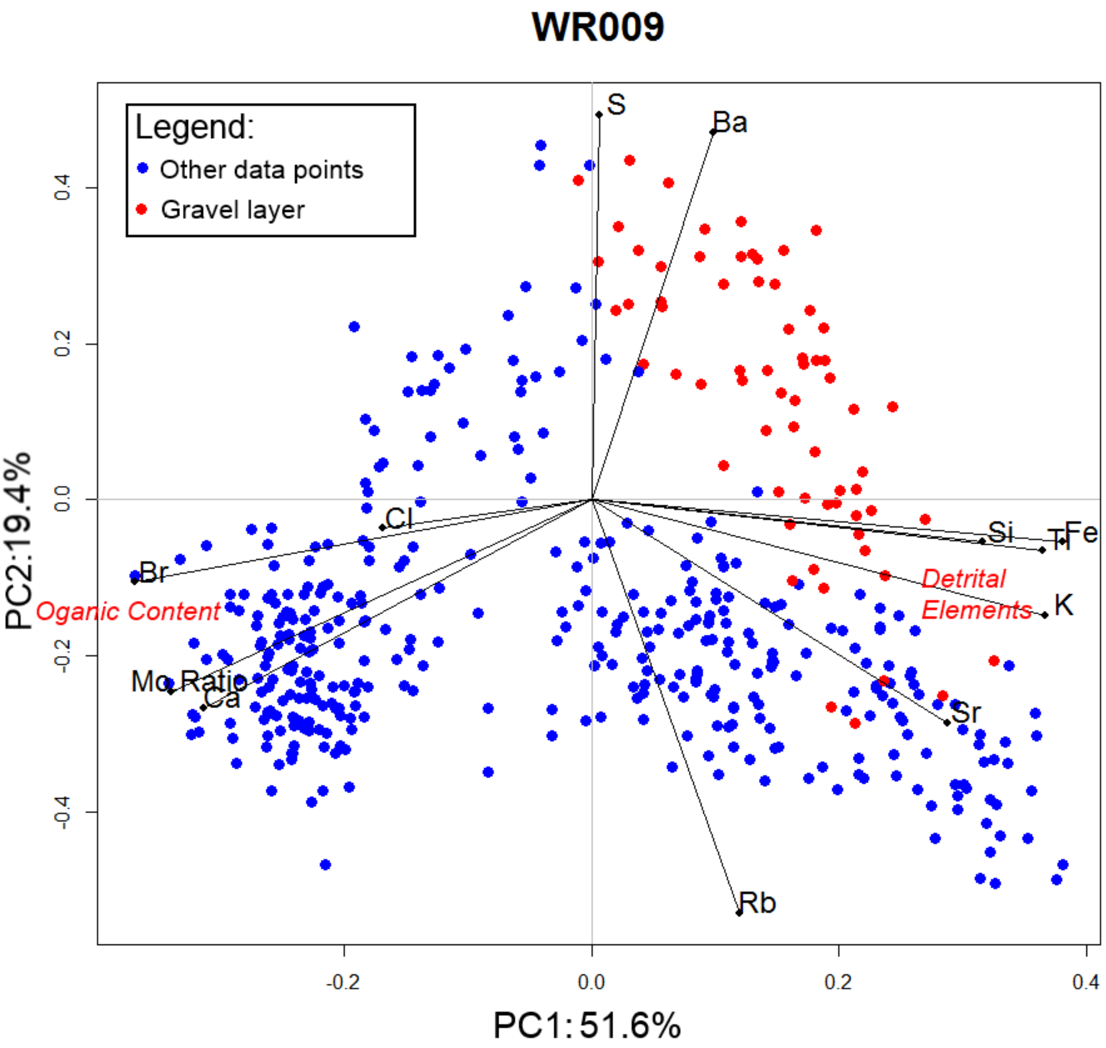

Figure 17: PCA plot of WR009 with the anomalous (gravel) layer in red and the rest of the core in blue. The plot also shows the four distinct grouping of elements (organic content-left, detrital elements-right, 'S-Ba' grouping-top, Rb-bottom).

4.2.3 WR011

ITRAX data for core WR011 display increases in Si, Sr, Rb, K and Fe deposit and a decrease in organic content (Mo-ratio) within the top anomalous (gravel) layer while there is little variation in elemental profiles between the lower anomalous (gravel) layer and the surrounding soil (Figure 18).

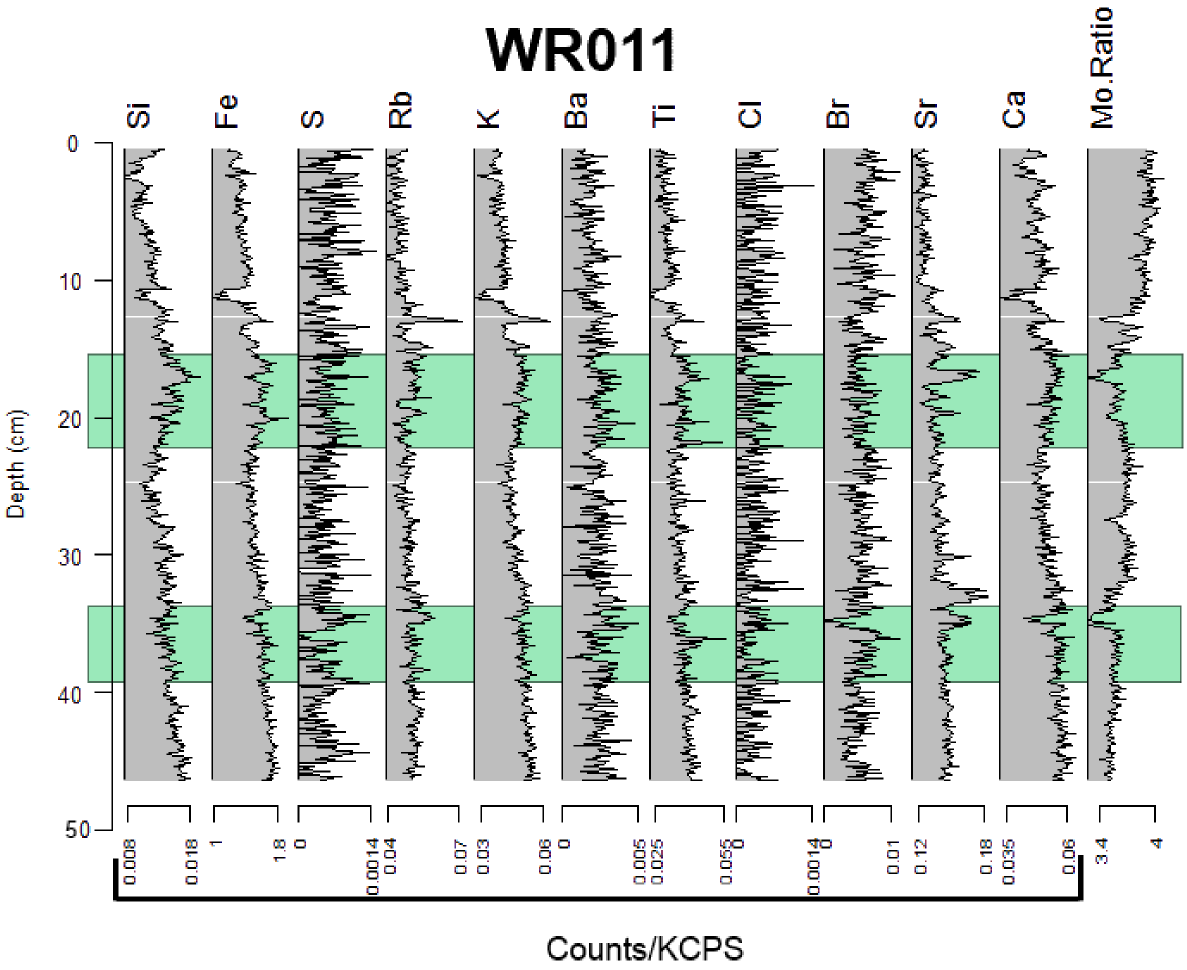

Figure 18: Normalised (excluding Mo-ratio) count data for core WR011. Green shaded areas represent the two anomalous (gravel) layers.

However PCA of WR011 (PC1: 50.7%, PC2: 11.2%) allows the grouping of elements into three distinct clusters, the detrital elements (Si, Sr, K, Fe, Ti, Rb, and Ca), the organic matter (Mo-Ratio) and a grouping of Cl and S (Figure 19). Elements Ba and Br are not associated with each other nor any other 'cluster', indicating that their presence in the stratigraphy is not correlated with any particular element. Along the *x* axis the detrital elements are clustered on the left side, inversely related to Mo-ratio on the far right. S and Cl are strongly related to one another, located on the *y* axis, between the detrital and organic regions of the plot. Both of the deposits in WR011 can be found between the detrital and 'S-Cl' region, associated with Ba.

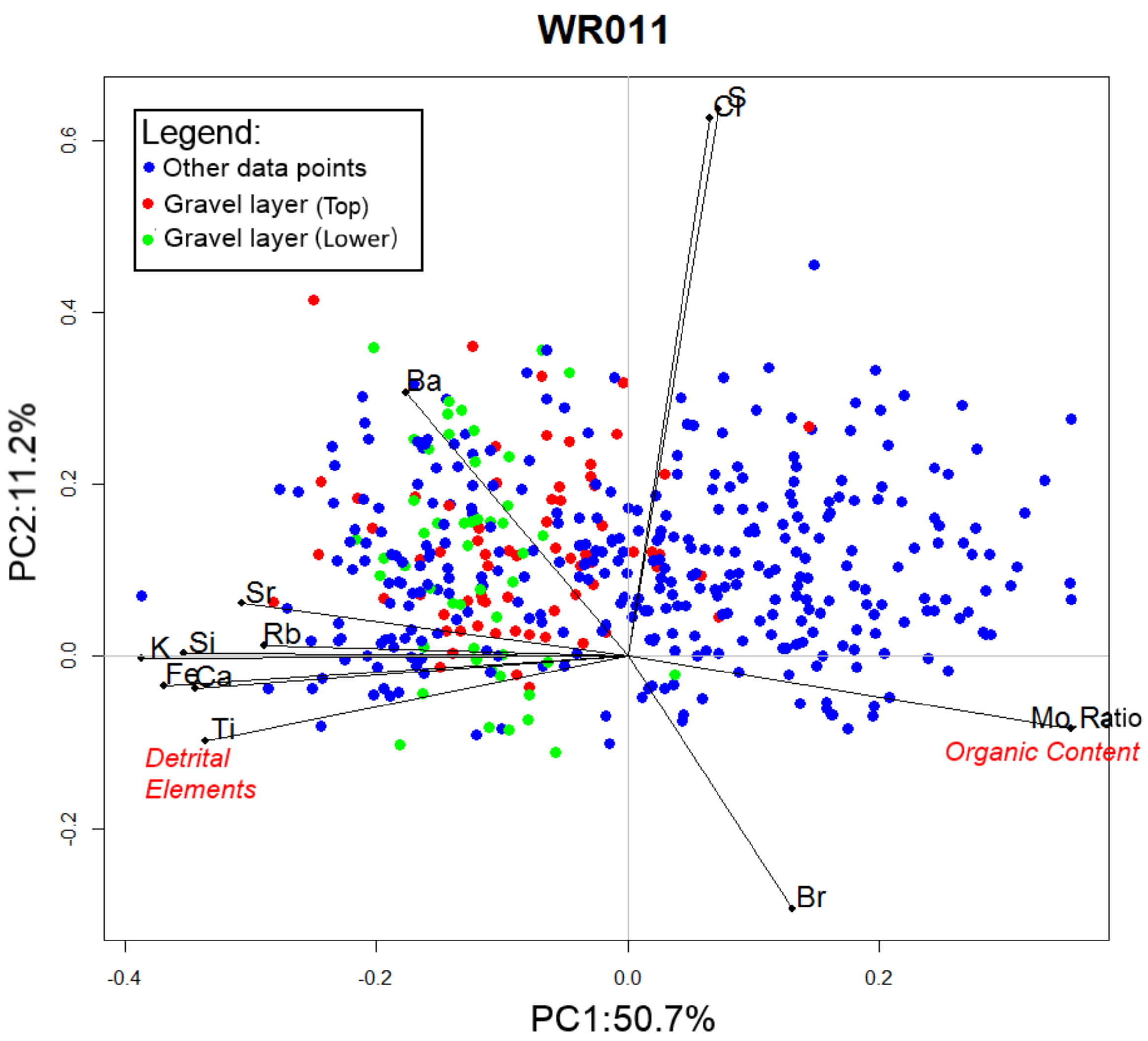

Figure19: PCA of WR011 displaying both anomalous (gravel) layers (red-top and green-lower) and the overlying and underlying soil (blue). Organic content is located on the right, detrital elements on the left and the 'Cl-S' grouping towards the top.

4.2.4 WR007, WR008 and WR010

ITRAX data for cores WR007, WR008 and WR010 show little variations between the anomalous (gravel) layer and the rest of the sequences (see Appendix C for plots of counts versus depth). PCA analysis however indicates a slight difference in the chemistry with the anomalous (gravel) deposit (Figure 20). PCA plots for WR007, WR008 and WR010 all show a similar shape: clumping of the detrital elements opposite the organic content, and groupings of elements, usually Cl, S, Br and Ba, located between the two groups, along the *y* axis. The deposits plot between the detrital and Cl and S in WR007 and between detrital and Br in

WR010 (Figure 20a, c). In both cores there is a tendency for the anomalous (gravel) layer to be associated with Ba. In WR008 the deposit plots between Ba and Mo-ratio, correlated with S, Cl and Ca (Figure 20b). In WR008 Br plots with organic content, implying that the Br in the deposit is associated mostly with organic matter, however in WR007 and WR010 Br plots away from the organic content suggesting an additional source for Br.

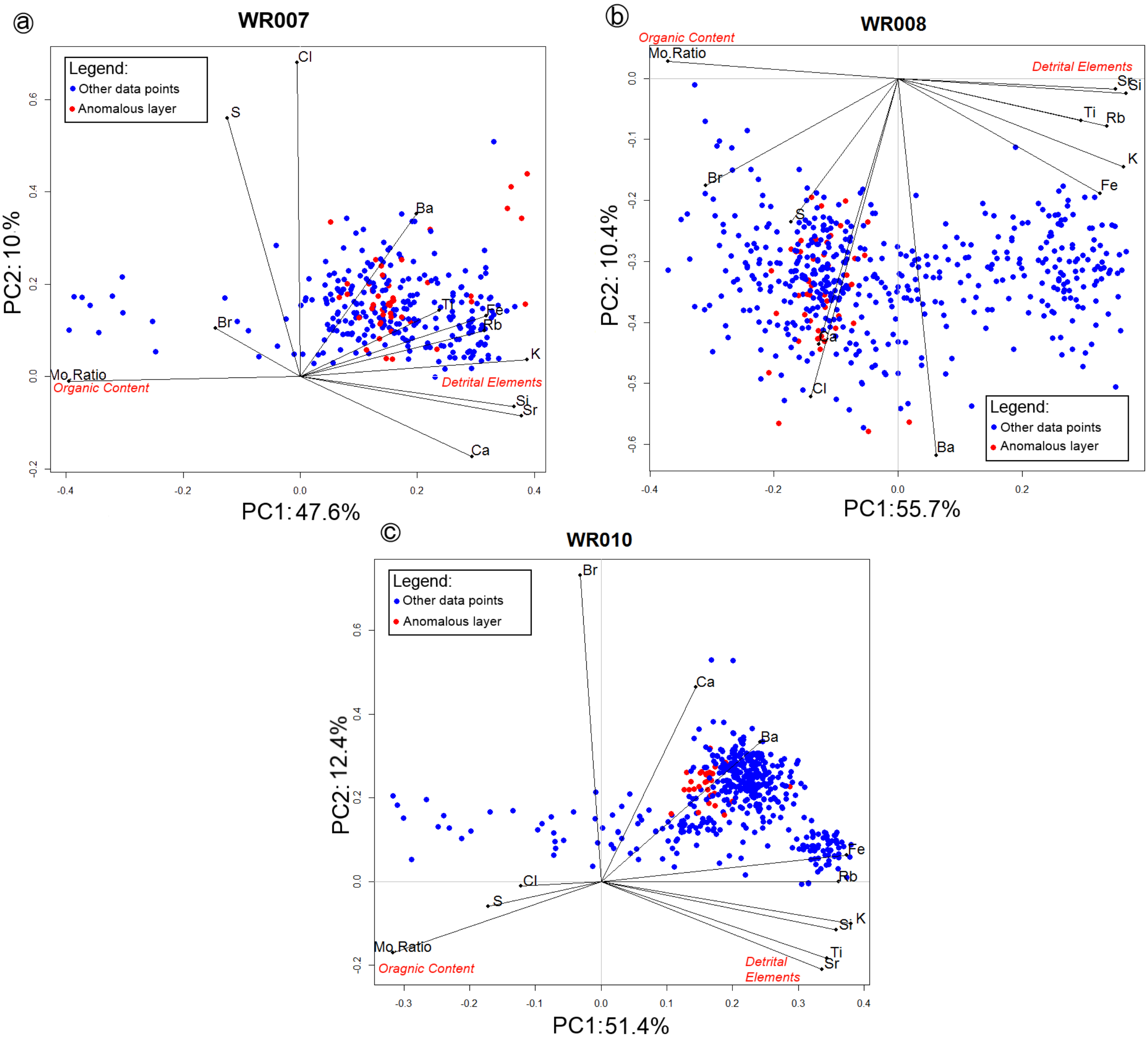

Figure 20: PCA plots for: a) WR007, b) WR008, c) WR010. Samples in the anomalous (gravel) units are in red, while the overlying and underlying sediments are in blue.

4.2.5 Grab Samples

Table 1 displays the Spearman's rank correlation coefficient between all the grab samples, calculated using geochemical count data. This suggests that WR004 (from the landslide face) and WR012T (from the lowest terrace on the opposite bank) are the most strongly correlated (correlation of 0.996), whereas WR001A (rock taken from the river bank) is the most chemically different from the rest of the samples.

Table 1: Spearman's rank correlation coefficients of the geochemical counts (after normalisation with KCPS) of the grab samples.

		Sample					
		WR001A	**WR001B**	**WR002**	**WR003**	**WR004**	**WR012T**
Sample	**WR001A**		0.886	0.906	0.904	0.911	0.909
	WR001B	0.886		0.962	0.968	0.973	0.962
	WR002	0.906	0.962		0.995	0.993	0.995
	WR003	0.904	0.968	0.995		0.992	0.992
	WR004	0.911	0.973	0.993	0.992		0.996
	WR012T	0.909	0.962	0.995	0.992	0.996	

4.2.6 Magnetic Susceptibility

Magnetic susceptibility showed no correlation with Fe or Ti when plotted in any of the cores (data not shown) suggesting that Fe and Ti were probably not present as ferromagnetic minerals. As the data therefore are unlikely to reflect heavy mineral deposition they will not be discussed.

4.3 Diatoms

Diatom slides were made from samples taken from cores WR005 and WR011 (Figure 5). Counts of 250+ diatoms were possible on 12 of the 14 slides. Full diatoms counts and species lists can be found in Appendix D.

4.3.1 WR005

Eight slides were made from subsamples of WR005 with only the uppermost sample, at 7 cm depth, containing no diatoms (Figure 6 and Table 2). The sample from 13 cm depth contained the highest amount of marine diatoms (50.4%) which were all in the form of the planktonic species *Paralia sulcata (Ehr.)* with 95% of the frustules being intact. The only other samples to contain any marine diatoms were located in and immediately above and below the gravel deposit. Samples from 25, 29 and 32 cm all contained some marine and marine-brackish species (22.7%, 30.2% and 11.6%, respectively). These samples also had the largest proportion of broken valves. The remaining samples, including one above the deposit at 22 cm and two below at 39 and 45 cm depth, were almost entirely composed of fresh-brackish or brackish-fresh (99.2%, 100% and 93.6%, respectively) diatoms. The majority of these species were either intact epiphytic or benthic in origin.

Table 2: Preservation, salinity preference and habitat preference of diatoms found in core WR005. Dark shaded columns represent samples from within the gravel layer or directly below it.

	Depth (cm)							
Diatoms:	**7-8**	**13-14**	**22-23**	**25-26**	**29-30**	**32-33**	**39-40**	**45-46**
Salinity Preference (%)								
Polyhalobous (Marine) (P)	0.0	50.4	0.0	8.4	12.1	4.8	0.0	0.0
Mesohalobous (Marine-Brackish) (M)	0.0	0.0	0.8	14.3	18.1	6.8	0.0	6.4
Oligohalobion halophilous (Brackish-Fresh) (OH)	0.0	0.0	35.4	13.5	24.5	6.0	1.9	13.9
Oligohalobion indifferent (Fresh-Brackish) (OI)	0.0	49.6	63.8	62.9	39.7	81.7	98.1	79.7
Halophobous (Fresh) (H)	0.0	0.0	0.0	0.8	5.7	0.8	0.0	0.0
Habitat Preference (%)								
Planktonic - tychoplanktonic (water column) (P)	0.0	54.7	4.7	11.6	20.3	5.6	0.0	0.0
Epiphytic (lives on plants e.g. seaweed) (E)	0.0	2.0	36.2	39.0	39.0	27.1	1.9	15.5
Benthic (seafloor/sediment) (B)	0.0	43.4	59.1	49.4	40.7	67.3	98.1	84.5
Percent Broken: Fresh (OH, OI, H)	0	75	22	75	90	35	5	10
Percent Broken: Marine (M, P)	0	5	100	75	50	50	0	0

4.3.2 WR011

Of the six samples taken from core WR011, five contained sufficient frustules while the topmost sample (7 cm depth) had only 81 diatoms counted (Figure 13 and Table 3). Samples from above or below the gravel layers (7, 14, 25 and 45 cm depth) contained mostly brackish-fresh to fresh-brackish diatom species with virtually no marine frustules (0.4% of total counts at 25 cm depth). They also contained few broken valves and much less planktonic species than those from within the gravel layers. Samples taken from the gravel layers (19-20 and 35-36 cm depth) contained a notable presence of marine diatoms (9.1% and 17.5%, respectively) and a high proportion of planktonic species. There were considerably more broken marine and non-marine species within the gravel layers than in any other sample.

Table 3: Preservation, salinity preference and habitat preference of diatoms reported in core WR011 (C denotes control). Dark shaded columns represent samples from the gravel layers.

	Depth (cm)						
Diatoms:	**7-8**	**14-15**	**19-20**	**25-26**	**35-36**	**45-46**	**C**
Salinity Preference (%)							
Polyhalobous (Marine) (P)	0.0	0.0	9.1	0.4	17.5	0.0	0.0
Mesohalobous (Marine-Brackish) (M)	0.0	26.3	35.0	12.7	26.3	0.4	0.0
Oligohalobion halophilous (Brackish-Fresh) (OH)	45.7	2.0	27.2	21.5	14.7	2.0	0.0
Oligohalobion indifferent (Fresh-Brackish) (OI)	54.3	70.9	27.6	61.8	41.4	90.4	0.0
Halophobous (Fresh) (H)	0.0	0.8	1.2	3.6	0.0	7.2	0.0
Habitat Preference (%)							
Planktonic - tychoplanktonic (water column) (P)	2.5	35.5	50.4	5.8	47.8	15.1	0.0
Epiphytic (lives on plants e.g. seaweed) (E)	71.6	49.0	41.3	42.9	33.1	45.8	0.0
Percent Broken: Fresh (OH, OI, H)	0	5	25	20	35	5	0
Percent Broken: Marine (M, P)	0	0	25	5	50	0	0

4.4 Dating

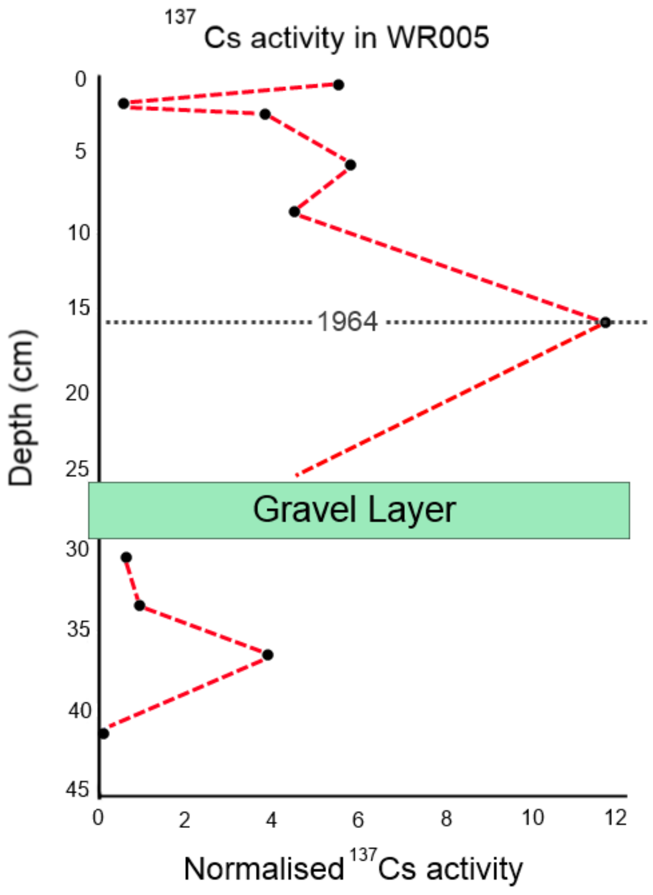

Figure 21: Normalised ^{137}Cs activity plotted against depth in core WR005. The green shaded area represents the position of the anomalous (gravel) layer.

Unsupported ^{210}Pb activity was low in core WR005, possibly due to the environmental conditions not being conducive to retention of unsupported ^{210}Pb (Kirchner, 2011). As a result, these data were not suitable for obtaining any chronology. ^{137}Cs activity in the core, while being low (2.7 Bq/kg maximum: Appendix E), could be used after being normalised for grainsize (Figure 21). Normalisation by the <63µm fraction was done to account for the strong association of ^{137}Cs with fine particles, particularly clays (Kirchner and Ehlers, 1997). The ^{137}Cs plot shows a peak at 16 cm depth, which probably represents the peak in 1964 (in the southern hemisphere) usually reported in sedimentary sequences (Pennington et al., 1973; Matthews, 1989).

4.5 Gravel Deposit

In total, 52 GPS points (Appendix F) were taken throughout the site encompassing the extent of the gravel layer (Figure 22). The maximum landward extent of the gravel layer was found directly opposite the landslide site. Its extent follows the topography of the slope before dropping down closer to the river bank. It can then be traced parallel to the river bank for ~150 m before running out towards the south east of the study area (Figure 22).

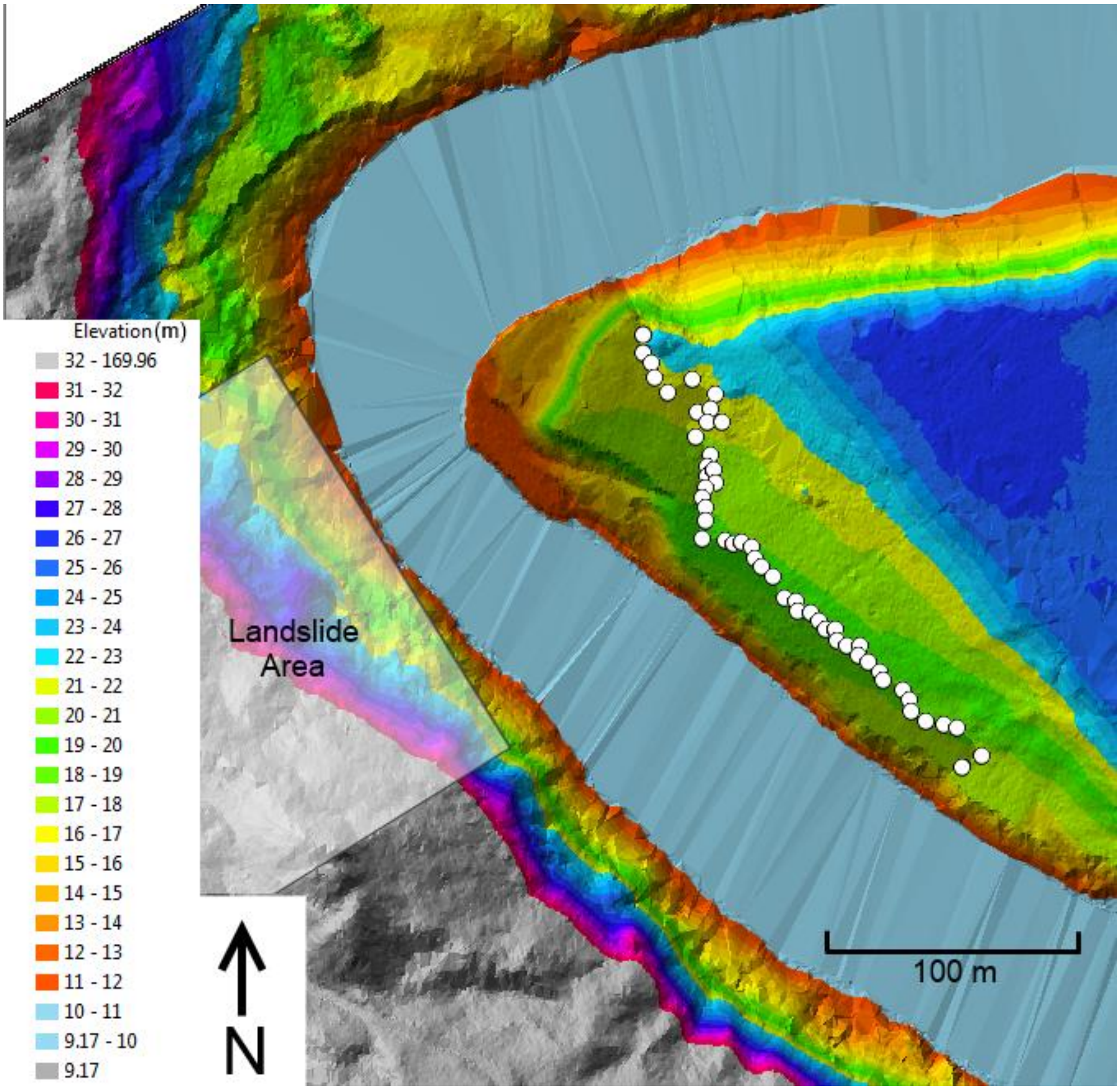

Figure 22: GPS points (white circles) representing the extent of the gravel deposit throughout the site. White shaded area on the western bank of the river shows the lower portion of landslide scar.

4.6 Landslide

The size of the landslide was calculated as approximately 1,705,000 ± 170,500 m^3. This error value was determined by calculating volume differences from both sides of the three surrounding hills (Figure 23). Results of these volumetric calculations are shown in Table 4, along with the percentage differences between each slope. There is an average slope volume difference of 8.6% (Table 4) and as such an error ±10% was deemed appropriate. While this is a relatively large error, even at the lower end of the estimated slide the magnitude of any resultant tsunami will be limited by the amount of water in the river.

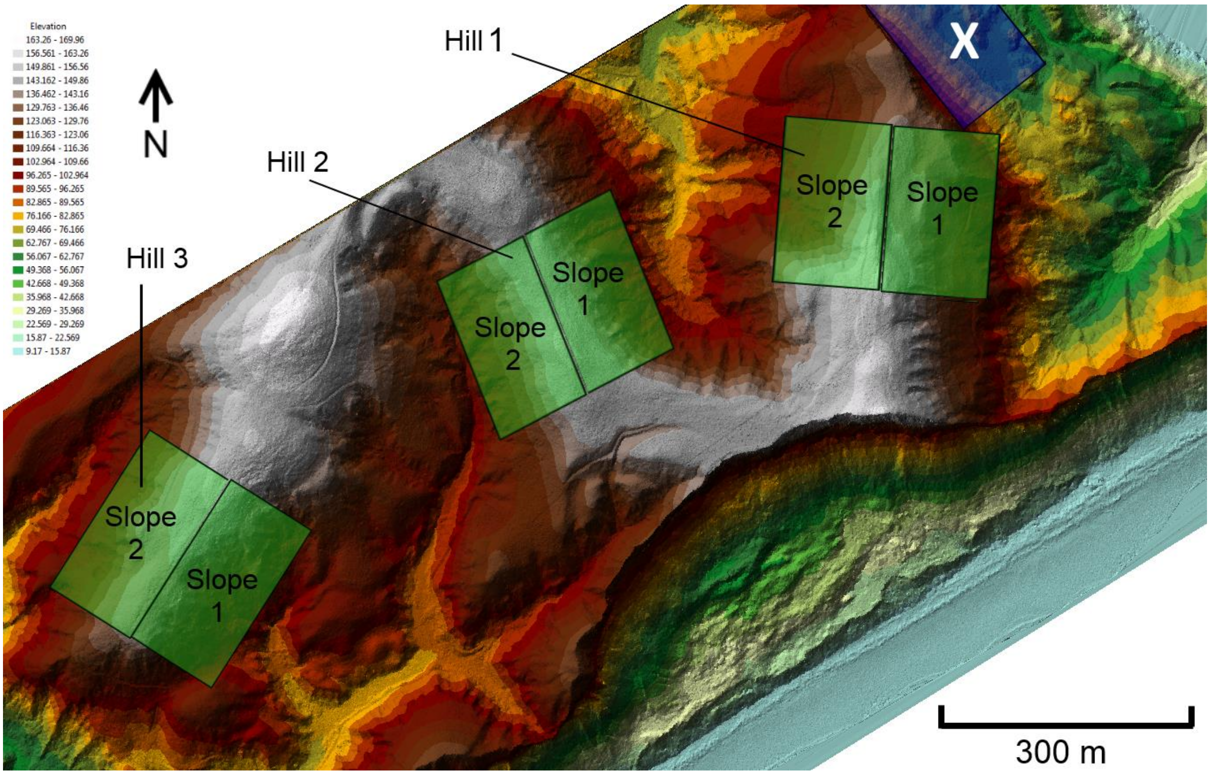

Figure 23: Three hills used in calculating an appropriate error for landslide size. 'X' (in the NE corner of the figure) corresponds to the location of the 1931 landslide, with the study area immediately to the north east of the figure.

Table 4: Volumes of opposite slopes from three unfailed hills surrounding the landslide area. (Note: the volumes are in decimal degrees, the dataset's native coordinate system)

	Volume (Decimal Degrees)		
	Hill 1	**Hill 2**	**Hill 3**
Slope 1	0.00013041	4.2707E-05	1.6778E-05
Slope 2	0.00014708	4.6086E-05	1.8065E-05
Difference (%) between slopes	11.3364033	7.33085893	7.12678558
Average slope volume difference: 8.6%			

5.0 Discussion

The 1931 Hawke's Bay Earthquake produced widespread ground shaking throughout the Hawke's Bay region, triggering faulting, uplift, subsidence and landslides. This region-wide deformation led to 30 cm of uplift at the mouth of the Waikari River (Hull, 1990). Simultaneously, shaking caused the failure of a 120 m high loess hill located 700 m upstream from the mouth of the river, opposite the homestead of Waikari Station (Tait, 1977).

The landslide, with a calculated volume of 1,705,000 m^3 ± 10%, spilled into the river, displacing the water and resulting in a large wave that inundated the Waikari Station. Field observations and descriptions from 1931 point to the type of landslide being a rotational debris slide, as defined by Hungr et al. 2014. A rotational debris slide is a mass of predominately coarse particles failing along a concave up plane of weakness (e.g. Crozier, 1986). The size and mechanism of the 1931 event meant that it would have been more than enough to transport river water and sediments onto the opposite bank and dam the channel as reported at the time. "The river was completely blocked by this huge earth outfall" (Tait, 1977). Geochemical analysis supports this, showing a very high correlation in the chemistry between grab samples taken from the landslide face and the lowest terrace on the opposite bank, suggesting that the toe of the landslide extended across the river.

Tait, who spent much of his life on Waikari Station and was at the station the day after the event, goes on to describe the aftermath of the landslide, describing the resulting wave in his memoir: "It also lifted the waters of the river onto the top terrace, surrounding the homestead and washing some of the outbuildings a chain or so away" (Tait, 1977). The energy of this wave was also such that it destroyed the entire sheep shed, as well as knocking over a tangye engine (a large multipurpose combustion engine), estimated to weigh between one and two tonnes (Tait, 1977).

A possible contributing factor to the landslide was land clearing by Maori and then more invasively by European settlers. Maori cleared flora mainly with the use of fire, changing the vegetation of the region from podocarp/hardwood forest to one dominated by more shallow rooted bracken fern-scrubland (Wilmshurt, 1997a). This was followed by European settlement of the region and the subsequent clearing of much of the remaining forest and the scrubland to create pasture for grazing in the 1870s (Wilmshurt, 1997b). These changes would have led to lower slope stability making hills more prone to failure.

During fieldwork aimed at identifying and analysing the deposit left by the event, a gravel layer was found adjacent to the river bank which thinned inland.

5.1 Dating

Dating performed on core WR005 found insufficient unsupported ^{210}Pb to obtain a chronology, however ^{137}Cs activity, which was measured simultaneously, after normalisation for grainsize displayed a peak at around 16 cm depth. This most likely constitutes the 1964 peak. Thus, at that site, the average sedimentation rate is 0.3 cm y^{-1} between 1964 and 2015. Extrapolating a chronology based upon this sediment accumulation rate, assuming that it is constant, places 1931 at a depth of 25.7 cm which matches well with the top of the gravel deposit found at 25 cm.

There is evidence of some minor remobilisation of ^{137}Cs down the core as illustrated by the presence of ^{137}Cs activity below the 1931 deposit. This is most likely due to migration of ^{137}Cs through the core which can occur in a variety of ways including: bioturbation, physical mixing or downward molecular diffusion (Klaminder et al., 2012). Downward diffusion of ^{137}Cs is not uncommon and has been reported in a number of studies (e.g Robbins and Edington, 1975; Davis et al., 1984; Anderson et al., 1987) but does not negate the recognition of concentrations associated with the 1964 peak (Krishnaswamy et al., 1971).

While radionuclide dating is not conclusive in this instance it is supported by the discovery of debris within the deposit. Two roofing nails, in addition to a piece of broken crockery were found in WR009. These items of debris are most likely from the damaged sheep shed and homestead. The destruction and distribution of debris throughout the site was reported in Tait's 1977 memoirs "[t]he debris of these buildings was strewn along the beach…". So it is not unlikely that some were incorporated into the deposit at WR009 which is between the homestead and the beach.

These two lines of evidence, along with the historical accounts, therefore strongly suggest that the gravel deposit found on the Waikari Station site resulted from the 1931 event.

5.2 Stratigraphy

Sediments lain down by the 1931 Waikari River Tsunami consist of a distinct gravel layer which generally thins inland, also showing a decrease in the grainsize away from the river. The gravel layer present in cores WR005, WR009 and WR011 consists of clasts with *a* axes ranging from 5 mm to 25 cm. The clasts are elongated, rounded and grey, appearing to have a similar size distribution, colour and shape to the gravels lining the river bed. The gravel layers are also organic-poor compared to the surrounding soil.

The thickness of the gravel layer increases from WR005 to WR009 (Figure 24), which might be contrary to the generally expected observation that tsunami deposits thin as they travel inland losing energy (Goff et al., 2012), although there have been reports of localised variations in deposit thickness due to topography and tsunami flow regimes (Richmond et al., 2012). The increase in thickness from WR005 to WR009 therefore could be due to WR005 being located on the side of a cutting, whereas WR009 is on flat land and therefore it is possible that a greater amount of gravel was deposited in addition to WR009 being less susceptible to erosion during the tsunami return flow. There is evidence of the deposit thinning, however, between sites WR009 and WR010 (Figure 24). Sharp basal contacts, a feature of tsunami deposits (Chagué-Goff et al., 2011), were present in WR011 along with an indication of infilling of microtopography at sites WR005, WR006 and WR011.

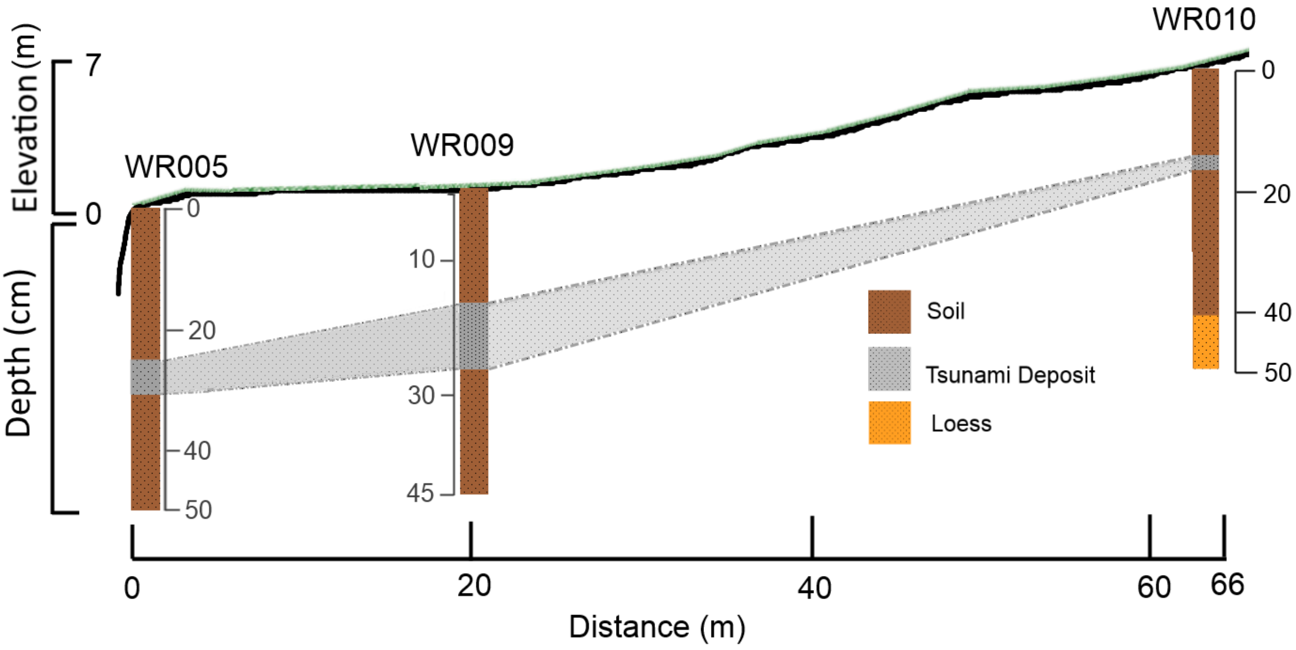

Figure 24: Location and thickness of the inferred tsunami deposit in cores WR005, WR009 and WR010.

WR007 and WR008 contain no obvious gravel layer this finding agrees with the mapped extent of the gravel deposited throughout the site (Figure 22). There is an increase in grainsize at both sites, however it is less then would be expected, especially when compared to the nearby site WR011. Historic documents describing the destruction of the sheep shed, which is located between sites WR007 and WR008, suggest a large amount of water passed through both sites and as such a more recognisable deposit would be expected. The absence of more coarse sediments here can be explained in terms of the availability of source materials. The bed of the Waikari River, the main source of the tsunami sediments, consists only of coarse gravels with finer sediments (*a* axis <5 mm) transported downstream. This dominantly coarse grainsize distribution caused most of the tsunami deposit to be laid down adjacent to the river with little or no fine sediment tail extending inland.

There is little evidence of sediments fining upwards within the deposits, as often reported in tsunami deposits (Morton et al., 2007). This is also due to relative lack of variation in the size distribution of the source sediments. However there is some evidence of fining upwards in the deposit in WR008.

5.3 Geochemistry

The geochemical signal of the cores was subtle at sites which had the most material deposited (WR005, WR009 and WR011), and undetectable without the use of PCA in the other sites (WR007, WR008 and WR010).

Geochemistry can provide information that can be useful in identifying deposits left behind by events such as tsunamis (Chagué-Goff, 2010). Marine indicators (e.g S, Cl and Br) might be elevated in sediments deposited by a tsunami. The geological signature can also help identify the source material (Chagué-Goff et al., 2015). However in this study this proved challenging.

Detecting a marine signature is difficult for a number of reasons, firstly the river itself was brackish, not fully marine, resulting in a weaker signal to that of a full marine inundation. The lack of water ponding, due to the sloping geomorphology of the site, also resulted in a more subtle signal. Water allowed to sit and evaporate leaves behind the elements in higher concentrations, creating more defined signatures compared to when the water can easily run off, as observed after recent tsunamis (e.g. Chagué-Goff et al., 2012)

In this case the local geology is dominated by marine Plio-Pleistocene sediments. Consequently potential brackish signals might also be similar to those of the authigenic sediments.

Assessing the presence of chemically different source material was difficult due to the similarity of the deposited sediments to the surrounding material. The source of the river is the Maungaharuru ranges which consist of greywacke-argillites and marine Plio-Pleistocene sediments. These sediments are mostly the source of both the deposited and the surrounding material making it difficult to observe differences in the chemistry between these two sediments.

Due to the factors mentioned above, the geochemical data were analysed with PCA. PCA allows much subtler differences to be examined and trends to become apparent (e.g. Xue et al., 2011).

PCA plot of WR009 showed the clearest difference between the deposit chemistry and the surrounding sediments (Figure 17). The gravel layer plots in the top right corner of the PCA, away from the surrounding sediments, between the grouping of Ba and S and the cluster of detrital elements. The variation in chemistry throughout the gravel layer suggests that the deposition process and components of the gravel differ from the rest of the core. It is assumed that this is a result of the tsunami.

While PCA of the remaining sites are not as well defined as WR009 they all show the same general shape: elements associated with detrital inputs (e.g. K, Si, Fe and Rb) grouping together, with organic content plotting on the opposite side. All cores also contained elements, or groupings of elements, associated with neither detrital inputs nor organic content and are termed the ‘third grouping’. Elements in this ‘third grouping’ varied between cores however it was always some combination of Ba, Cl and S. If sediments were of a similar source this pattern would not be expected, the relationship between elements would remain similar the entire length of the core, causing all elements to plot together (e.g. Pereira et al., 2003).

Highlighting samples associated with the anomalous/gravel layer on the PCA plots assisted in determining which elements, or groups of elements, are most strongly associated with the deposit. The anomalous/gravel layer tends to plot between the ‘third grouping’ and the detrital elements. The ‘third grouping’ is not associated with detrital inputs nor organic matter therefore is likely to originate from another source.

The location of Ba in the PCAs is of particular interest as it usually plots close to the anomalous/gravel layer. Dissolved Ba is invariably higher in estuary environments then in a full marine or freshwater setting (Coffey et al., 1997). In low salinity environments Ba undergoes desorption, leading to an increase in the concentration within the mixing zone of estuaries. As salinity increases Ba precipitates with sulphate in the seawater resulting in a decrease in concentration in a marine setting (Coffey et al*.,* 1997). Because of this Ba could be an indicator for inundation from a brackish source. Therefore the tendency for the gravel/anomalous layer to associate with Ba on a PCA suggests these sediments were indeed deposited by the 1931 tsunami.

5.4 Diatoms

Diatom analysis of cores closest to the river (WR005 and WR011) displayed assemblages commonly associated with marine/brackish inundation. In both WR005 and WR011 species of marine diatoms were found in the gravel deposit, while samples from outside the gravel layers contained only fresh water species. The exception to this was at 13 cm depth in core WR005 which showed the highest percentage of marine diatoms despite being above the deposit range. This likely reflects contamination of the sample. Contamination is unlikely to have occurred during sample preparation as a blank control was prepared and no mixing between samples was noted. It is therefore most likely that contamination occurred *in situ* as a result of human activity. Site WR005 is adjacent to a pathway so there is potential for human activity resulting in contamination.

Both fresh and marine diatoms within the gravel deposits had a significantly higher instance of broken frustules compared to the rest of the core. This suggests deposition by turbulent flows wherein the valves are damaged due to high energy currents often containing debris (Hemphill-Haley, 1996; Dawson, 2002). The habitat preference of the diatoms also suggests that they were deposited by a tsunami. Dura *et al*. (2016) report higher instances of planktonic (found in the water column) or benthic (found in sediments) species in tsunami deposits. This agrees with the assemblage that was found within the gravel layers of WR005 and WR011 which both contained higher counts of planktonic species.

5.5 Precursor of the 1931 Tsunami

Two gravel layers were identified at site WR011. Both gravel layers, the upper (14-21.5 cm depth) and the lower (34-39 cm depth), contain evidence of deposition by a tsunami. Sedimentological indicators, such as the grainsize and sorting suggest similar source material. The diatom taxa found and the high portion of damaged frustules also imply both gravel layers were deposited by high energy events. PCA plots of the geochemical data also support this as both deposits plot in similar locations. The top gravel deposit is believed to be a result of the 1931 event as there is no report of any other tsunamis or events which could have deposited a gravel layer since 1931.

Similarities between the lower deposit and the 1931 event above, suggest that it was probably caused by a similar mechanism, i.e. a landslide into the Waikari River. Since there is no evidence of the lower deposit in any of the other cores it appears that this may have only been a relatively small event associated with a minor landslide from the opposite bank of the river. However attempts to observe a landslide scar in the field and with LiDAR data were unsuccessful.

One potential cause for this earlier, small landslide could have been the 1863 Hawke's Bay Earthquake. This M_L 7.5 earthquake had a focal depth of 25 km and was located 100 km south of the mouth of the Waikari River (Figure 1a) (Stirling et al., 1998). At that site sedimentation rates between the surface and the top of the 1931 deposit (14 cm) are 0.17 cm y^{-1}, assuming a constant rate and limited erosion, the top of the lower deposit (34 cm depth) would have been deposited around 1855. This timing fits with the 1863 Hawke's Bay Earthquake however without further detailed research it is impossible to know the precise generating mechanism and timing of this event.

5.6 Possibility of Future Events in the Region

Taking into account the 1931 tsunami and evidence of a probable earlier event at the same site suggests that these events may occur relatively frequently in the Hawke's Bay region and therefore there is a high probability that more will occur in the future.

Future events, exacerbated by land clearing, have the potential to have a large impact on the region, posing a threat to infrastructure, stock and human life. While there exist highly localised risks from both a landslide and possible tsunami, a landslide alone could also lead to the damming of rivers. Damming occurred in both the Waikari and a tributary of the Mohaka Rivers following the 1931 Hawke's Bay Earthquake (Adams, 1981). While the blockage of the Waikari River was manually removed two days after the event, the Mohaka tributary was dammed for seven years, resulting in a 2 km long 25 m deep, temporary lake (Adams, 1981). The risk of landslides damming a river upstream poses a serious threat as a subsequent breach can cause downstream flooding in towns located around the mouth of a river, e.g. Wairoa.

A brief survey of the area around the Waikari River illustrates two potential risks in the region (Figure 25).

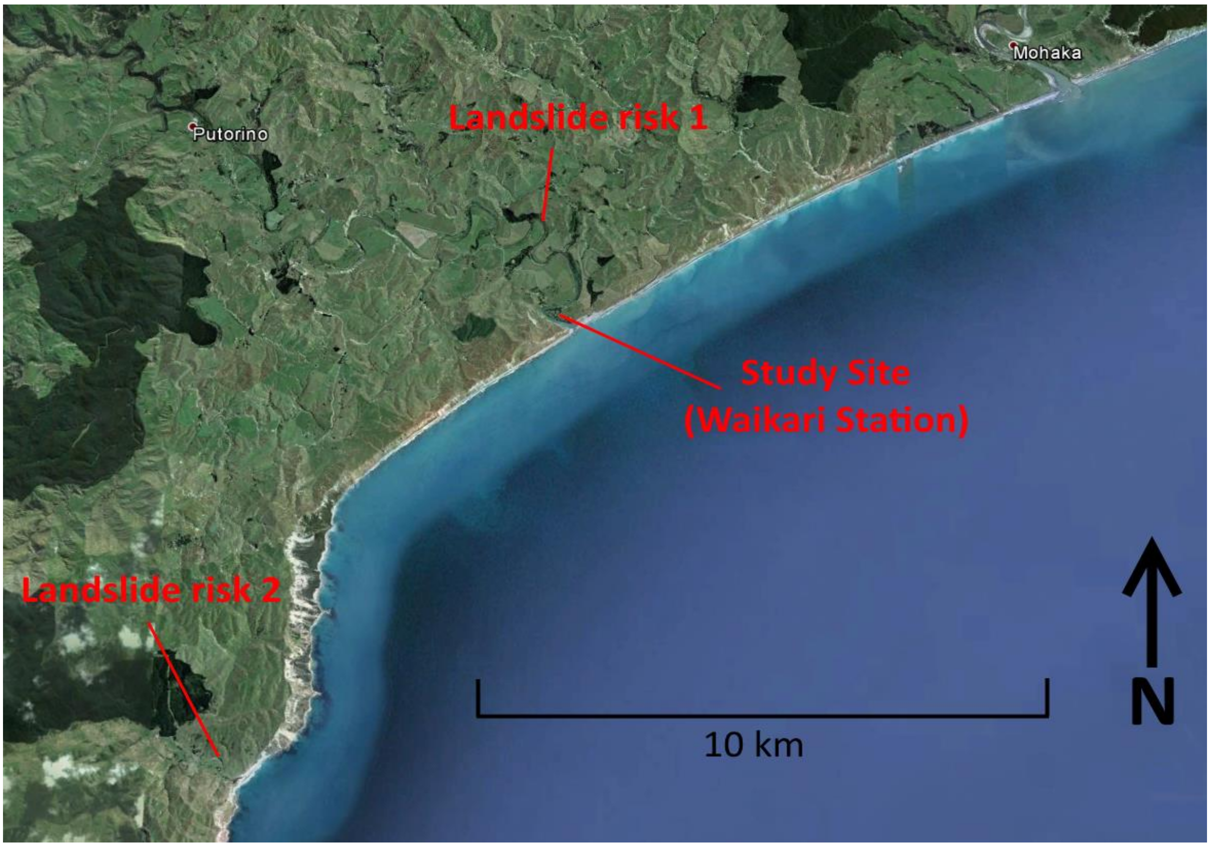

Figure 25: Map showing the locations of two areas at risk from landslides and landslide induced tsunamis (Google Earth).

5.6.1 Site 1

The first site identified as being at risk of a landslide-induced tsunami is also on the Waikari River, approximately 3.3 km upstream from the main study site (Figure 25). The hazard at this site originates from a 140 m high oversteepened hillslope which displays evidence of landslide scaring, this would be most likely point for the hill to fail (Figure 26, D). There is a building 20 m from the opposing bank, approximately 1 m higher than the river level which could be at risk (Figure 26, E). However it is approximately 100 m between the likely failure point and the building (Figure 26). If the hill were to fail it is likely the mass of debris would be enough to displace all the water, potentially damming the river. A detailed survey is required to accurately predict how this would affect the entire site and downstream land.

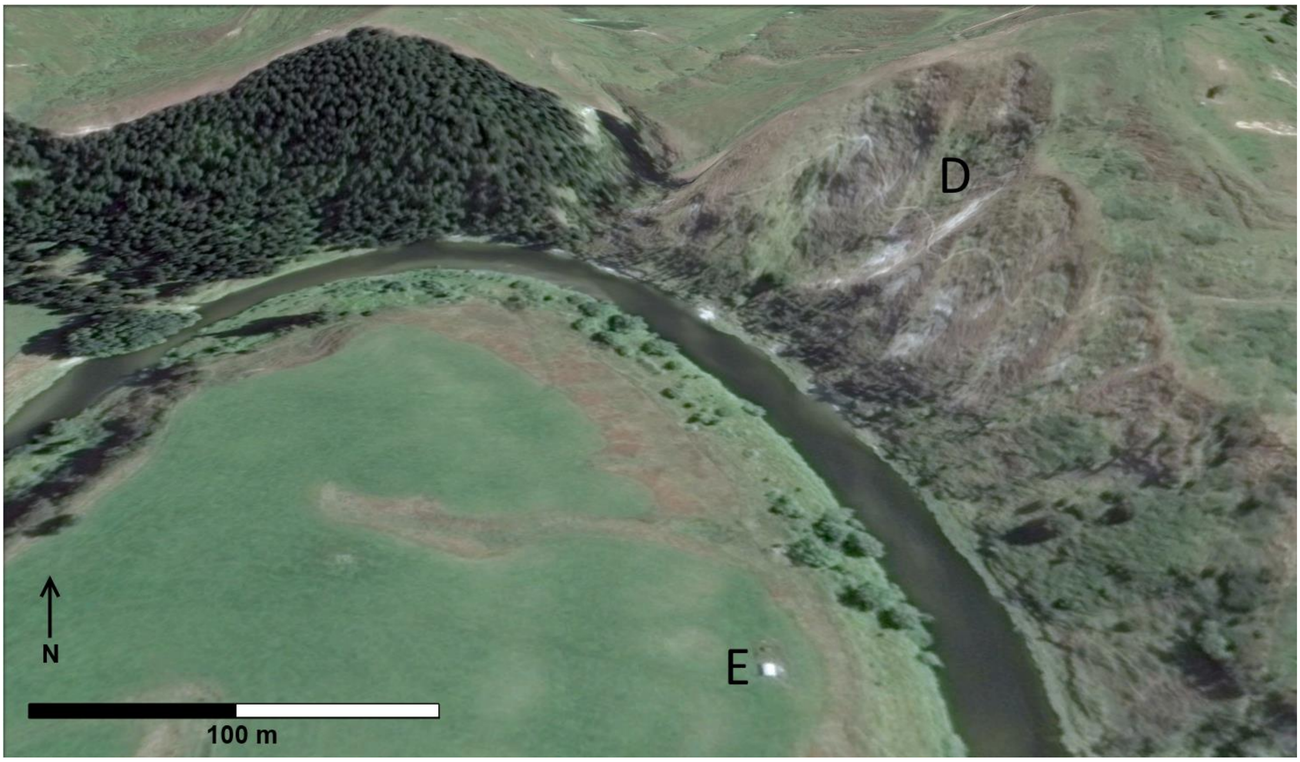

Figure 26: Location on the Waikari River identified as being having a potential landslide tsunami risk. 'E' is a building which could be at risk, 'D' shows the face most likely to fail (Google Earth).

5.6.2 Site 2

The second location is in the Moeangiangi River, 10 km south of the Waikari River (Figure 25). The potential hazard is from a hill located 600 m upstream from the mouth of the river (Figure 27). The peak of the hill is 160 m high and 200 m from the closest bank of the river. A house and two other buildings are located on the other side of the river, the closest building is 120 m away from the bank and the furthest is 150 m (Figure 27).

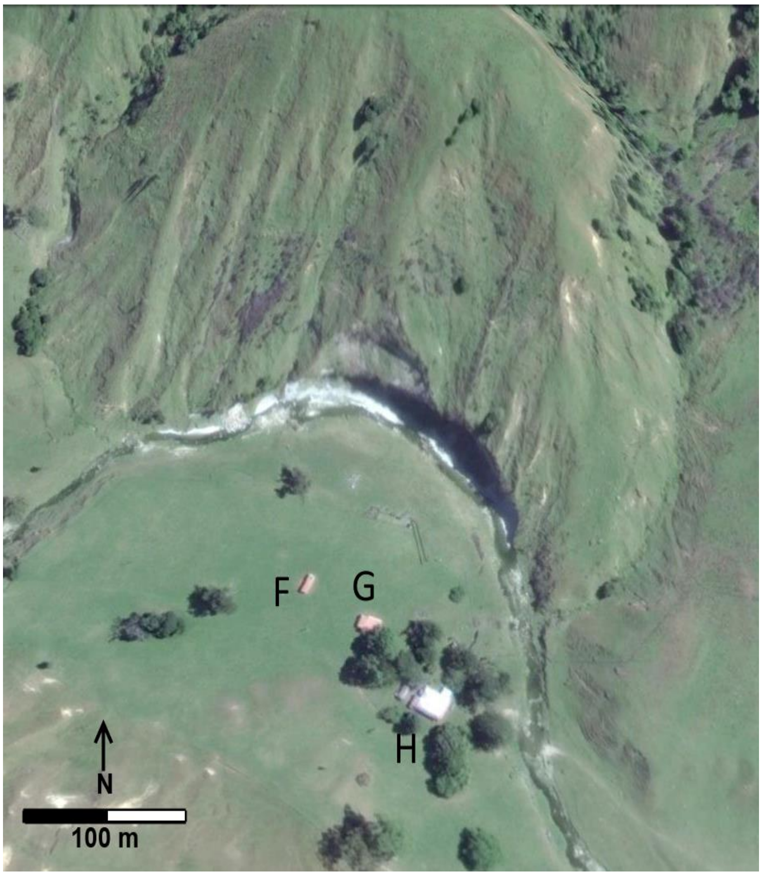

Figure 27: Location on the Moeangiangi River susceptible to a landslide and possibly landslide induced tsunami. 'F', 'G' and 'H' show the location of buildings at risk (Google Earth).

The Moeangiangi is smaller than the Waikari River and as a result any failure of the hill, would likely result in the entire body of water being displaced. This amount of water, due to the size of the river, would be unlikely to damage or even reach the buildings on the opposing bank. There is a potential for serious damage, however, if the river was in flood. Serious flooding has occurred previously when, in 1924, the river rose an additional 7.5 m after extended heavy rains (NIWA, 2008). If a landslide occurred into a swollen river it may have the potential to destroy the buildings next to the river. Periods of sustained heavy rains dramatically increase the risk of landslides therefore it is possible for a single event to swell the river to a dangerous level before causing the hill to collapse. Equally, a landslide dam breach may have catastrophic consequences for downstream land.

At both sites research needs to be carried out to determine if there is any evidence that a tsunami has previously occurred. Estimations of the likelihood of the slopes failing and the amount of displaced water if a failure were to occur need to be undertaken to properly prepare for this type of event.

6.0 Conclusions

Multiproxy analysis of a gravel layer found on Waikari Station revealed it was deposited by New Zealand's largest historic tsunami: the landslide-induced 1931 Waikari River Tsunami. Groundshaking from the 1931 Hawke's Bay Earthquake, New Zealand's deadliest natural disaster, triggered the collapse of the flank of a 120 m high hill. The landslide, with an estimated volume in excess of 1,000,000 m^3, fell into the Waikari River, damming it and producing a 15 m high wave which destroyed the homestead and a sheep shed on Waikari Station.

Analysis of ^{137}Cs activities, in addition to debris from the destroyed homestead, provided the chronology of the gravel layer found throughout the site. Cores taken from around the study area were subject to sedimentological, geochemical and microfossil analysis to determine the nature of the deposit.

Sediments deposited by the tsunami were defined by a marked increase in grainsize and a decrease in organic matter and sorting compared to the surrounding soils. Although geochemical analysis proved difficult to interpret, PCA provided the ability to spot subtle trends in geochemical counts throughout the cores. PCA exhibited similar groupings for all sites with the gravel/anomalous layer plotting next to a grouping of elements not related to detrital inputs or organic content. This grouping was a combination of Ba, Cl and S, and is believed to have originated from the tsunami. Compared to those within the surrounding soils, diatoms found within the gravel layer exhibited a higher instance of marine-brackish species which were mostly broken. It is assumed that these diatoms, which display a preference for higher salinity levels, originated from the brackish river and were subject to high energy turbulent transportation resulting in a large portion sustaining frustule damage.

During this analysis a second, earlier, deposit was identified in core WR011. This lower gravel layer also contained evidence that it was most likely to have been deposited by a tsunami, possibly generated by a landslide. Assuming constant sedimentation rates, the timing of the deposition of this gravel layers matches the timing of the M_L 7.5, 1863 Hawke's Bay Earthquake which could have been a trigger for an earlier landslide. However, further research needs to be conducted to determine the mechanism and timing of this event.

Land clearing throughout Hawke’s Bay by both Maori and European settlers has drastically changed the vegetation throughout the region, possibly resulting in decreased soil stability. This could have been a factor in the 1931 tsunami and the previous event as well as increasing the risk of future landslides. Two sites of potential risk have been identified and should act as guides for a more comprehensive analysis of surrounding catchments. Future research needs to accurately assess the risks posed by similar potential landslide-generated tsunamis throughout the river catchments of the region, in order to help mitigate potential damage to stock, property, infrastructure and human life.

7.0 References

Adams, J., 1981. Earthquake-dammed lakes in New Zealand. Geology 9, 215-219.

Anderson, R.F., Schiff, S.L., Hesslein, R.H., 1987. Determining sediment accumulation and mixing rates using ^{210}Pb, ^{137}Cs, and other tracers: problems due to post depositional mobility or coring artefacts. Canadian Journal of Fisheries and Aquatic Sciences 44, 231-250.

Appleby, P.G., Oldfield, F., 1978. The calculation of lead-210 dates assuming a constant rate of supply of unsupported 210 Pb to the sediment. Catena 5, 1-8.

Atwater, B., 1987. Evidence for Great Holocene earthquakes along the outer coast of Washington State. Science 236, 924-944.

Auckland Star, 19th March 1931. Seen from the air. Volume LXII, Issue 66, 8. http://paperspast.natlib.govt.nz/cgi-bin/paperspast?a=d&d=AS19310319.2.76&e=-------10--1----0-- [Last Accessed: 5/04/2016].

Bannister, S., 1988. Microseismicity and velocity structure in the Hawkes Bay region, New Zealand: fine structure of the subducting pacific plate. Geophysical Journal 95, 45-62.

Blott, S.J., Pye, K., 2001. GRADISTAT: a grain size distribution and statistics package for the analysis of unconsolidated sediments. Earth Surface Processes and Landforms 26, 1237-1248.

Bolin, H., Yueping, Y., Xiaoting, C., Guangning, L., Sichang, W., Zhibing, J., 2014. Experimental modelling of tsunamis generated by subaerial landslides: two case studies of the Three Gorges Reservoir, China. Environmental Earth Science 71, 3813-3825.

Bouchard, F., Francus, P., Pienitz, R., Laurion, I., 2011. Sedimentology and geochemistry of thermokarst ponds in discontinuous permafrost, subarctic Quebec, Canada. Journal of Geophysical Research 116, G00M04.

Bullen, K.E., 1938. An analysis of the Hawke's Bay earthquakes during February 1931. New Zealand Journal of Science and Technology 19, 497-519.

Carter, M., Moghissi, A., 1977. Three decades of nuclear testing. Health Physics 33, 55–71.

Chagué-Goff, C., 2010. Chemical signatures of palaeotsunamis: A forgotten proxy? Marine Geology 271, 67-71.

Chagué-Goff, C., Andrew, A., Szczuciński, W., Goff, J., & Nishimura, Y., 2010. Geochemical signatures up to the maximum inundation of the 2011 Tohoku-oki tsunami—implications for the 869AD Jogan and other palaeotsunamis. Sedimentary Geology 282, 65-77.

Chagué-Goff, C., Chan, J.C.H., Goff, J., Gadd, P., 2016. Late Holocene record of environmental changes, cyclones and tsunamis in a coastal lake, Mangaia, Cook Islands. Island Arc. Doi:10.1111/iar.12153

Chagué-Goff, C., Goff, J., Nichol, S.L., Dudley, W., Zawadzki, A., Bennett, J.W., Mooney, S.D., Fierra, D., Heiknis, H., Dominey-Howes, D., Courtney, C., 2012. Multi-proxy evidence for trans-Pacific tsunamis in the Hawai'ian Island. Marine Geology 299-302, 77-89.

Chagué-Goff, C., Goff, J., Wong, H.K.Y., Cisternas, M., 2015. Insights from geochemistry and diatoms to characterise a tsunami's deposit and maximum inundation limit. Marine Geology 359, 22-34.

Chagué-Goff, C., Schneider, J., Goff, J., Dominey-Howes, D., Strotz, L., 2011. Expanding the proxy toolkit to help identify past events — Lessons from the 2004 Indian Ocean Tsunami and the 2009 South Pacific Tsunami. Earth Science Reviews 107, 107-122.

Chappell, P.R., 2010. The climate and weather of Hawke's Bay 3rd edition. NIWA Science and Technology Series Number 58.

Clark, K.J., Upton, P., Carey, J., Rosser, B., Strong, D., 2015. Tsunami and Seiche Hazard Scoping Study for Lakes Tekapo, Pukaki, Ohau, Alexandrina and Ruataniwha, GNS Science Consultancy Report 2014/227.

Coffey, M., Dehairs, F., Collette, O., Luther, G., Church, T., Jickells, T., 1997. The behaviour of dissolved barium in estuaries. Estuarine, Coastal and Shelf Science 45, 113-121.

Cole, J.W., Lewis, K.B., 1981. Evolution of the Taupo-Hikurangi subduction system. Tectonophysics 72, 1-21.

Croudace, I.W., Rindby, A., Rothwell, R.G., 2006. ITRAX: description and evaluation of a new multi-function X-ray core scanner. Special Publication-Geological Society of London 267, 51-63.

Crozier, M.J., 1986. Landslides: Causes Consequences and Environment. Taylor & Francis.

Davis, R.B., Hess, C.T., Norton, S.A., Hanson, D.W., Hoagland, K.D., Anderson, D.S., 1984. ^{137}Cs and ^{210}Pb dating of sediments from soft-water lakes in New England (U.S.A.) and Scandinavia, a failure of ^{137}Cs dating. Chemical Geology 44, 151-185.

Davison, C., 1934. The Hawke's Bay Earthquake of February 3, 1931. Nature 133, 841-842.

Dawson, S., 2002. Diatom biostratigraphy of tsunami deposits: Examples from the 1998 Papua New Guinea tsunami. Sedimentary Geology 200, 328-335.

Dean, W.E., 1974. Determination of carbonate and organic matter in calcareous sediments and sedimentary rocks by loss on ignition: comparison with other methods. Journal of Sedimentary Research 44, 242–248.

Di Stefano, D.C., Ferro, V., Mirabile, S., 2010. Comparison between grain-size analyses using laser diffraction and sedimentation methods. Biosystems Engineering 106, 205-215.

Dinis, P., Castilho, A., 2012. Integrating sieving and laser data to obtain bulk grain-size distributions. Journal of Sedimentary Research 82, 747-754.

Dirksen, O., Van Den Bogaard, C., Danhara, T., Diekmann, B., 2011. Tephrochronological investigations at Dvuh-yurtochnoe lake area, Kamchatka: Numerous landslides and lake tsunami, and their environmental impacts. Quaternary International 246, 298-311.

Dunbar, P., McCullough, H., 2012. Global tsunami deposits database. Natural Hazards 63, 267-278.

Dura, T., Hemphill-Haley, E., Sawai, Y., Horton, B.P., 2016. The application of diatoms to reconstruct the history of subduction zone earthquakes and tsunamis. Earth-Science Reviews 152, 181-197.

Folk, R.L., Ward, W.C., 1957. Brazos River bar: a study in the significance of grain size parameters. Journal of Sedimentary Research 27, 3-26.

Fritz, H.M., Hager, W.H., Minor, H.E., 2003a. Landslide generated impulse waves; part 1: instantaneous flow fields. Experiments in Fluids 35, 505–519.

Fritz, H.M., Hager, W.H., Minor, H.E., 2003b. Landslide generated impulse waves; part 2: hydrodynamic impact craters. Experiments in Fluids 35, 520–532.

Gibowicz, S.J., 1973. Variation of the frequency-magnitude relation during earthquake sequences in New Zealand. Bulletin of the Seismological Society of America 63, 517-528.

Goff, J., Chagué-Goff, C., 2012. A review of palaeo-tsunamis for the Christchurch region, New Zealand. Quaternary Science Reviews 57, 136-156.

Goff, J., Chagué-Goff, C., Nichol, S.L., 2001. Palaeotsunami deposits: A New Zealand perspective. Sedimentary Geology 143, 1-6.

Goff, J., Chagué-Goff, C., Nichol, S.L., Jaffe, B., Dominey-Howes, D., 2012. Progress in palaeotsunami research. Sedimentary Geology 234-244, 70-88.

Goff, J., McFadgen, B.G., Chagué-Goff, C., 2004. Sedimentary differences between the 2002 Easter storm and the 15th-century Okoropunga tsunami, southeastern North Island, New Zealand. Marine Geology 204, 235-250.

Goff, J., Nichol, S., Kennedy, D., 2010. Development of a palaeotsunami database for New Zealand. Natural Hazards 54, 193-208.

Guyard, H., Chapron, E., St-Onge, G., Anselmetti, F.S., Arnaud, F., Magand, O., Francus, P., Mélières, M., 2007. High-altitude varve records of abrupt environmental changes and mining activity over the last 4000 years in the Western French Alps (Lake Bramant, Grandes Rousses Massif). Quaternary Science Reviews 26, 2644-2660.

Hawke's Bay Emergency Management Group. 2015. 1931 Napier Earthquake. Available at: http://www.hbemergency.govt.nz/hazards/earthquake/1931 [Last accessed: 28/1/2016].

Hayes, R.C., 1936. Focal depth of the Hawke's Bay earthquake of February 2-3, 1931. Nature 138, 126-127.

Heiri, O., Lotter, A.F., Lemcke, G., 2001. Loss on ignition as a method for estimating organic and carbonate content in sediments: reproducibility and comparability of results. Journal of Paleolimnology 25, 101-110.

Hemphill-Haley, E., 1996. Diatoms as an aid in identifying late-Holocene tsunami deposits. The Holocene 6, 439-448.

Hill, M., Gaillard, J.C., 2013. Integrating disaster risk reduction into post-disaster reconstruction: A long-term perspective of the 1931 earthquake in Napier, New Zealand. New Zealand Geographer 69, 108-119.

Hungr, O., Leroueil, S., Picarelli, L., 2014. The Varnes classification of landslide types, an update. Landslides 11, 167-194.

Hull, A.G., 1990. Tectonics of the 1931 Hawke's Bay earthquake. New Zealand Journal of Geology and Geophysics 33, 309-320.

Jaboyedoff, M., Oppikofer, T., Abellan, A., Derron, M., Loye, A., Metzger, R., Pedrazzini, A., 2012. Use of LIDAR in landslide investigations: a review. Natural Hazards 61, 5-28.

Jones, L.D., 2006. Monitoring landslides in hazardous terrain using terrestrial LiDAR: an example from Monsterrat. Quarterly Journal of Engineering Geology and Hydrogeology 39, 371-373.

Kershaw, P.A., 1997. A modification of the Troels-Smith system of sediment description and portrayal. Quaternary Australasia 15, 63-68.

Kirchner, G., 2011. ^{210}Pb as a tool for establishing sediment chronologies: examples of potentials and limitations of conventional dating models. Journal of Environmental Radioactivity 102, 490-494.

Kirchner, G., Ehlers, H., 1997. Sediment geochronology in changing coastal environments: potentials and limitations of the ^{137}Cs and ^{210}Pb methods. Journal of Coastal Research 14, 483-492.

Klaminder, J., Appleby, P., Crook, P., Renberg, I., 2012. Post-deposition diffusion of ^{137}Cs in lake sediment: Implications for radiocaesium dating. Sedimentology 59, 2259-2267.

Kottek, M., Grieser, J., Beck, C., Rudolf, B., Rubel, F., 2006. World Map of the Köppen-Geiger climate classification updated. Meteorologische Zeitschrift 15, 259-263.

Krishnaswamy, D.L., Martin, J.M., Meybeck, M., 1971. Geochronology of lake sediments. Earth and Planetary Science Letters 11, 407-414.

Leslie, C., Hancock, G.J., 2008. Estimating the date corresponding to the horizon of the first detection of ^{137}Cs and $^{239+240}$Pu in sediment cores. Journal of Environmental Radioactivity 99, 483-490.

Liu, P.L.F., Wu, T.R., Raichlen, F., Synolakis, C.E., Borrero, J.C., 2004. Runup and rundown generated by three-dimensional sliding masses. Journal of Fluid Mechanics 536, 107-144.

Matthews, K.M., 1989. Radioactive fallout in the South Pacific: a history Part 1: deposition in New Zealand. National Radiation Lab.

Miller, D.J., 1960. The Alaska earthquake of July 10, 1958: giant wave in Lituya Bay. Bulletin of the Seismological Society of America 50, 253-266.

Morton, R.A., Gelfenbaum, G., Jaffe, B.E., 2007. Physical criteria for distinguishing sandy tsunami and storm deposits using modern examples. Sedimentary Geology 200, 184-207.

National Institute of Water and Atmospheric Research (NIWA)., 2008. March 1924 Hawke's Bay Flooding (1924-03-11). NIWA Historic Weather Event Catalogue.

Pennington, W., Tutin, T.G., Cambray, R.S., Fisher, E.M., 1973. Observations on lake sediments using fallout ^{137}Cs as a tracer. Nature 242, 324-326.

Pereira, H.G., Renca, S., Saraiva, J., 2003. A case study on geochemical anomaly identification through principal components analysis supplementary projection. Applied Geochemistry 18, 37-44.

Pillans, B., 1986. A late quaternary uplift map for North Island, New Zealand. Royal Society of New Zealand Bulletin 24, 409-417.

Renberg, I., 1990. A procedure for preparing large sets of diatom slides from sediment cores. Journal of Paleolimnology 4, 87-90.

Reyners, M., 1980. A microearthquake study of the plate boundary, North Island, New Zealand. Geophysical journal of the Royal Astronomical Society 63, 1-22.

Richmond B., Szczuciński, W., Chagué-Goff, C., Goto, K., Sugawara, D., Witter, R., Tappin, D.R., Jaffe, B., Fujino, S., Nishimura, Y., Goff, J., 2012. Erosion, deposition and landscape change on the Sendai coastal plain, Japan, resulting from the March 11, 2011 Tohoku-oki tsunami. Sedimentary Geology 282, 27-39.

Ritchie, J.C., McHenry, R., 1990. Application of radioactive fallout Cesium-137 for measuring soil erosion and sediment accumulation rates and patterns: a review. Journal of Environmental Quality 19, 215-233.

Robbins, J.A., Edginton, D.N., 1975. Determination of recent sedimentation rates in Lake Michigan using Pb-210 and Cs-137. Geochimica Cosmochimica Acta 39, 285-304.

Schuller, P., Løvengreen, C., Handl, J., 1993. ^{137}Cs concentration in soil, prairie plants, and milk from sites in Southern Chile. Health Physics 64, 157-161.

Smith, W.D., 1978. Spatial distribution of felt intensities for New Zealand earthquakes. New Zealand Journal of Geology and Geophysics 21, 293-311.

Sperazza, M., Moore, J.N., Hendrix, M.S., 2004. High-resolution particle size analysis of naturally occurring very fine-grained sediment through laser diffractometry. Journal of Sedimentary Research 74, 736-743.

Stirling, M. W, Wesnousky, S.G, Berryman, K.R., 1998. Probabilistic seismic hazard analysis of New Zealand. New Zealand Journal of Geology and Geophysics 41, 355-375.

Tait, S. U., 1977. Waikari Station 1840 to 1940. Hawke’s Bay Regional Council (HBRC) Report No. AM15-16, HBRC plan No. 4751.

Van der Weijden, C.H., 2002. Pitfalls of normalization of marine geochemical data using a common divisor. Marine Geology 184, 167-187.

Van der Werff, A., Huls, H., 1957-1974. Diatomeënflora van Nederland 1–10. Otto Koeltz Science Publishers, Koenigstein. Reprinted 1976.

Viroulet, S., C´ebron, D., Kimmoun, O., Kharif, C., 2013. Shallow water waves generated by subaerial solid landslides. Geophysical Journal International 193, 747-762.

Wilmshurt, J., 1997a. A late Holocene history of natural disturbance in lowland podocarp/hardwood forest, Hawke’s Bay, New Zealand. New Zealand Journal of Botany 35, 79-96.

Wilmshurt, J., 1997b. The impact of human settlement on vegetation and soil stability in Hawke’s Bay, New Zealand. New Zealand Journal of Botany 35, 97-111.

Xue, J., Lee, C., Wakeham, S.G., Armstrong, R.A., 2011. Using principal components analysis (PCA) with cluster analysis to study the organic geochemistry of sinking particles in the ocean. Organic Geochemistry 42, 356-367.

8.0 Appendices

Appendix A–Stratigraphy data:

Appendix A.1-Sample locations and description:

Sample Name	GPS Data		Sample Type	Comments
	Latitude	**Longitude**		
WR001	-39.170429	177.085757	Grab	River bank, landslide side
WR002	-39.170312	177.085595	Grab	Side wall, landslide side
WR003	-39.170053	177.08233	Grab	Side wall, landslide side
WR004	-39.168288	177.079584	Grab	Landslide face, landslide side
WR005	-39.167566	177.080985	Core	Terrace sidewall of homestead paddock, station side
WR006	-39.167071	177.080895	Stratigraphy description	Terrace wall around river bend, station side
WR007	-39.168133	177.08198	Core	Sheep shed paddock, station side
WR008	-39.167836	177.081517	Core	Between sheep shed paddock & homestead paddock, station side
WR009	-39.167386	177.081135	Core	Homestead paddock, station side
WR010	-39.167287	177.081597	Core	Homestead paddock, station side
WR011	-39.168323	177.082096	Core	Side wall of sheep shed paddock, station side
WR012-T	-39.167387	177.080498	Grab	Lowest terrace, station side

Appendix A.2-Gradistat data:

WR005 Gradistat data

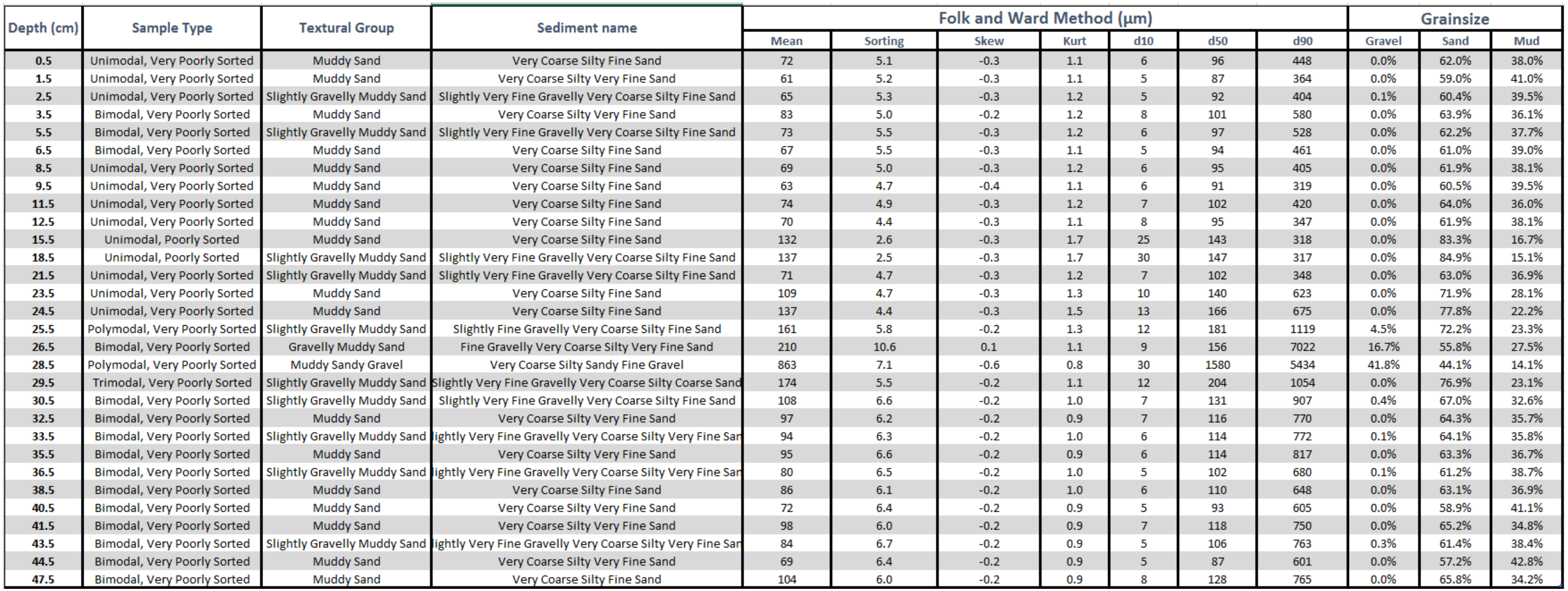

Depth (cm)	Sample Type	Textural Group	Sediment name	Folk and Ward Method (µm)							Grainsize		
				Mean	Sorting	Skew	Kurt	d10	d50	d90	Gravel	Sand	Mud
0.5	Unimodal, Very Poorly Sorted	Muddy Sand	Very Coarse Silty Fine Sand	72	5.1	-0.3	1.1	6	96	448	0.0%	62.0%	38.0%
1.5	Unimodal, Very Poorly Sorted	Muddy Sand	Very Coarse Silty Very Fine Sand	61	5.2	-0.3	1.1	5	87	364	0.0%	59.0%	41.0%
2.5	Unimodal, Very Poorly Sorted	Slightly Gravelly Muddy Sand	Slightly Very Fine Gravelly Very Coarse Silty Fine Sand	65	5.3	-0.3	1.2	5	92	404	0.1%	60.4%	39.5%
3.5	Bimodal, Very Poorly Sorted	Muddy Sand	Very Coarse Silty Very Fine Sand	83	5.0	-0.2	1.2	8	101	580	0.0%	63.9%	36.1%
5.5	Bimodal, Very Poorly Sorted	Slightly Gravelly Muddy Sand	Slightly Very Fine Gravelly Very Coarse Silty Fine Sand	73	5.5	-0.3	1.2	6	97	528	0.0%	62.2%	37.7%
6.5	Bimodal, Very Poorly Sorted	Muddy Sand	Very Coarse Silty Fine Sand	67	5.5	-0.3	1.1	5	94	461	0.0%	61.0%	39.0%
8.5	Unimodal, Very Poorly Sorted	Muddy Sand	Very Coarse Silty Fine Sand	69	5.0	-0.3	1.2	6	95	405	0.0%	61.9%	38.1%
9.5	Unimodal, Very Poorly Sorted	Muddy Sand	Very Coarse Silty Fine Sand	63	4.7	-0.4	1.1	6	91	319	0.0%	60.5%	39.5%
11.5	Unimodal, Very Poorly Sorted	Muddy Sand	Very Coarse Silty Fine Sand	74	4.9	-0.3	1.2	7	102	420	0.0%	64.0%	36.0%
12.5	Unimodal, Very Poorly Sorted	Muddy Sand	Very Coarse Silty Fine Sand	70	4.4	-0.3	1.1	8	95	347	0.0%	61.9%	38.1%
15.5	Unimodal, Poorly Sorted	Muddy Sand	Very Coarse Silty Fine Sand	132	2.6	-0.3	1.7	25	143	318	0.0%	83.3%	16.7%
18.5	Unimodal, Poorly Sorted	Slightly Gravelly Muddy Sand	Slightly Very Fine Gravelly Very Coarse Silty Fine Sand	137	2.5	-0.3	1.7	30	147	317	0.0%	84.9%	15.1%
21.5	Unimodal, Very Poorly Sorted	Slightly Gravelly Muddy Sand	Slightly Very Fine Gravelly Very Coarse Silty Fine Sand	71	4.7	-0.3	1.2	7	102	348	0.0%	63.0%	36.9%
23.5	Unimodal, Very Poorly Sorted	Muddy Sand	Very Coarse Silty Fine Sand	109	4.7	-0.3	1.3	10	140	623	0.0%	71.9%	28.1%
24.5	Unimodal, Very Poorly Sorted	Muddy Sand	Very Coarse Silty Fine Sand	137	4.4	-0.3	1.5	13	166	675	0.0%	77.8%	22.2%
25.5	Polymodal, Very Poorly Sorted	Slightly Gravelly Muddy Sand	Slightly Fine Gravelly Very Coarse Silty Fine Sand	161	5.8	-0.2	1.3	12	181	1119	4.5%	72.2%	23.3%
26.5	Bimodal, Very Poorly Sorted	Gravelly Muddy Sand	Fine Gravelly Very Coarse Silty Very Fine Sand	210	10.6	0.1	1.1	9	156	7022	16.7%	55.8%	27.5%
28.5	Polymodal, Very Poorly Sorted	Muddy Sandy Gravel	Very Coarse Silty Sandy Fine Gravel	863	7.1	-0.6	0.8	30	1580	5434	41.8%	44.1%	14.1%
29.5	Trimodal, Very Poorly Sorted	Slightly Gravelly Muddy Sand	Slightly Very Fine Gravelly Very Coarse Silty Coarse Sand	174	5.5	-0.2	1.1	12	204	1054	0.0%	76.9%	23.1%
30.5	Bimodal, Very Poorly Sorted	Slightly Gravelly Muddy Sand	Slightly Very Fine Gravelly Very Coarse Silty Fine Sand	108	6.6	-0.2	1.0	7	131	907	0.4%	67.0%	32.6%
32.5	Bimodal, Very Poorly Sorted	Muddy Sand	Very Coarse Silty Very Fine Sand	97	6.2	-0.2	0.9	7	116	770	0.0%	64.3%	35.7%
33.5	Bimodal, Very Poorly Sorted	Slightly Gravelly Muddy Sand	ightly Very Fine Gravelly Very Coarse Silty Very Fine Sar	94	6.3	-0.2	1.0	6	114	772	0.1%	64.1%	35.8%
35.5	Bimodal, Very Poorly Sorted	Muddy Sand	Very Coarse Silty Very Fine Sand	95	6.6	-0.2	0.9	6	114	817	0.0%	63.3%	36.7%
36.5	Bimodal, Very Poorly Sorted	Slightly Gravelly Muddy Sand	ightly Very Fine Gravelly Very Coarse Silty Very Fine Sar	80	6.5	-0.2	1.0	5	102	680	0.1%	61.2%	38.7%
38.5	Bimodal, Very Poorly Sorted	Muddy Sand	Very Coarse Silty Fine Sand	86	6.1	-0.2	1.0	6	110	648	0.0%	63.1%	36.9%
40.5	Bimodal, Very Poorly Sorted	Muddy Sand	Very Coarse Silty Very Fine Sand	72	6.4	-0.2	0.9	5	93	605	0.0%	58.9%	41.1%
41.5	Bimodal, Very Poorly Sorted	Muddy Sand	Very Coarse Silty Very Fine Sand	98	6.0	-0.2	0.9	7	118	750	0.0%	65.2%	34.8%
43.5	Bimodal, Very Poorly Sorted	Slightly Gravelly Muddy Sand	ightly Very Fine Gravelly Very Coarse Silty Very Fine Sar	84	6.7	-0.2	0.9	5	106	763	0.3%	61.4%	38.4%
44.5	Bimodal, Very Poorly Sorted	Muddy Sand	Very Coarse Silty Very Fine Sand	69	6.4	-0.2	0.9	5	87	601	0.0%	57.2%	42.8%
47.5	Bimodal, Very Poorly Sorted	Muddy Sand	Very Coarse Silty Fine Sand	104	6.0	-0.2	0.9	8	128	765	0.0%	65.8%	34.2%

WR007 Gradistat Data

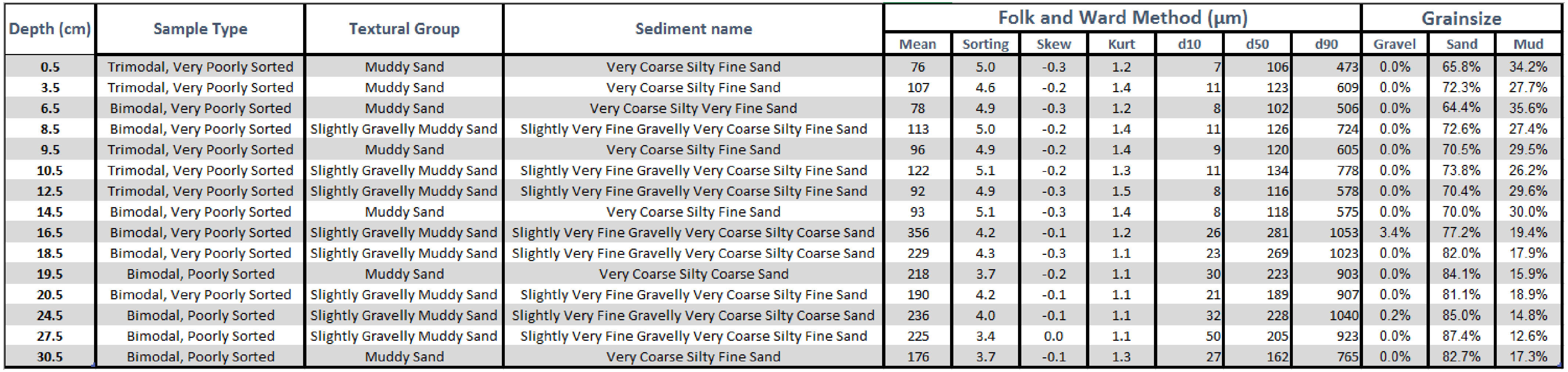

Depth (cm)	Sample Type	Textural Group	Sediment name	Folk and Ward Method (µm)							Grainsize		
				Mean	Sorting	Skew	Kurt	d10	d50	d90	Gravel	Sand	Mud
0.5	Trimodal, Very Poorly Sorted	Muddy Sand	Very Coarse Silty Fine Sand	76	5.0	-0.3	1.2	7	106	473	0.0%	65.8%	34.2%
3.5	Trimodal, Very Poorly Sorted	Muddy Sand	Very Coarse Silty Fine Sand	107	4.6	-0.2	1.4	11	123	609	0.0%	72.3%	27.7%
6.5	Bimodal, Very Poorly Sorted	Muddy Sand	Very Coarse Silty Very Fine Sand	78	4.9	-0.3	1.2	8	102	506	0.0%	64.4%	35.6%
8.5	Bimodal, Very Poorly Sorted	Slightly Gravelly Muddy Sand	Slightly Very Fine Gravelly Very Coarse Silty Fine Sand	113	5.0	-0.2	1.4	11	126	724	0.0%	72.6%	27.4%
9.5	Trimodal, Very Poorly Sorted	Muddy Sand	Very Coarse Silty Fine Sand	96	4.9	-0.2	1.4	9	120	605	0.0%	70.5%	29.5%
10.5	Trimodal, Very Poorly Sorted	Slightly Gravelly Muddy Sand	Slightly Very Fine Gravelly Very Coarse Silty Fine Sand	122	5.1	-0.2	1.3	11	134	778	0.0%	73.8%	26.2%
12.5	Trimodal, Very Poorly Sorted	Slightly Gravelly Muddy Sand	Slightly Very Fine Gravelly Very Coarse Silty Fine Sand	92	4.9	-0.3	1.5	8	116	578	0.0%	70.4%	29.6%
14.5	Bimodal, Very Poorly Sorted	Muddy Sand	Very Coarse Silty Fine Sand	93	5.1	-0.3	1.4	8	118	575	0.0%	70.0%	30.0%
16.5	Bimodal, Very Poorly Sorted	Slightly Gravelly Muddy Sand	Slightly Very Fine Gravelly Very Coarse Silty Coarse Sand	356	4.2	-0.1	1.2	26	281	1053	3.4%	77.2%	19.4%
18.5	Bimodal, Very Poorly Sorted	Slightly Gravelly Muddy Sand	Slightly Very Fine Gravelly Very Coarse Silty Coarse Sand	229	4.3	-0.3	1.1	23	269	1023	0.0%	82.0%	17.9%
19.5	Bimodal, Poorly Sorted	Muddy Sand	Very Coarse Silty Coarse Sand	218	3.7	-0.2	1.1	30	223	903	0.0%	84.1%	15.9%
20.5	Bimodal, Very Poorly Sorted	Slightly Gravelly Muddy Sand	Slightly Very Fine Gravelly Very Coarse Silty Fine Sand	190	4.2	-0.1	1.1	21	189	907	0.0%	81.1%	18.9%
24.5	Bimodal, Poorly Sorted	Slightly Gravelly Muddy Sand	Slightly Very Fine Gravelly Very Coarse Silty Coarse Sand	236	4.0	-0.1	1.1	32	228	1040	0.2%	85.0%	14.8%
27.5	Bimodal, Poorly Sorted	Slightly Gravelly Muddy Sand	Slightly Very Fine Gravelly Very Coarse Silty Fine Sand	225	3.4	0.0	1.1	50	205	923	0.0%	87.4%	12.6%
30.5	Bimodal, Poorly Sorted	Muddy Sand	Very Coarse Silty Fine Sand	176	3.7	-0.1	1.3	27	162	765	0.0%	82.7%	17.3%

WR008 Gradistat Data

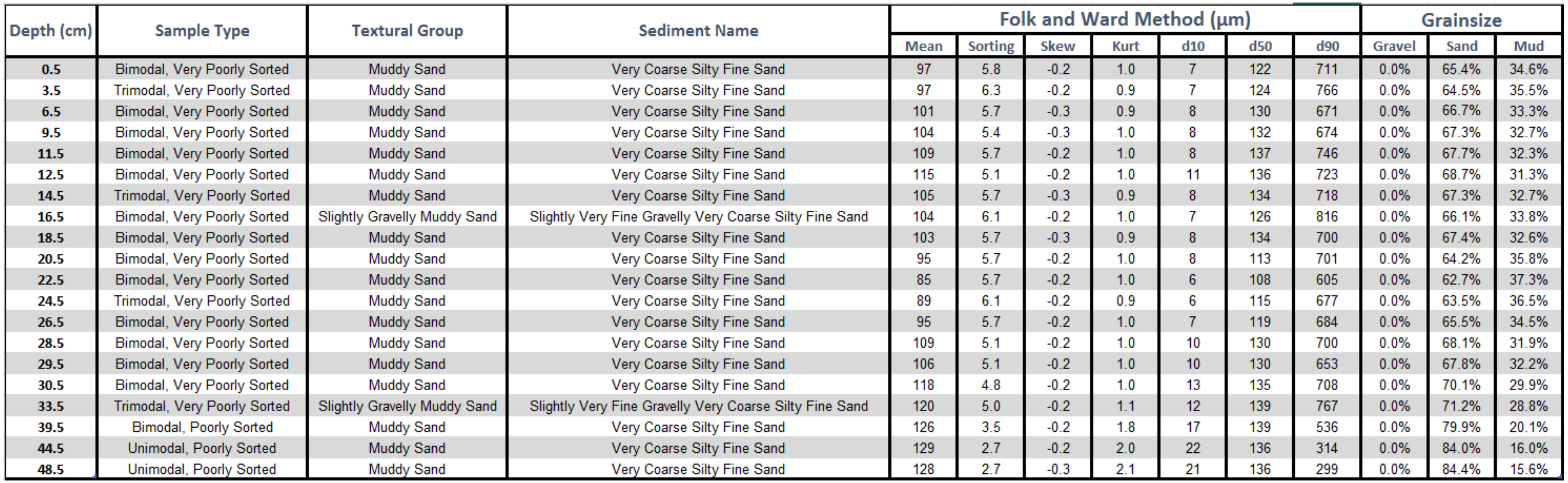

Depth (cm)	Sample Type	Textural Group	Sediment Name	Folk and Ward Method (µm)							Grainsize		
				Mean	Sorting	Skew	Kurt	d10	d50	d90	Gravel	Sand	Mud
0.5	Bimodal, Very Poorly Sorted	Muddy Sand	Very Coarse Silty Fine Sand	97	5.8	-0.2	1.0	7	122	711	0.0%	65.4%	34.6%
3.5	Trimodal, Very Poorly Sorted	Muddy Sand	Very Coarse Silty Fine Sand	97	6.3	-0.2	0.9	7	124	766	0.0%	64.5%	35.5%
6.5	Bimodal, Very Poorly Sorted	Muddy Sand	Very Coarse Silty Fine Sand	101	5.7	-0.3	0.9	8	130	671	0.0%	66.7%	33.3%
9.5	Bimodal, Very Poorly Sorted	Muddy Sand	Very Coarse Silty Fine Sand	104	5.4	-0.3	1.0	8	132	674	0.0%	67.3%	32.7%
11.5	Bimodal, Very Poorly Sorted	Muddy Sand	Very Coarse Silty Fine Sand	109	5.7	-0.2	1.0	8	137	746	0.0%	67.7%	32.3%
12.5	Bimodal, Very Poorly Sorted	Muddy Sand	Very Coarse Silty Fine Sand	115	5.1	-0.2	1.0	11	136	723	0.0%	68.7%	31.3%
14.5	Trimodal, Very Poorly Sorted	Muddy Sand	Very Coarse Silty Fine Sand	105	5.7	-0.3	0.9	8	134	718	0.0%	67.3%	32.7%
16.5	Bimodal, Very Poorly Sorted	Slightly Gravelly Muddy Sand	Slightly Very Fine Gravelly Very Coarse Silty Fine Sand	104	6.1	-0.2	1.0	7	126	816	0.0%	66.1%	33.8%
18.5	Bimodal, Very Poorly Sorted	Muddy Sand	Very Coarse Silty Fine Sand	103	5.7	-0.3	0.9	8	134	700	0.0%	67.4%	32.6%
20.5	Bimodal, Very Poorly Sorted	Muddy Sand	Very Coarse Silty Fine Sand	95	5.7	-0.2	1.0	8	113	701	0.0%	64.2%	35.8%
22.5	Bimodal, Very Poorly Sorted	Muddy Sand	Very Coarse Silty Fine Sand	85	5.7	-0.2	1.0	6	108	605	0.0%	62.7%	37.3%
24.5	Trimodal, Very Poorly Sorted	Muddy Sand	Very Coarse Silty Fine Sand	89	6.1	-0.2	0.9	6	115	677	0.0%	63.5%	36.5%
26.5	Bimodal, Very Poorly Sorted	Muddy Sand	Very Coarse Silty Fine Sand	95	5.7	-0.2	1.0	7	119	684	0.0%	65.5%	34.5%
28.5	Bimodal, Very Poorly Sorted	Muddy Sand	Very Coarse Silty Fine Sand	109	5.1	-0.2	1.0	10	130	700	0.0%	68.1%	31.9%
29.5	Bimodal, Very Poorly Sorted	Muddy Sand	Very Coarse Silty Fine Sand	106	5.1	-0.2	1.0	10	130	653	0.0%	67.8%	32.2%
30.5	Bimodal, Very Poorly Sorted	Muddy Sand	Very Coarse Silty Fine Sand	118	4.8	-0.2	1.0	13	135	708	0.0%	70.1%	29.9%
33.5	Trimodal, Very Poorly Sorted	Slightly Gravelly Muddy Sand	Slightly Very Fine Gravelly Very Coarse Silty Fine Sand	120	5.0	-0.2	1.1	12	139	767	0.0%	71.2%	28.8%
39.5	Bimodal, Poorly Sorted	Muddy Sand	Very Coarse Silty Fine Sand	126	3.5	-0.2	1.8	17	139	536	0.0%	79.9%	20.1%
44.5	Unimodal, Poorly Sorted	Muddy Sand	Very Coarse Silty Fine Sand	129	2.7	-0.2	2.0	22	136	314	0.0%	84.0%	16.0%
48.5	Unimodal, Poorly Sorted	Muddy Sand	Very Coarse Silty Fine Sand	128	2.7	-0.3	2.1	21	136	299	0.0%	84.4%	15.6%

WR009 Gradistat Data

Depth (cm)	Sample Type	Textural Group	Sediment name	Folk and Ward Method (µm)							Grainsize		
				Mean	Sorting	Skew	Kurt	d10	d50	d90	Gravel	Sand	Mud
0.5	Bimodal, Very Poorly Sorted	Sandy Mud	Very Fine Sandy Very Coarse Silt	38	5.0	-0.3	1.0	3	55	207	0.0%	46.5%	53.5%
3.5	Bimodal, Very Poorly Sorted	Muddy Sand	Very Coarse Silty Very Fine Sand	47	4.9	-0.3	1.1	4	64	260	0.0%	50.9%	49.1%
6.5	Bimodal, Very Poorly Sorted	Muddy Sand	Very Coarse Silty Very Fine Sand	47	5.4	-0.3	1.1	4	68	300	0.0%	52.4%	47.6%
8.5	Polymodal, Very Poorly Sorted	Gravelly Mud	Fine Gravelly Very Coarse Silt	48	7.0	-0.1	1.4	4	66	542	5.2%	46.2%	48.6%
9.5	Bimodal, Very Poorly Sorted	Sandy Mud	Very Fine Sandy Very Coarse Silt	42	4.7	-0.3	1.1	4	59	216	0.0%	48.2%	51.8%
10.5	Unimodal, Very Poorly Sorted	Sandy Mud	Very Fine Sandy Very Coarse Silt	44	4.1	-0.3	1.0	5	58	205	0.0%	47.8%	52.2%
12.5	Unimodal, Very Poorly Sorted	Sandy Mud	Very Fine Sandy Very Coarse Silt	37	4.9	-0.3	1.0	3	54	195	0.0%	45.6%	54.4%
14.5	Unimodal, Very Poorly Sorted	Sandy Mud	Very Fine Sandy Very Coarse Silt	40	4.4	-0.4	1.1	4	56	182	0.0%	46.3%	53.7%
16.5	Bimodal, Very Poorly Sorted	Gravelly Muddy Sand	Fine Gravelly Very Coarse Silty Very Fine Sand	83	10.1	0.1	1.6	5	81	6756	13.7%	43.6%	42.7%
18.5	Polymodal, Very Poorly Sorted	Muddy Sandy Gravel	Very Coarse Silty Sandy Medium Gravel	379	14.6	0.1	0.7	10	249	9215	42.0%	32.6%	25.4%
20.5	Polymodal, Very Poorly Sorted	Gravelly Muddy Sand	Fine Gravelly Very Coarse Silty Very Fine Sand	234	13.1	0.2	0.8	8	128	6054	24.7%	45.6%	29.7%
22.5	Unimodal, Very Poorly Sorted	Gravelly Muddy Sand	Medium Gravelly Very Coarse Silty Very Fine Sand	171	13.5	0.1	1.3	6	115	8176	16.8%	49.4%	33.8%
24.5	Unimodal, Very Poorly Sorted	Gravelly Muddy Sand	Fine Gravelly Very Coarse Silty Fine Sand	111	8.9	0.0	1.2	7	125	7102	12.7%	52.9%	34.5%
25.5	Unimodal, Very Poorly Sorted	Muddy Sand	Very Coarse Silty Medium Sand	107	5.6	-0.3	0.9	8	142	707	0.0%	65.2%	34.8%
26.5	Unimodal, Very Poorly Sorted	Muddy Sand	Very Coarse Silty Medium Sand	104	5.5	-0.3	0.9	8	138	668	0.0%	64.6%	35.4%
30.5	Unimodal, Very Poorly Sorted	Muddy Sand	Very Coarse Silty Coarse Sand	107	6.0	-0.3	0.8	8	143	774	0.0%	63.4%	36.6%
36.5	Unimodal, Very Poorly Sorted	Muddy Sand	Very Coarse Silty Medium Sand	120	5.5	-0.3	0.9	9	165	754	0.0%	67.3%	32.7%
42.5	Unimodal, Very Poorly Sorted	Muddy Sand	Very Coarse Silty Coarse Sand	114	5.5	-0.2	0.8	10	141	768	0.0%	64.3%	35.7%

WR010 Gradistat Data

Depth (cm)	Sample Type	Textural Group	Sediment name	Folk and Ward Method (µm)							Grainsize		
				Mean	Sorting	Skew	Kurt	d10	d50	d90	Gravel	Sand	Mud
0.5	Bimodal, Very Poorly Sorted	Muddy Sand	Very Coarse Silty Very Fine Sand	105	5.8	-0.2	1.0	8	121	799	0.0%	66.5%	33.5%
3.5	Trimodal, Very Poorly Sorted	Muddy Sand	Very Coarse Silty Fine Sand	76	5.9	-0.3	0.9	6	100	562	0.0%	61.1%	38.9%
6.5	Trimodal, Very Poorly Sorted	Muddy Sand	Very Coarse Silty Fine Sand	98	6.4	-0.2	0.9	7	122	790	0.0%	65.2%	34.8%
9.5	Polymodal, Very Poorly Sorted	Slightly Gravelly Muddy Sand	Slightly Very Fine Gravelly Very Coarse Silty Very Fine San	111	6.3	-0.2	1.0	8	132	908	0.0%	68.3%	31.6%
12.5	Trimodal, Very Poorly Sorted	Gravelly Muddy Sand	Fine Gravelly Very Coarse Silty Very Fine Sand	118	7.7	-0.1	1.1	8	133	1273	9.6%	57.5%	32.9%
16.5	Polymodal, Very Poorly Sorted	Slightly Gravelly Muddy Sand	Slightly Very Fine Gravelly Very Coarse Silty Coarse Sand	99	7.6	-0.1	0.8	6	113	1042	0.1%	59.7%	40.2%
18.5	Bimodal, Very Poorly Sorted	Muddy Sand	Very Coarse Silty Coarse Sand	132	6.0	-0.3	0.9	9	189	897	0.0%	68.6%	31.4%
22.5	Trimodal, Very Poorly Sorted	Slightly Gravelly Muddy Sand	Slightly Very Fine Gravelly Very Coarse Silty Coarse Sand	113	7.0	-0.2	0.8	7	142	1020	0.0%	63.1%	36.8%
26.5	Bimodal, Very Poorly Sorted	Muddy Sand	Very Coarse Silty Coarse Sand	118	5.9	-0.2	0.8	9	141	886	0.0%	64.4%	35.6%
32.5	Trimodal, Very Poorly Sorted	Slightly Gravelly Muddy Sand	Slightly Very Fine Gravelly Very Coarse Silty Coarse Sand	110	7.0	-0.2	0.8	6	146	954	0.0%	63.3%	36.7%
38.5	Bimodal, Very Poorly Sorted	Slightly Gravelly Muddy Sand	Slightly Very Fine Gravelly Very Coarse Silty Coarse Sand	122	6.0	-0.2	0.9	9	143	922	0.0%	67.9%	32.1%
41.5	Bimodal, Very Poorly Sorted	Muddy Sand	Very Coarse Silty Very Fine Sand	99	6.1	-0.2	0.9	7	110	804	0.0%	63.4%	36.6%
47.5	Unimodal, Very Poorly Sorted	Muddy Sand	Very Coarse Silty Very Fine Sand	61	5.0	-0.3	1.2	5	82	374	0.0%	58.1%	41.9%

WR011 Gradistat Data

Depth (cm)	Sample Type	Textural Group	Sediment name	Folk and Ward Method (µm)							Grainsize		
				Mean	Sorting	Skew	Kurt	d10	d50	d90	Gravel	Sand	Mud
0.5	Bimodal, Very Poorly Sorted	Muddy Sand	Very Coarse Silty Very Fine Sand	45	5.1	-0.4	1.0	4	70	238	0.0%	53.3%	46.7%
3.5	Bimodal, Very Poorly Sorted	Muddy Sand	Very Coarse Silty Very Fine Sand	52	5.2	-0.4	1.1	4	80	289	0.0%	57.6%	42.4%
6.5	Bimodal, Very Poorly Sorted	Muddy Sand	Very Coarse Silty Very Fine Sand	43	5.0	-0.4	1.0	4	64	230	0.0%	50.6%	49.4%
11.5	Trimodal, Very Poorly Sorted	Muddy Sand	Very Coarse Silty Very Fine Sand	49	5.3	-0.4	1.1	4	77	283	0.0%	56.3%	43.7%
12.5	Bimodal, Very Poorly Sorted	Gravelly Muddy Sand	Fine Gravelly Very Coarse Silty Very Fine Sand	74	8.3	-0.1	1.7	5	97	1637	10.0%	53.6%	36.4%
13.5	Trimodal, Very Poorly Sorted	Gravelly Muddy Sand	Fine Gravelly Very Coarse Silty Very Fine Sand	142	13.7	0.1	1.3	5	96	5388	16.9%	44.3%	38.8%
15.5	Polymodal, Very Poorly Sorted	Muddy Sandy Gravel	Very Coarse Silty Sandy Medium Gravel	1614	10.6	-0.8	0.7	27	5945	10436	63.8%	21.2%	15.0%
17.5	Polymodal, Very Poorly Sorted	Muddy Sandy Gravel	Very Coarse Silty Sandy Fine Gravel	1888	8.3	-0.8	3.8	57	6253	10135	75.7%	13.7%	10.6%
18.5	Polymodal, Poorly Sorted	Gravel	Fine Gravel	5609	3.1	-0.8	5.9	113	7096	9277	84.2%	9.0%	6.8%
20.5	Polymodal, Very Poorly Sorted	Gravel	Fine Gravel	3398	4.6	-0.8	5.0	98	6355	9939	83.3%	9.4%	7.3%
21.5	Trimodal, Very Poorly Sorted	Gravelly Muddy Sand	Medium Gravelly Very Coarse Silty Very Fine Sand	154	14.2	0.2	1.5	5	97	6466	17.8%	45.4%	36.8%
24.5	Unimodal, Very Poorly Sorted	Muddy Sand	Very Coarse Silty Very Fine Sand	43	4.8	-0.4	1.0	4	66	216	0.0%	51.5%	48.5%
30.5	Polymodal, Very Poorly Sorted	Gravelly Muddy Sand	Fine Gravelly Very Coarse Silty Very Fine Sand	143	14.4	0.1	1.4	5	90	5136	17.9%	42.5%	39.6%
33.5	Polymodal, Very Poorly Sorted	Muddy Sandy Gravel	Very Coarse Silty Sandy Fine Gravel	954	9.3	-0.8	0.8	18	3324	5917	58.2%	23.4%	18.4%
34.5	Polymodal, Very Poorly Sorted	Muddy Sandy Gravel	Very Coarse Silty Sandy Fine Gravel	1605	8.2	-0.8	2.0	53	4683	10064	74.9%	13.9%	11.2%
36.5	Trimodal, Poorly Sorted	Gravel	Medium Gravel	5740	2.1	-3.0	1.6	104	13356	99528	85.1%	7.7%	7.2%
37.5	Trimodal, Very Poorly Sorted	Gravelly Mud	Fine Gravelly Very Coarse Silt	127	14.6	0.1	1.5	4	78	4637	16.8%	40.1%	43.1%
38.5	Unimodal, Very Poorly Sorted	Sandy Mud	Very Fine Sandy Very Coarse Silt	36	4.5	-0.4	1.0	3	56	164	0.0%	46.2%	53.8%
41.5	Unimodal, Very Poorly Sorted	Sandy Mud	Very Fine Sandy Very Coarse Silt	34	4.6	-0.5	1.0	3	53	153	0.0%	44.7%	55.3%
47.5	Unimodal, Very Poorly Sorted	Sandy Mud	Very Fine Sandy Very Coarse Silt	34	4.4	-0.5	1.0	3	53	144	0.0%	44.3%	55.7%

Appendix B- Loss-on-ignition data:

Moisture content and LOI of WR005 and WR008

WR005

Depth (cm)	Moisture (%)	LOI (%)
0-1	11.1	5.3
1-2	11.8	5.0
2-3	11.4	4.9
5-6	10.6	4.1
8-9	11.7	4.7
11-12	11.5	4.3
15-16	10.2	3.5
30-31	15.7	7.0
33-34	17.8	7.9
36-37	18.4	7.9
40-41	19.1	7.1
43-44	20.0	7.5

WR008

Depth (cm)	Moisture (%)	LOI (%)
3-4	18.8	13.5
9-10	16.2	10.6
14-15	16.0	9.2
18-19	20.7	9.9
24-25	21.2	9.5
29-30	23.6	8.3
33-34	19.2	5.4
39-40	14.5	2.6
44-45	11.7	2.3
48-49	11.9	1.8

Appendix C- Geochemistry:

All count data (apart from Mo-ratio) are normalised over KCPS. The green shaded area in each figure shows the location of the anomalous deposit.

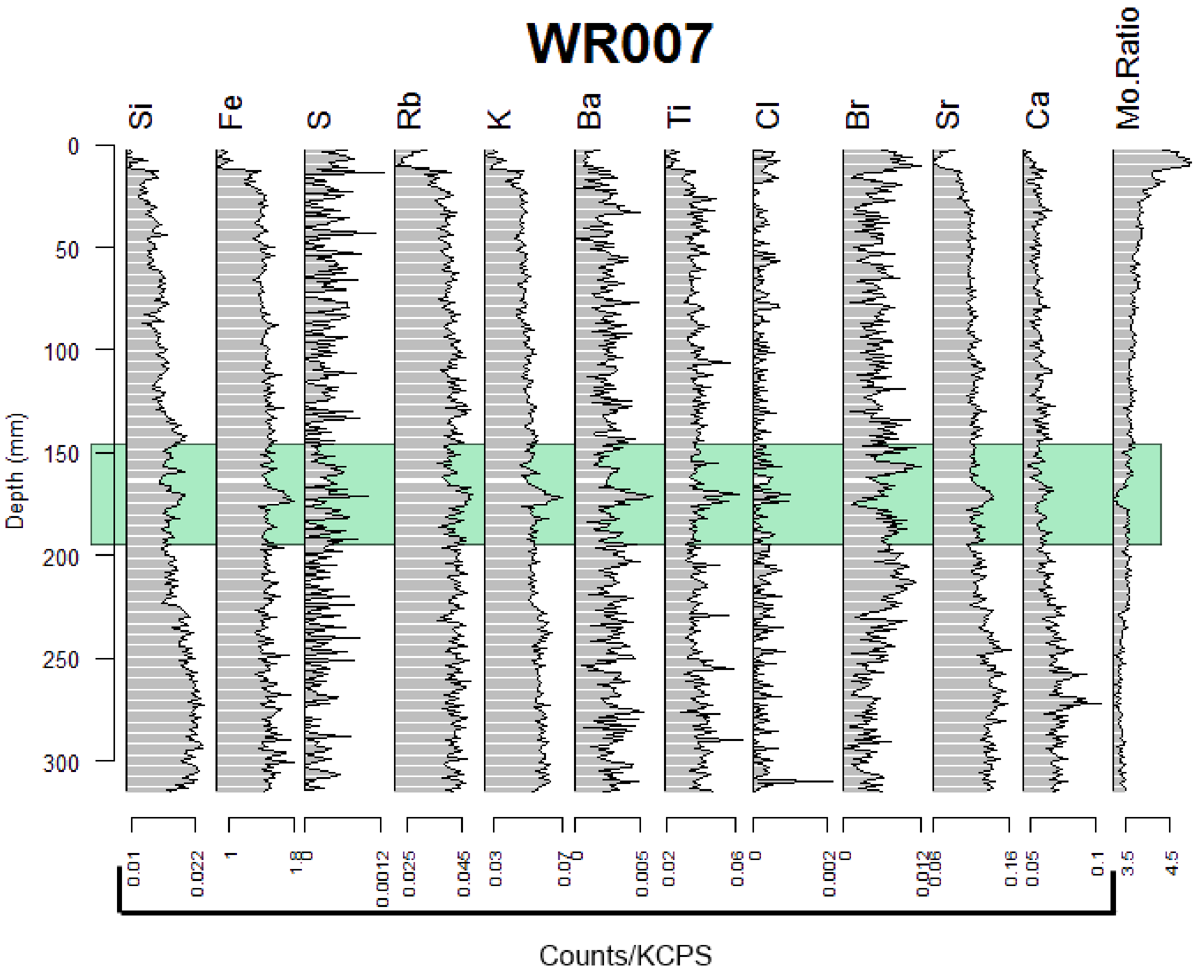

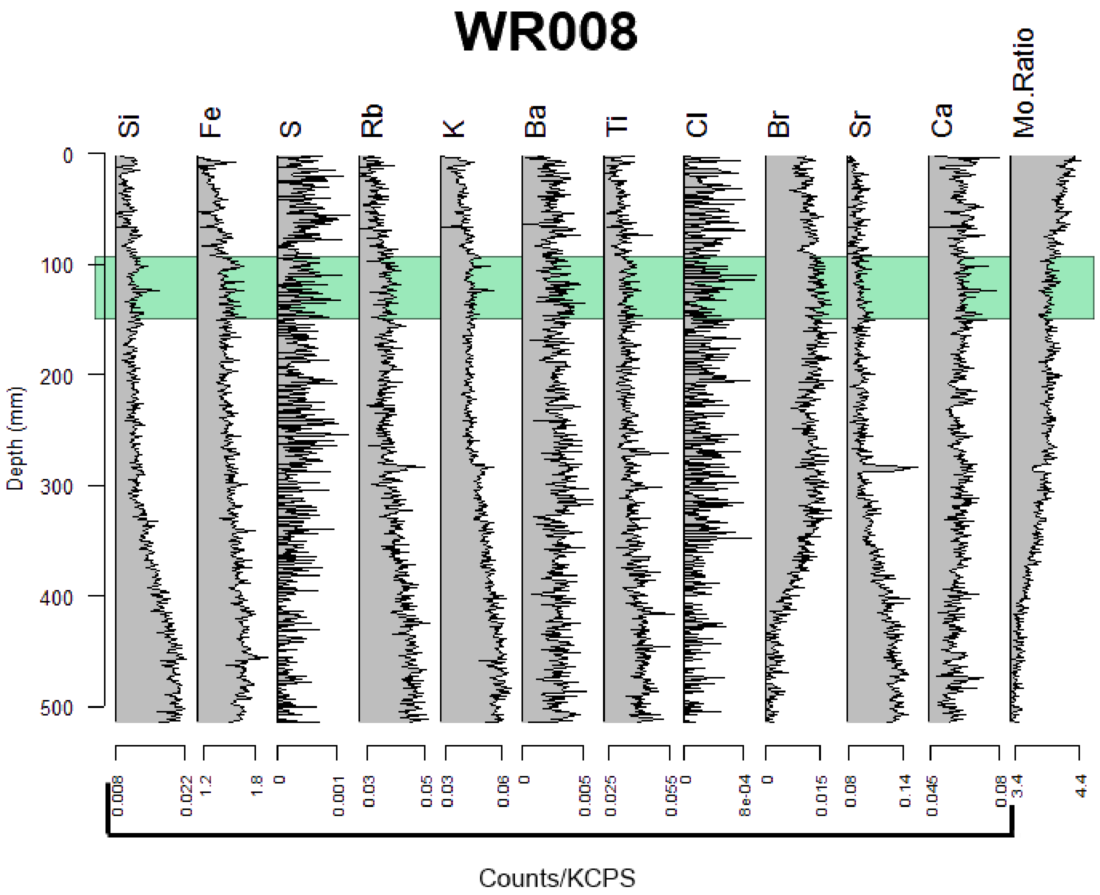
WR008
Si
Fe
S
Rb
K
Ba
Ti
Cl
Br
Sr
Ca
Mo.Ratio
Depth (mm)
0
100
200
300
400
500
0.008
0.022
1.2
1.8
0
0.001
0.03
0.05
0.03
0.06
0
0.005
0.025
0.055
0
8e-04
0
0.015
0.08
0.14
0.045
0.08
3.4
4.4
Counts/KCPS

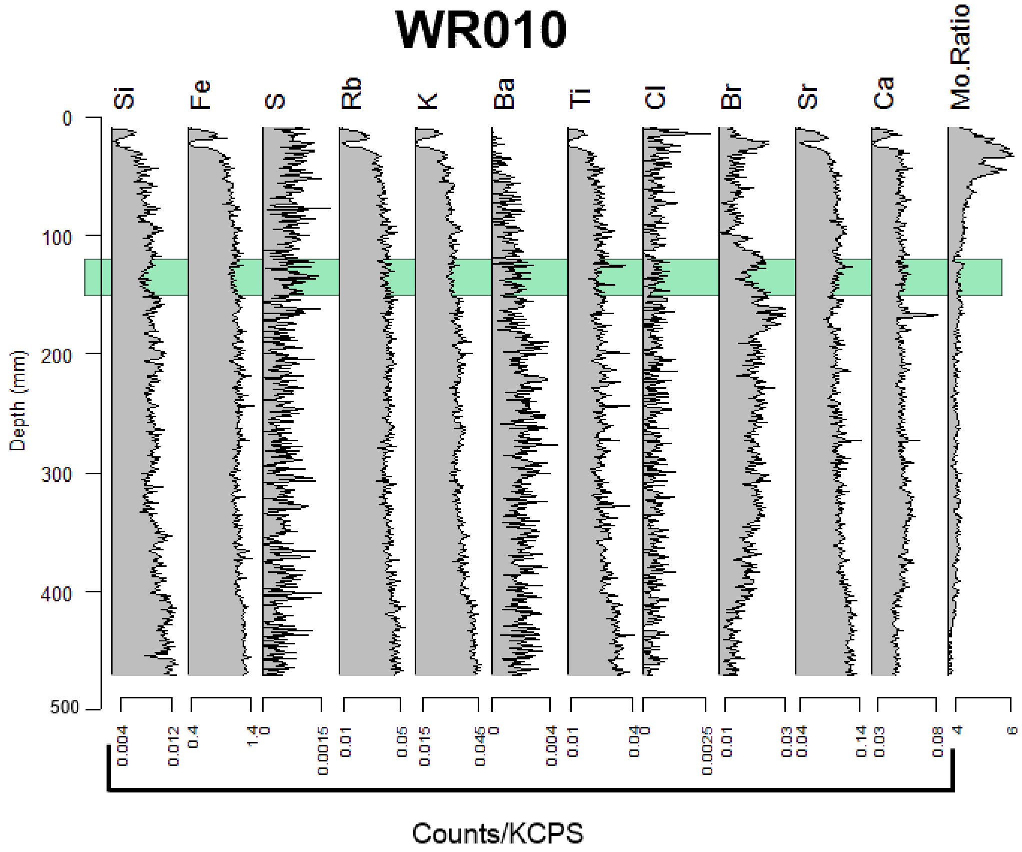
WR010
Si
Fe
S
Rb
K
Ba
Ti
Cl
Br
Sr
Ca
Mo.Ratio
Depth (mm)
0
100
200
300
400
500
0.004
0.012
0.4
1.4
0
0.0015
0.01
0.05
0.015
0.045
0
0.004
0.01
0.04
0
0.0025
0.01
0.03
0.04
0.14
0.03
0.08
4
6
Counts/KCPS

Appendix D-Diatom Data:

Appendix D.1.1-WR005 Diatom Taxa:

	Depth (cm)							
Diatom Taxa	**7-8**	**13-14**	**22-23**	**25-26**	**29-30**	**32-33**	**39-40**	**45-46**
Achnanthes affinis Grun. OIE			26	12				
Achnanthes hauckiana Grun. ME			1	5				
Achnanthes hauckiana Grun. var. rostrata Schulz. ME				15	18			
Achnanthes lanceolata (Bréb.) Grun. OIE					17			
Amphora ovalis Kütz. OIB		111	23	34	7	62	75	79
Amphora salina W. Smith OHB-MB			16	9	21			
Amphora veneta Kütz. OHB			19	2	11			
Cocconeis pediculus Ehr. OHE			54	22	35	15	5	35
Cocconeis placentula Ehr. OIE				22	14			
Diploneis interrupta (Kütz.) Cleve. MB					21	17		
Diploneis ovalis (Hilse) Cleve. OHB-OIB			1	1	2			
Eunotia diodon Ehr. HE				2	8	2		
Eunotia formica Ehr. OIE		5	11	18	17			
Eunotia spp. OIE-HE						30		
Fragilaria construens var. venter (Ehr.) Grun. OIP		11			16	2		
Fragilaria pinnata Ehr. OIE						21		
Frustulia rhomboides (Ehr.) De Toni HP					8			
Navicula pusilla W. Smith OIB			2		10	32		10
Navicula pygmaea Kütz. MB-PB				5				
Nitzschia sigma (Kütz.) W. Smith MB			1	11	12			12
Paralia sulcata (Ehr.) Cleve. PP		129		21	34	12		
Percent Broken (fresh) - OH, OI, H	0	75	22	75	90	35	5	10
Percent Broken (marine) - M, P	0	5	100	75	50	50	0	0
Pinnularia borealis Ehr. OIB			87	45	19	58	177	111
Pinnularia microstauron (Ehr.) Cleve. OIB			1	17	7			
Synedra acus Kütz. OIP-OIE			12	8	1			
Synedra pulchella Ralfs ME								4
Synedra ulna (Nitzsch) Ehr. OIE				2	4			
Total number	**0**	**256**	**254**	**251**	**282**	**251**	**257**	**251**

Key for diatom salinity preference and lifeform:

First letter: salinity preference	
P	**Polyhalobous**
M	**Mesohalobous**
OH	**Oligohalobion halophilous**
OI	**Oligohalobion indifferent**
H	**Halophobous**
Second letter: the lifeform	
P	**Planktonic - tychoplanktonic**
E	**Epiphytic, including species classified as epontic**
B	**Benthic.**

D.1.2-WR005: Salinity Preference:

	Depth (cm)							
Salinity Preference:	**7-8**	**13-14**	**22-23**	**25-26**	**29-30**	**32-33**	**39-40**	**45-46**
(P) Polyhalobous	0	50.4	0	8.4	12.1	4.8	0	0
(M) Mesohalobous	0	0	0.8	14.3	18.1	6.8	0	6.4
(OH) Oligohalobion halophilous	0	0	35.4	13.5	24.5	6	1.9	13.9
(OI) Oligohalobion indifferent	0	49.6	63.8	62.9	39.7	81.7	98.1	79.7
(H) Halophobous	0	0	0	0.8	5.7	0.8	0	0

D.1.3-WR005 Lifeform:

(P) Planktonic - tychoplanktonic	0	140	12	29	59	14	0	0
(E) Epiphytic, including species classified as epontic	0	5	92	98	113	68	5	39
(B) Benthic.	0	111	150	124	118	169	252	212

D.1.4-WR005: Condition

Percent Broken (fresh) - OH, OI, H	0	75	22	75	90	35	5	10
Percent Broken (marine) - M, P	0	5	100	75	50	50	0	0

Appendix D.2.1-WR011 Diatom Taxa:

	Depth (cm)					
Diatom Taxa	**7-8**	**14-15**	**19-20**	**25-26**	**35-36**	**45-46**
Achnanthes affinis Grun. OIE			12		1	1
Achnanthes hauckiana Grun. ME			9			
Achnanthes microcephala (Kütz.) Grun. HE-OIB	0					
Amphora ovalis Kütz. OIB	6	17	4	47	11	32
Cocconeis pediculus Ehr. OHE	17	15	14	54	15	29
Cocconeis placentula Ehr. OIE				34		11
Cyclotella meneghiniana Kütz. OHP\OHB-MP\MB		37	53		22	
Cyclotella stelligera Cleve. & Grun. OIP		23	27		33	
Diploneis interrupta (Kütz.) Cleve. MB		9		21		1
Diploneis ovalis (Hilse) Cleve. OHB-OIB			2			
Eunotia diodon Ehr. HE	4	2	3	1		
Eunotia spp. OIE-HE	22				30	48
Fragilaria construens var. venter (Ehr.) Grun. OIP	2	11	17	6	12	20
Fragilaria pinnata Ehr. OIE	12			11		3
Frustulia rhomboides (Ehr.) De Toni HP				8		18
Melosira juergensi Agardh ME		43	65	11	29	
Navicula pusilla W. Smith OIB		1		23		8
Navicula pygmaea Kütz. MB-PB			15		37	
Nitzschia sigma (Kütz.) W. Smith MB		66				
Paralia sulcata (Ehr.) Cleve. PP			23	1	44	
Pinnularia borealis Ehr. OIB	18	1		34		57
Synedra acus Kütz. OIP-OIE		18	8		9	
Synedra ulna (Nitzsch) Ehr. OIE		8	2		8	23
Total	81	251	254	251	251	251

D.2.1-WR011 Salinity Preference:

	Depth (cm)					
Salinity Preference	**7-8**	**14-15**	**19-20**	**25-26**	**35-36**	**45-46**
(P) Polyhalobous	0.0	0.0	9.1	0.4	17.5	0.0
(M) Mesohalobous	0.0	26.3	35.0	12.7	26.3	0.4
(OH) Oligohalobion halophilous	45.7	2.0	27.2	21.5	14.7	2.0
(OI) Oligohalobion indifferent	54.3	70.9	27.6	61.8	41.4	90.4
(H) Halophobous	0.0	0.8	1.2	3.6	0.0	7.2

D.2.3-WR011 Lifeform:

(P) Planktonic - tychoplanktonic	2	89	128	15	120	38
(E) Epiphytic, including species classified as epontic	58	123	105	111	83	115
(B) Benthic.	21	39	21	133	48	98

D.2.4-WR011 Condition:

Percent Broken (fresh) - OH, OI, H	0	5	25	20	35	5
Percent Broken (marine) - M, P	0	0	25	5	50	0

Appendix E- ^{137}Cs activity*:

Depth (cm)	137-Cs activity (Bq/kg)
1-2	2.1 ± 0.2
2-3	<0.4
3-4	1.6 ± 0.3
5-6	2.2 ± 0.2
9-10	1.7 ± .02
12-13	2.7 ± 0.3
16-17	2.0 ± 0.3
31-32	0.2 ± 0.1
34-35	0.4 0 ± 0.1
37-38	1.6 ± 0.3
41-42	<0.3
44-45	<0.1

*(raw data not normalised for grainsize)

Appendix F-Gravel deposit data:

GPS coordinates marking the boundary of gravel layer. Plotted in Figure 22

Latitude	Longitude	Latitude	Longitude	Latitude	Longitude
-39.167701	177.081181	-39.167287	177.080996	-39.167944	177.081656
-39.167647	177.081193	-39.167242	177.080984	-39.167962	177.081679
-39.16762	177.081193	-39.167224	177.080961	-39.167962	177.081726
-39.167593	177.081181	-39.16717	177.080949	-39.167989	177.081726
-39.167566	177.081193	-39.16771	177.081262	-39.167998	177.08176
-39.16753	177.081193	-39.16771	177.081297	-39.168025	177.081795
-39.167512	177.081193	-39.167701	177.08132	-39.168052	177.081807
-39.167512	177.081216	-39.167719	177.081355	-39.168972	177.081854
-39.167485	177.081204	-39.167746	177.081366	-39.16807	177.081876
-39.167548	177.081227	-39.167755	177.081378	-39.168097	177.081899
-39.167431	177.081146	-39.167791	177.081424	-39.168124	177.081911
-39.167395	177.081181	-39.167845	177.081471	-39.168142	177.081957
-39.167368	177.081146	-39.167854	177.081506	-39.168151	177.082015
-39.167359	177.081192	-39.167872	177.081517	-39.16816	177.082062
-39.167386	177.081239	-39.167881	177.081563	-39.16825	177.082096
-39.167323	177.081204	-39.167899	177.081587	-39.168232	177.082143
-39.167287	177.081123	-39.167917	177.08161		
-39.167323	177.081042	-39.167917	177.081644		